

Review

Formation of carbon nanoparticles from the gas phase in shock wave pyrolysis processes

Alexander V. Eremin*

Joint Institute for High Temperatures, Russian Academy of Sciences, 125412, Izhorskaya str. 13, Moscow, Russia

ARTICLE INFO

Article history:

Received 26 September 2010

Accepted 17 September 2011

Available online 20 October 2011

Keywords:

Carbon nanoparticle

Shock wave pyrolysis

Diagnostics

Induction time

Formation rate

Yield

Optical properties

Temperature

ABSTRACT

This review deals with the most recent achievements in experimental investigations of the process of carbon nanoparticle formation, at pyrolysis of various carbon bearing species behind shock waves. The diverse diagnostic methods of these processes are described; special attention is given to new methods for measuring the current sizes and optical properties of particles and the temperature of the reacting mixture using time resolved laser-induced incandescence (LII), and IR emission-absorption spectroscopy. The main part of the review provides critical analysis of the numerous results of the kinetics of particle formation at various temperatures, pressures and concentrations of carbon. Particular emphasis is placed on the results obtained by pyrolysis of hydrogen free precursors. It is shown that recent measurements of size dependence of the optical properties of particles, actual temperature of the mixture during pyrolysis of initial substances, and the subsequent growth of nanoparticles require a serious revision of current conceptions regarding the temperature dependence of particle yield and growth rate. Based on this analysis, unified regularities in these processes, with various temperatures and types of initial substances, are suggested. The last section of the paper contains a short review of the methods for modeling the processes of carbon nanoparticle formation in shock waves. Emphasis is placed on the necessity for the elaboration of more general models describing the detailed changes in particle properties during the growth process and the unified regularities of particle growth from hydrocarbons and hydrogen-free precursors as determined in experiments.

© 2011 Elsevier Ltd. All rights reserved.

Contents

1. Introduction	2
2. Experimental methods of particle formation study using shock tubes	3
3. Diagnostic technique for the investigation of carbon particle formation behind shock waves	5
3.1. Measurements of extinction	6
3.2. Scattering measurements	7
3.3. Measurements of particle radiation	10
3.4. Current particle temperature measurements	12
3.5. Method of laser-induced incandescence	13
3.6. Time resolved time-of-flight mass spectrometry	16
3.7. Post-shock analysis of formed nanoparticles	18
4. Kinetic characteristics of the particle formation process	19
4.1. Induction time of particle inception τ_{ind}	19
4.2. Rate constant of particle formation k_f	22
4.3. Kinetics of particle size growth	23
5. Size and structure of formed carbon particles	24
6. Thermal effects and ionization of particles forming in pyrolysis processes behind shock waves	25
6.1. Endothermic effects of pyrolysis reactions	25
6.2. Heat effects of particle formation	26

* Tel.: +7 495 484 19 66.

E-mail address: eremin@ihed.ras.ru.

6.3. Formation of charged particles	28
7. Temperature dependences of the particle growth process	30
7.1. Particle yield and volume fraction	30
7.2. Condensed phase growth rate	32
8. Numerical modeling of particle formation processes in pyrolysis reactions	33
9. Conclusions	36
9.1. General remarks regarding the mechanisms of carbon particle formation in gas phase reactions	36
Acknowledgments	37
References	37

1. Introduction

The formation processes of carbon particles accompanying incomplete combustion, or pyrolysis of hydrocarbons, have been investigated for many years. Originally the main objective of such research was to reduce soot and thus increase the efficiency of combustion processes. With the expansion of applications for carbon nanoparticles in manufacturing (rubber, dyes, plastics, etc.), interest in these processes has increased. Today, with the discovery of new forms of carbon (carbyne, fullerenes, nanotubes, graphene), the formation processes of condensed carbon particles are the focus of attention in a wide range of research. In addition to traditional methods based on combustion and pyrolysis of hydrocarbons [1,2], various carbon nanoparticles are now synthesized by other methods, such as chemical vapor deposition (CVD) [3,4], plasma reactors using electric arcs, microwave radiation, electron beams, and laser ablation with IR lasers [5].

Particular interest is directed toward methods of nanoparticle synthesis using gaseous precursors. These substances decay under the influence of energy, yielding a supersaturated carbon vapor which is condensed to nanoparticles. To some extent, not only thermal pyrolysis (i.e. heating to the disintegration temperature), but also plasma and laser pyrolysis reactors, are relevant to this method.

Nevertheless, a review of a number of publications on these topics has led to the conclusion that the majority of work has been purely empirical; the authors only describe the method of synthesis and detailed characteristics of the nanoparticles obtained. At the same time, a limited quantity of work has been devoted to detailed research on the formation mechanisms of various carbon nanoparticles under these or other conditions. The problem is that the majority of the methods used for nanoparticle synthesis are characterized by very difficult and poorly controlled parameters, which considerably complicate the analysis of the occurring processes. These problems are inherent in combustion as the most accepted method of carbon nanostructure synthesis [1,2], where, in addition to principal non-one-dimensionality and non-isothermality, the complex reactions of carbon oxidation proceed along with particle formation.

Therefore, for the fundamental study of the mechanisms of nanoparticle growth from a gas phase, the process of pyrolysis of gaseous carbon bearing substances behind shock waves has special appeal. The uniformity of the parameters behind shock waves in a shock tube, the variability of temperature, pressure and mixture content within wide limits and the possibility of dependable control of these parameters, and other key parameters of experimentation in the last 50 years have enabled shock tube investigations to become one of the most widespread tools – not only for studying the kinetics of various gas reactions such as relaxation processes, chemical reactions, and the kinetics of ignition and combustion – but also for heterogeneous processes like condensation, evaporation, and surface reactions with nanoparticle participation.

At this time, highly skilled scientists worldwide are actively researching the formation of carbon nanoparticles in pyrolysis processes behind shock waves. Much has been published regarding the basic regularity of the kinetics of carbon nanoparticle formation and their final properties, depending on the precursor, temperature, pressure, and concentration. Progress in these investigations has been presented approximately every ten years in the comprehensive reviews of Haynes and Wagner [6], Glassman [7], Kern and Xie [8], Bhaskaran and Roth [9], and Hai Wang [10].

The last decade has introduced considerable advancement; the main outcome of these experimental works was the implementation of a wide variety of diagnostic methods. In addition to traditional optical methods (emission, extinction, and scattering measurements in the various spectral ranges), new methods of laser-induced incandescence (LII), time-of-flight mass-spectroscopy (TOF-MS), and the versatile analysis of particles collected at the end of experimentation (including electron, atomic-force and X-ray spectroscopy, laser desorption-ionization time-of-flight mass spectrometry (LDI-TOFMS), and the chemical analysis of particle structure), have been implemented. By these methods it is possible to define the most important characteristics of the process: induction time of condensed particle formation after the start of pyrolysis (shock wave arrival), time profiles of the particle sizes, volume fraction of the condensed phase, and the properties of the obtained particles. However, the majority of the published experimental results are incomplete and the interpretations presented may be inconsistent. Data regarding induction periods, rate of particle formation and final particle yield measured by laser extinction, depend on the particle refractive index, which in turn is a function of wavelength, size and chemical content of the particles. Therefore, the comparison of data obtained under different experimental conditions, and at different stages of the process, is not always dependable.

Another example concerns the essential heat effects—both in the processes of pyrolysis and condensation—neglected by many authors, which refer to a small concentration of reacting substances in an inert diluter. Recent investigations have shown that such an approach is also not always justified.

Modeling of carbon particle formation in pyrolysis processes conventionally uses the instruments of chemical kinetics, which satisfactorily describe the initial stages of hydrocarbon polymerization and the growth of clusters. Later stages of particle surface growth and coagulation are usually described using statistical methods. However, in most cases, the purpose of these simulations is limited by the attempt to describe those or other experimental results within the framework of the offered kinetic mechanism.

Thus, despite an abundance of information on carbon particle growth under the conditions of shock-wave pyrolysis, obtaining an overall picture of the process is still rather difficult, based on the available publications. The purpose of the present review is to offer a critical analysis of the results of the available literature and to establish some generalized regularity in the formation of various carbon nanoparticles during the processes of shock-wave pyrolysis.

Section 2 contains a description of the principle of shock tube operation and an analysis of the features of this instrument for the investigation of condensed particle formation from gaseous precursors.

Section 3 is devoted to the discussion of the experimental techniques which are coupled with the shock tube method. The author has attempted to describe the various diagnostics and to show the possibilities and limitations of each method for the investigation of carbon particle formation. Particular attention has been given to new and informative methods of laser induced incandescence (LII), and two-channel IR emission-absorption particle temperature measurements.

Section 4 presents a summary of the experimental data on the kinetic characteristics of the particle formation process. Since one of the main advantages of shock tube experimentation is reliable, time resolved measurements under well controlled conditions, the kinetic data represent the most valuable information on the particle formation process obtained from these experiments. Basically, there are phenomenological data, such as induction time and the rate constant of particle formation, but the application of modern diagnostics allows for the measurement of direct particle properties, such as time profiles of mean particle size and temperature. However, in most cases the extraction of quantitative results from experimental measurements requires certain additional speculations. In this section, particular attention is devoted to the analysis of possible uncertainties and errors caused by the adopted assumptions.

Section 5 deals with the size and structure of formed carbon particles. Shock wave experiments present wider opportunities for the variation of temperature, pressure, and concentration than combustion experiments; therefore, the properties of the yielded particles also change over a broad range. On the other hand, the time for controllable parameters behind shock waves (usually about 1–3 ms) is much shorter than typical combustion times, and the possibilities for analysis of the current properties of forming particles are quite limited. Therefore, most of the data obtained refers to particles collected after experiments, and the history of post-shock cooling and mixing of young particles is practically uncontrolled. So, in Section 5, the correlation of results presented with the regularities of young particle growth is, in most cases, very qualitative.

Section 6 considers the non-isothermal effects caused by heat consumption and release during shock wave pyrolysis processes and particle ionization in shock tube experiments. These phenomena have not been analyzed before the last ten years. The application of modern temperature and electron concentration measurements has permitted the observation of important effects caused by the endothermicity of precursor decomposition, the exothermicity of particle condensation, and particle charging due to thermo-ionization of alkali metal admixtures.

Based on these results, it has become possible to correct much of the previous data which were treated using an isothermal approximation. This new view of the temperature dependencies of the particle growth process is presented in Section 7. It is shown that corrections to the actual temperature offer an opportunity to obtain the unified temperature dependence of particle yield and the rate constant of particle growth, independent of the type of precursor molecules.

Section 8 is a short summary of the methods used by various authors for numerical modeling of particle formation processes in shock wave pyrolysis reactions. The comprehensive analysis of existing models is beyond the scope of this review; therefore, an overview of the diversity of various approaches is provided, showing that there still exists no commonly accepted mechanism describing the formation of carbon particles in pyrolysis of hydrocarbons, as well as hydrogen-free precursors.

Hopefully some new general regularities, based on the analysis of experimental data presented in this review, will be helpful for further progress in modeling.

2. Experimental methods of particle formation study using shock tubes

A shock tube is a convenient and widely used tool for the investigation of various physical and chemical processes in a wide range of temperatures and pressures. Modern shock tubes present opportunities for generating temperatures over 20 000 K (with explosive-driven shock waves), and pressures from 0.01 to 1000 bar [11,12].

The theory and construction of shock tubes are presented in detail [13,14]. A convenient shock tube consists of a high pressure driver section and a low pressure test section, which are separated by a diaphragm (see Fig. 1). Before beginning an experiment, the high pressure section is filled with the driving gas and the test section is filled with an investigated gas mixture. After diaphragm rupture (which could occur by increasing the pressure of the driving gas, or by means of a special device), the driving gas from the high pressure section rushes into the test section, owing to the formation of a shock wave in the investigated mixture and a rarefaction wave expanding in the driving gas in the opposite direction. A schematic diagram of the processes occurring in a shock tube is shown in Fig. 1. The investigated gas, compressed and heated by the shock wave (area 2 on the diagram), is separated from the driving gas by a contact surface. After reflection from the end plate of the tube, the shock wave moves through the gas, already heated by the incident wave. This results in further heating and compression of the mixture. From conditions of continuous flow, it is obvious that the mixture behind the reflected shock wave (area 5 in Fig. 1) stagnates relative to the walls of the tube that allows for observation of the fixed group of molecules during the working time of the shock tube. The end of the working time, Δt_R , is determined by the arrival of the next disturbance as a result of the interaction of the reflected shock wave with the contact surface (as shown in Fig. 1), or the arrival of the head of a rarefaction wave, reflected from the opposite end plate of the tube. Usually, this takes no more than several milliseconds. To increase this time, researchers choose the so-called 'tailored' regime of flow in which the passage of the reflected shock wave through the contact surface does not cause additional disturbances to propagate in the zone of the investigated mixture (area 5 in Fig. 1). Additionally, to avoid further heating of the investigated mixture and its mixing with the driving gas, so-called single-pulse shock tubes equipped with an additional dump tank [12,15] are used.

Compared to any gas or plasma reactor, the basic advantages of a shock tube are the almost instant, homogeneous heating of a gaseous mixture to the necessary temperature and pressure, and the absence of complicating factors such as diffusion, heat conductivity, and heterogeneous processes on the walls. On the other hand, the restriction of the working time in a shock tube (a value of about $\sim (1-3) \times 10^{-3}$ s) does not permit the study of the processes taking place over greater time scales. Therefore, the major advantage of a shock tube for the investigation of condensed nanoparticle formation is the excellent conditions for studying the initial stages of soot formation; however, slow processes such as coagulation, crystallization, etc., in shock tube experiments are difficult to observe.

The high degree of uniformity and the one-dimensionality of flow in a shock tube allow a reliable description of the mixture parameters which depend upon shock wave intensity. In the system of coordinates connected with shock waves, the parameters of a gas mixture behind a shock wave are determined by the laws of conservation of mass, impulse, and energy:

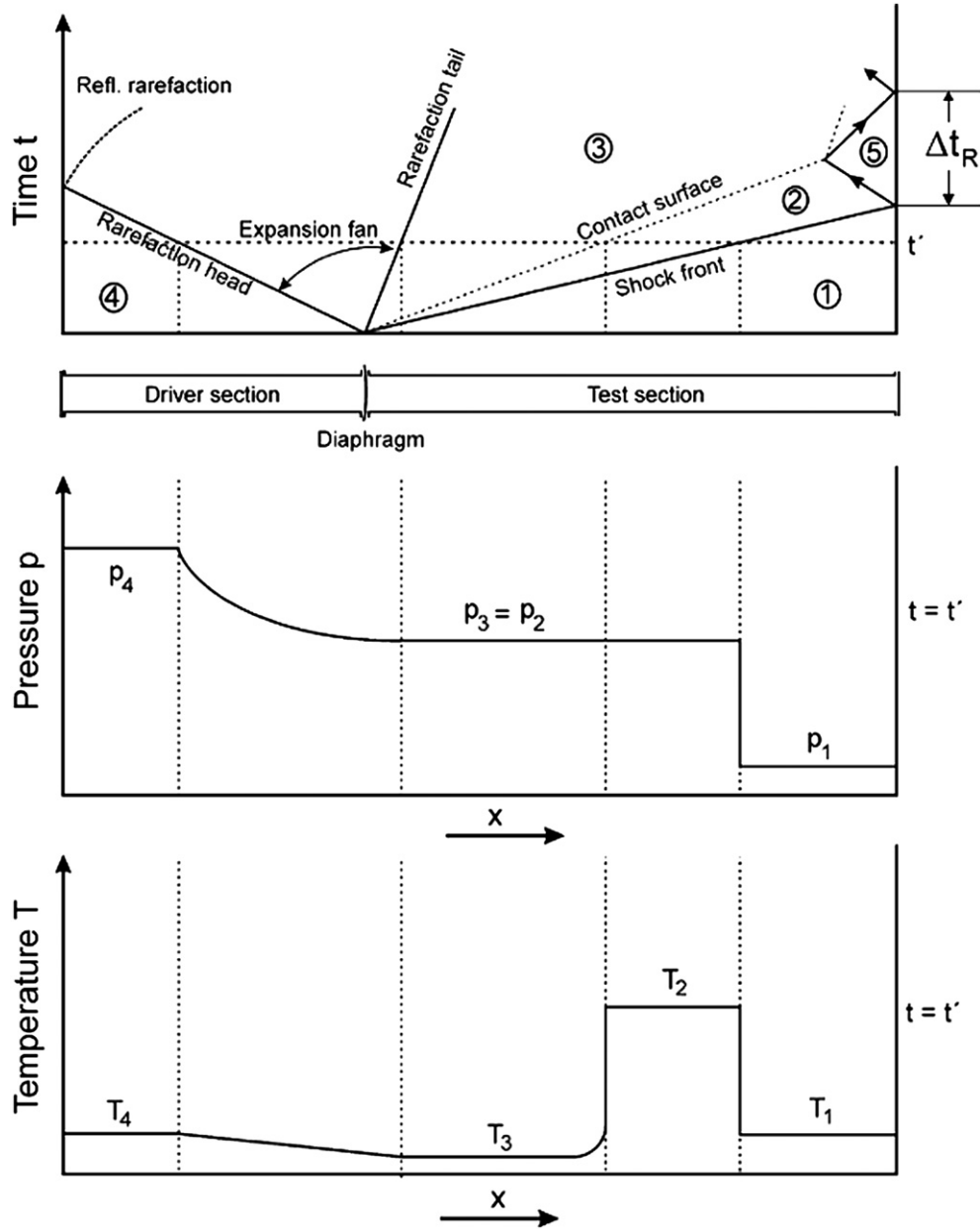


Fig. 1. x – t diagram of a simple shock tube. (1) initial test gas, (2) shocked gas, (3) driver gas behind contact surface, (4) initial driver gas, (5) test gas subjected to reflected shock. Ref. [9].

$$\begin{aligned} \rho_1 u_1 &= \rho_2 u_2 \\ P_1 + \rho_1 u_1^2 &= P_2 + \rho_2 u_2^2 \\ H_1 + \frac{1}{2} u_1^2 &= H_2 + \frac{1}{2} u_2^2 \end{aligned} \quad (1)$$

where ρ , P , H and u designate density, pressure, enthalpy of a unit mass of gas and its velocity; indices 1 and 2 correspond to the initial gas and the gas compressed by a shock wave.

In an ideal gas, which has the constant heat capacities ratio $\gamma = C_p/C_v$, enthalpy can be expressed as:

$$H = \left(\frac{\gamma}{\gamma - 1} \right) \frac{P}{\rho} \quad (2)$$

Substituting expression (2) in the equation of energy conservation (1) and combining it with the equations of mass and impulse conservation, it is easy to obtain Rankine–Hugoniot equations

defining the ratio of pressures and densities at the front of the incident shock wave in an ideal gas:

$$\begin{aligned} \frac{P_2}{P_1} &= \frac{1 - \left(\frac{\gamma - 1}{\gamma + 1} \right) \frac{\rho_1}{\rho_2}}{\frac{\rho_1}{\rho_2} - \frac{\gamma - 1}{\gamma + 1}} \\ \frac{\rho_2}{\rho_1} &= \frac{\frac{\gamma - 1}{\gamma + 1} + \frac{P_2}{P_1}}{\left(\frac{\gamma - 1}{\gamma + 1} \right) \frac{P_2}{P_1} + 1} \end{aligned} \quad (3)$$

Furthermore, using the equation of the state of an ideal gas $P = \rho RT$, and introducing the Mach number of the shock wave, which is equal to the ratio of its velocity U to the velocity of sound in the gas before the wave c ($M = U/c$), it is possible to obtain the

equation which determines the degree of heating of the gas behind the front of a shock wave:

$$\frac{T_2}{T_1} = \frac{[2\gamma M^2 - (\gamma - 1)][(\gamma - 1)M^2 + 2]}{(\gamma + 1)^2 M^2} \quad (4)$$

The equations for the reflected shock wave do not allow for the expression of the physical parameters of the mixture behind the reflected shock front directly through the values characterizing the initial conditions of the mixture in a shock tube. Therefore, the parameters behind the reflected shock wave are usually calculated through the parameters of an incident shock wave. Thus, the Mach number of the reflected shock wave is defined from a condition in which the velocity of the movement of the mixture, relative to the tube walls, should be equal to zero, after the passage of the front.

Note that the process of heating the mixture, caused by compression in a shock wave (unlike isentropic compression), is irreversible. From the equation of energy conservation (1), it is easily seen that transition through shock is characterized by an irreversible transformation of kinetic energy into thermal energy. Thus, owing to entropy growth at the wave front, gas heating in a shock wave is essentially higher than at isentropic compression. So, a pressure increase in a shock wave front by a factor of 50 will increase the temperature of an ideal gas (with $\gamma = 1.4$) from room temperature (293 K), to 3177 K, while at isentropic compression, the temperature will increase only to 897 K [14].

Another important circumstance is that – unlike an ideal gas – heating and compressing of the real gas in a shock wave are accompanied by an essential change in its heat capacity. The first process is the excitation of the internal degrees of freedom of molecules. After that proceed the chemical reactions, which change the content of the investigated mixture. Finally, the processes of ionization of atoms and molecules take place at higher temperatures.

Researching the reactions of ignition and combustion behind shock waves, or heterogeneous processes of condensed particle formation, becomes even more complicated due to the large complex of endothermic and exothermic reactions. In these situations, an exact calculation of the current parameters of the reacting mixtures demands reliable knowledge of a huge set of the thermal effects of the occurring reactions and the thermodynamic parameters of all the formed particles. In most cases, such data are absent and the corresponding calculation is impracticable. Therefore, researchers try to work with strongly diluted mixtures in which the content of reacting molecules in an inert gas does not exceed several percent.

Even under these conditions, the calculation of the current parameters of a reacting mixture represents an independent problem which is frequently the object of investigation. Therefore, as calculated parameters of a mixture, the so-called “frozen” parameters, which characterize the mixture directly behind the front (after the establishment of equilibrium on internal degrees of freedom, but with frozen chemical transformations), are used. In this case, the enthalpy of a gas mixture at temperature T is defined by the sum:

$$H = \frac{3}{2}RT + E_R + E_V + RT \quad (5)$$

where E_R and E_V are the rotational and vibrational energies of the molecules of the mixture and R is the universal gas constant.

In the majority of work relative to such frozen parameters, which are determined by the velocity (or Mach number) of an incident shock wave, all subsequent processes are analyzed.

Finally, it must be emphasized again that Equations (1)–(5) do not consider the possibility of non-one-dimensional flow in a shock tube, the viscosity of the gas or heat transfer to the walls.

Nevertheless, using experimental measurements of velocity of an initial shock wave to calculate the parameters of a mixture (before chemical transformations), both behind the incident and reflected shock wave, provides good accuracy in most cases.

3. Diagnostic technique for the investigation of carbon particle formation behind shock waves

The use of a shock tube provides unique possibilities for investigating the kinetics of carbon nanoparticle formation from various precursors and at various temperatures, pressures and concentrations. However, the processes investigated in shock tubes have significant time restrictions (usually 1–3 ms). Therefore it is often not possible to observe late processes of particle growth, such as coagulation, crystallization and the formation of specific nanostructures, such as nanotubes, in these experiments. In this regard, the data obtained from shock tube experiments mainly concern the initial stages of particle growth: from the gas phase reactions of pyrolysis to the formation of primary condensed particles.

Historically, the basic methods for investigating gas phase processes in shock waves were emission and absorption spectroscopy. Therefore, these types of diagnostics have been applied to the study of the processes of condensed particle formation. In gas mixtures, methods of absorption spectroscopy at known cross-sections of absorption provide the opportunity to measure the concentration of absorbing molecules. In mixtures containing condensed particles, the situation is more complex. First, in addition to absorption, the condensed particles also scatter radiation; therefore, total attenuation of passing radiation is defined by a complex refractive index of particles

$$m = n + ik \quad (6)$$

where a real n and imaginary k parts reflect the contributions of scattering and absorption to the total attenuation (extinction) of the passing radiation.

Typical values of a complex refractive index for normal soot particles, of 20–30 nm, observed in flames in a wide range of the spectrum (from UV to IR), are varied from $m = 1.90 - 0.55i$ [16] to $m = 1.56 - 0.46i$ [17]. The commonly used value for analyses of soot, summarized from the data of many sources, is $m = 1.57 - 0.56i$ [18]. In contrast to normal soot, very small soot-like particles, transparent in the visible range, were observed in [19], in rich, premixed, ethylene/air flames. The refractive index for these transparent particles of 2–3 nm was determined by behavior of their absorption and fluorescence at 266 nm and found to be $m = 1.4 - 0.08i$ [19]. However, carbon particles formed from the hydrogen-free precursor C_3O_2 , are apparently much more black than normal soot; for these particles, values of $m = 1.57 - 1.4i$ were suggested [20]. A discussion of the role of the actual values of a complex refractive index in the analysis of observable properties of carbon particles appears in Sections 4.1, 7.1, 7.2.

In the Rayleigh approach (the size of particles is much less than the wavelength), the absorbing part of the refractive index is essentially more than the scattering part, and the extinction coefficient of the particles ε can be expressed as [21]:

$$\varepsilon = -\frac{6\pi}{\lambda} \operatorname{Im} \left\{ \frac{m^2 - 1}{m^2 + 2} \right\} \quad (7)$$

The second specificity of such measurements is that, usually in the mixture, even at a fixed moment in time, particles of the various sizes are contained. It is even more difficult to analyze the development of particle growth over time, when it is necessary to deal not only with particles of various sizes (having, correspondingly, various refractive indices), but also with variable particle number

density $N(t)$ (cm^{-3}), which decreases in the process of coagulation. In this regard, the measured level of extinction is usually linked to the total volume of the condensed particles in the mixture, expressed in the form of the volume fraction of the condensed phase f_V [6].

In the case of spherical particles with diameter D and known size distribution of number density

$$p(D) = dN/dD \quad (8)$$

the total volume fraction can be expressed as:

$$f_V = \frac{\pi}{6} \int p(D) \cdot D^3 dD \quad (\text{cm}^3 \text{cond}/\text{cm}^3) \quad (9)$$

3.1. Measurements of extinction

When all sets of particles in the mixture can be presented as spherical particles of uniform size D and number density N , their volume fraction f_V is equal to

$$f_V = \frac{\pi}{6} N \cdot D^3 \quad (10)$$

Particle extinction, determined by the attenuation of passing radiation, is linked to the volume fraction of the condensed phase by the Beer–Lambert law:

$$I/I_0 = \exp(-l \cdot f_V \cdot \varepsilon(m, \lambda, D)) \quad (11)$$

where I_0 and I are the intensity of radiation of a probing source before and after the shock tube and l is the length of extinction (diameter of the shock tube).

Another important characteristic of the process of carbon particle formation, which is determined from extinction measurements, is the so-called yield of the condensed carbon (or a soot yield) Y , representing the relationship between the total number of atoms in the particles to the total number of available carbon atoms in the precursor. At known particle density ρ , the relationship between f_V and Y is given by simple parity:

$$Y = f_V \frac{\rho}{M_C [C]} \quad (12)$$

where M_C is the molecular weight of carbon and $[C]$ is the full initial concentration of the carbon atoms participating in process of particle formation. Thus, the particle yield can be calculated from the extinction data with use of the following equation:

$$Y = \frac{\ln(I_0/I) \rho}{\varepsilon l M_C [C]} \quad (13)$$

Measurement of extinction time profiles is one of the most informative methods of investigation into the processes of carbon particle formation behind shock waves. Such measurements have been carried out in a considerable number of works (see for example [22–38] and references therein). In most cases for this purpose, the convenient He–Ne laser with $\lambda = 633$ nm is used, though in some works, measurements on other wavelengths from the UV to IR range [23,26,27,29,33,34] were performed.

One of the important advantages of extinction measurements is their very high sensitivity. It is easy to show that at a soot extinction coefficient ε for probing wavelength 633 nm equal to $\sim 5 \times 10^6 \text{ m}^{-1}$ [18] and a signal/noise ratio greater than 100 (which is easily achievable for modern lasers and photodetectors) in a shock tube with an inner diameter of 10 cm, it is possible to register the soot volume fraction f_V about $\sim 2 \times 10^{-8}$ that corresponds to a particle size of 20 nm and a number density of $\sim 5 \times 10^9 \text{ cm}^{-3}$.

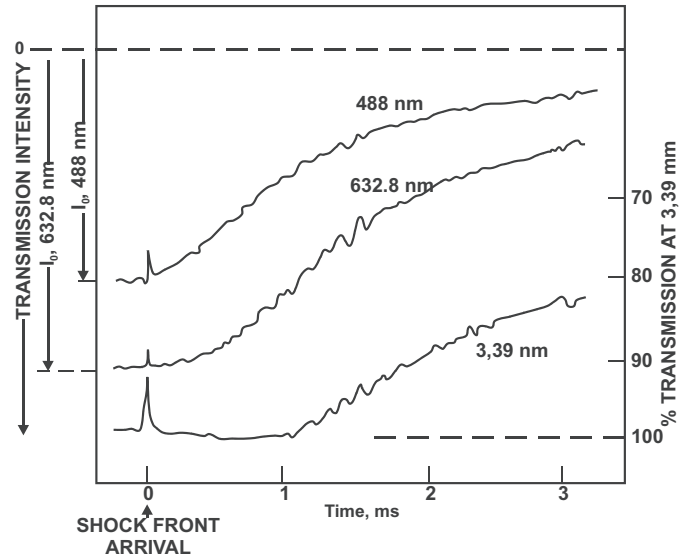


Fig. 2. Examples of extinction profiles measured at various wavelengths in ethyl benzene. $T = 1750$ K, $[C] = 2 \times 10^{17} \text{ cm}^{-3}$. Ref. [39].

On the other hand, at a too-high particle content, the attenuation of the transmitted signal becomes so strong such that the accuracy of the measurements sharply decreases. At the above-mentioned parameters, it is not possible to measure a soot volume fraction higher than 10^{-5} .

In following Figs. 2–4, examples of characteristic records of extinction signals behind shock waves, particle volume fraction f_V (see Eq. (10)) extracted from them, and normalized optical density $D_n = Y \varepsilon / \rho$ (see below) in various precursors and at various wavelengths are presented. In the plots shown in Figs. 2 and 4, the tendency of an increase in the induction period and a decrease in the rate of extinction rise toward longer wavelengths is clearly

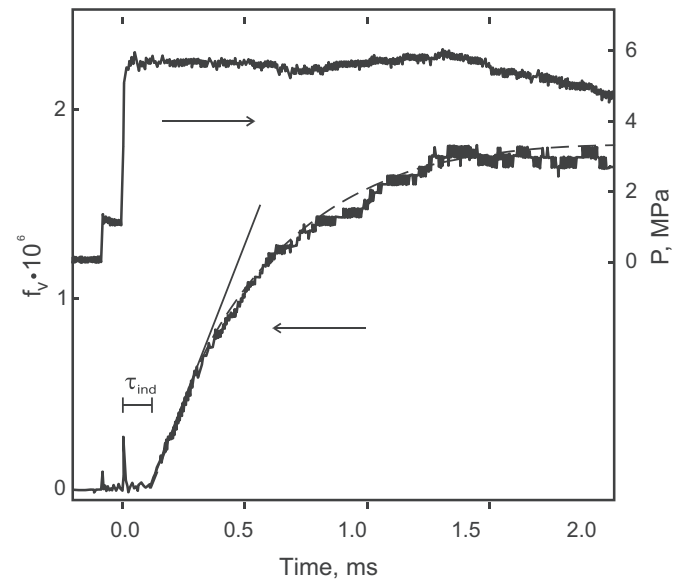


Fig. 3. Typical profile of volume fraction of the condensed particles f_V , determined from the extinction record at 633 nm and a pressure profile behind the reflected shock wave in a mixture 0.03% $\text{C}_6\text{H}_6 + \text{Ar}$. $T = 1890$ K, $[C] = 5 \times 10^{17} \text{ cm}^{-3}$. Tangent crossing the f_V curve on the time axis defines the induction time τ_{ind} . The dashed line indicates an approximation of the experimental profile by the relaxation equation (see Equation (30) in Section 4.2). Ref. [31].

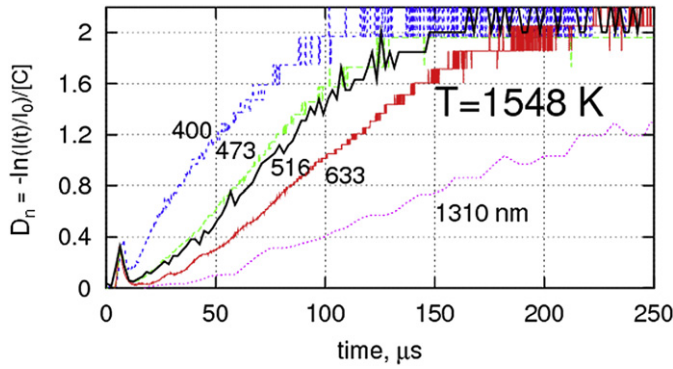


Fig. 4. Time profiles of normalized optical density D_n , measured simultaneously at different wavelengths from the UV to the IR range of the spectrum. Mixture 1% C_3O_2 in Ar. $P = 28$ bar. Ref. [34].

seen. The correlation of this phenomenon with the change of the optical properties of growing particles will be discussed below.

The analysis of the kinetic part of the obtained records will be given in Section 4, so now we will consider only the final, established stationary values of extinction, from which the final particle yield Y can be determined. The yield (or volume fraction) of the condensed particles has been measured in practically all studies on particle formation behind shock waves. The accumulated experimental results represent a large volume of data on particle yield during the pyrolysis of various precursors at a wide variation of pressure and temperatures behind a shock wave. The most extensive data have been obtained on the temperature dependence of soot yield Y . Starting from the first measurements, it was noticed that this dependence has a bell shape (see for instance [6,25–28,31,33,35]). Typical examples of bell-shaped soot yield are shown in Fig. 5. It is necessary to note, however, that the position on a temperature scale and the form (width) of this dependence for different precursors, measured by various authors, essentially differ from each other. The most substantial is a shift in the temperature dependence of soot yield during the pyrolysis of carbon-chlorides [40–42]. The reasons for these distinctions and an analysis of the physical reasons for this type of temperature dependence of soot yield Y are described below.

It is important to underline once again, however, that the extraction of absolute values of particle yield requires serious assumptions that all sets of particles can be attributed uniform (and known) values of the extinction coefficient e and density ρ . Note that the authors of the majority of works on the investigation of soot formation proceeded in this way; the errors connected with this method and the ambiguity in interpretation will be discussed in Section 7.1. A more accurate (careful) approach was mentioned for the first time in [39] and later used in other studies [34,40–42] for the analysis of hydrogen-free carbon particles (for which values of e and ρ are poorly known). This consideration limits particle yield in relative quantities: “relative soot yield” $Y_r = Y \times \varepsilon$ [26,40,43], or so-called normalized optical density $D_n = Y \varepsilon / \rho$ [34,36,42,44], represented in arbitrary units (see Figs. 4 and 6).

With such an approach, independent measurements of the extinction coefficient e (see [45]) have provided the opportunity to interpret the temperature dependence of particle yield in quite a different way. It will be shown below that such a correction of the experimental dependence of soot yield in turn serves as a push to revise the commonly accepted notions on the mechanisms of formation of soot at high temperatures.

3.2. Scattering measurements

The effect of light scattering by the particles represents additional possibilities for diagnostics. The intensity of scattered radiation in a Rayleigh approach can be written in the following shape [46]:

$$S_{VV} = \eta \cdot Q_{VV} \cdot I_{0,V} \cdot \Delta\Omega \cdot \Delta V \quad (14)$$

where η and $\Delta\Omega$ are efficiency and the solid angle aperture of the registering system, $I_{0,V}$ is the flux of incident radiation, ΔV is the scattering volume and Q_{VV} is the scattering coefficient, depending on particle size to the sixth power D^6 :

$$Q_{VV} = \frac{\pi^4}{4\lambda^4} \left| \frac{m^2 - 1}{m^2 + 2} \right|^2 N \cdot \int_0^\infty p(D) D^6 dD \quad (15)$$

So, the strong dependence of the scattering signal on particle size on the one hand makes it possible to achieve high-sensitivity

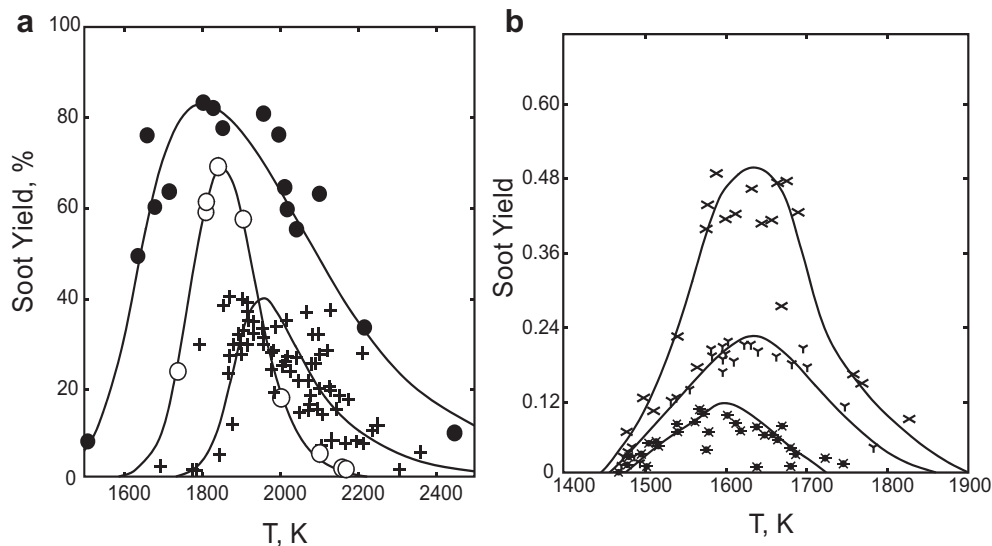


Fig. 5. Typical examples of temperature dependencies of soot yield in various hydrocarbon precursors. (a): ● benzene, ○ ethylene, + n-hexane. $P = 50$ bar. Ref. [32]; (b): × C_6H_8 , ▼ C_7H_8 , * C_2H_2 . $P = 2.5$ –10 bar. Ref. [28].

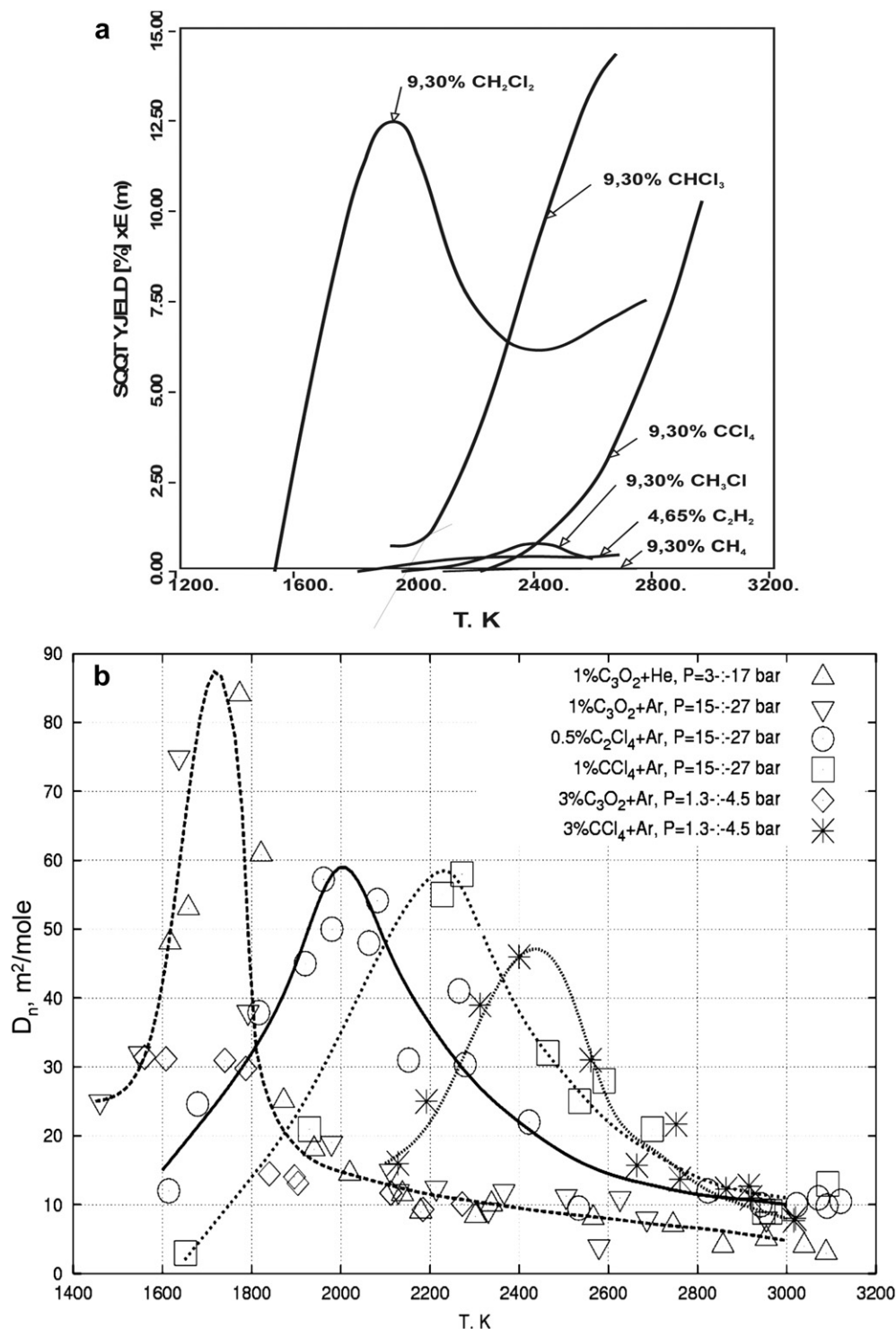


Fig. 6. Examples of the essential shift of bell-shaped temperature dependencies of relative soot yield Y_r or normalized optical density D_n in various hydrogen-free precursors (a) $P = 0.4\text{--}3.6$ bar, Ref. [40]; (b) Ref. [42].

measurements of any change in particle size; however, on the other hand, it sharply limits the minimum size of particles accessible to measurements. The first series of works on the measurement of the sizes of the carbon particles formed in the processes of pyrolysis behind shock waves was performed by Graham and Homer [39,47]. Later, similar measurements were performed in other studies [37,48–52]. The typical scheme of simultaneous measurements of

scattering and extinction during carbon particle formation in a shock tube is shown in Fig. 7.

In Fig. 8, the example of time profiles of intensity of the scattered radiation, measured during the pyrolysis of n-heptane and the growth of the particles extracted from it are shown [48]. It can be seen that the method of scattering can be used to observe particles with sizes above 5–10 nm.

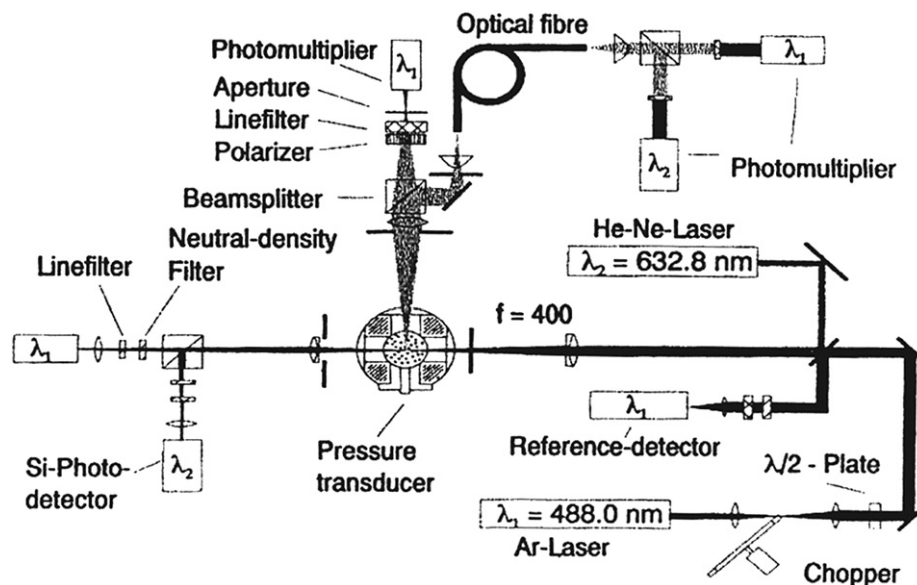


Fig. 7. Scheme of simultaneous scattering and emission measurements in shock tube pyrolysis experiments. Ref. [51].

In Fig. 9, the temperature dependence of the final particle size is shown, measured by the scattering method. One can see that these dependences, like the temperature dependence of particle yield (Figs. 5 and 6), have a bell shape.

Thus, it is necessary to make one important remark. Determination of the absolute particle size by the scattering method leans upon knowledge of the extinction coefficient (7), which in all works

mentioned above was considered independent of the particle size and was accepted to be equal to the value determined for soot in the investigation of flames [16–18,46,53]. Other independent methods of instantaneous measurement of nanoparticle sizes, based on the registration of laser-induced incandescence (LII) of particles, will be described below. Unlike the scattering method, the absolute measurement of particle sizes performed by the LII method does not depend so crucially on the extinction coefficient. Moreover, such measurements in some cases allow for extracting the absolute values of the extinction coefficient depending on the particle size. So, in a recent work [45], it has been shown that only in the range of carbon particle sizes from 10 to 25 nm, a sharp change in their optical properties takes place. In this work, using a two-channel method of laser-induced incandescence, the authors could obtain a dependence of the function of particle refractive index $E(m)$:

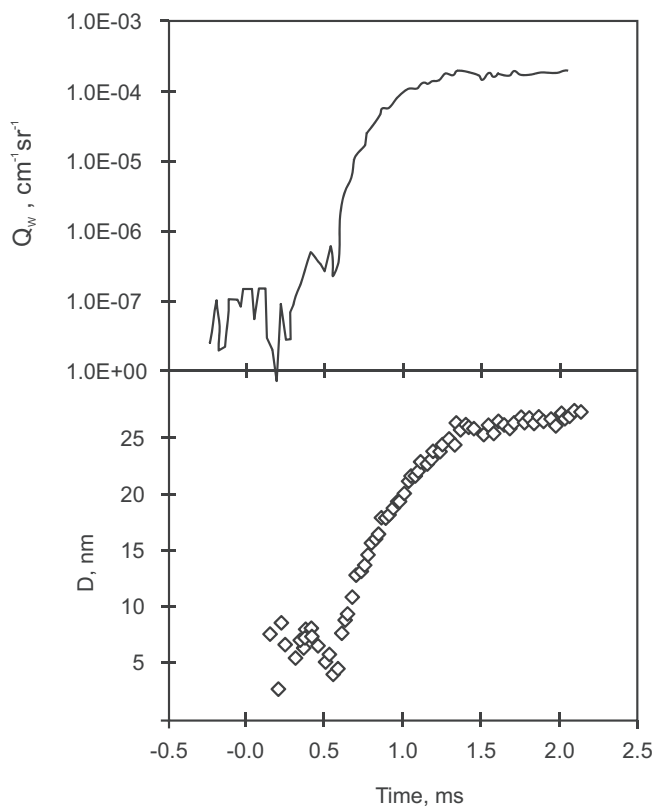


Fig. 8. The time profiles of intensity of the scattered radiation, measured during the pyrolysis of n-heptane and the growth of the particle size extracted from it. $T = 1750$ K, $P = 25$ bar, $[C] = 7.89$ mol/m³. Ref. [48].

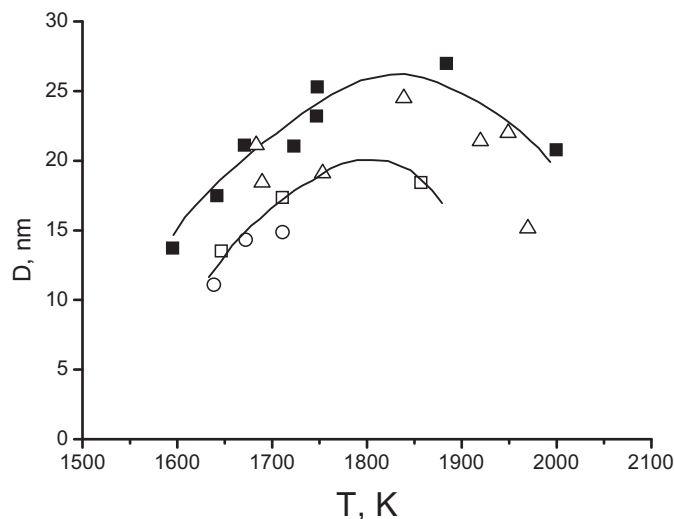


Fig. 9. The temperature dependencies of particle size determined by scattering-extinction measurements during shock wave pyrolysis of n-heptane at different concentrations and pressures. ■ - $P = 25$ bar, Ar = 96%; △ - $P = 60$ bar, Ar = 99.5%; + - $P = 80$ bar, Ar = 99.5%; * - $P = 100$ bar, Ar = 99.5%. Ref. [48].

$$E(m) = \frac{\varepsilon\lambda}{6\pi} = -\text{Im}\left\{\frac{m^2 - 1}{m^2 + 2}\right\} \quad (16)$$

on the size of growing carbon particles. In Fig. 10, the results of experimental measurements [45] of the size dependence of the values of $E(m)$ at a wavelength $\lambda = 1064$ nm during acetylene pyrolysis behind a shock wave are given. One can see that for small particles less than 10 nm in diameter, the value of $E(m)$ is below 0.1, which qualitatively agrees with observations of “transparent” nano-organic carbon particles with a complex refractive index of $m = 1.4 - 0.08i$ in the UV range ($\lambda = 266$ nm) [19]. With increasing particle size, $E(m)$ approaches usual soot values ~ 0.4 , corresponding to the commonly used value $m = 1.57 - 0.56i$ for the visible range [18] and a wavelength dependence of $E(m) = 0.232 + \lambda(1.2546 \times 10^3 \text{ cm}^{-1})$, as suggested in [54].

An account of this dependence $E(m) = f(D)$ should lead to essential amendments to the measurements performed by the scattering method.

3.3. Measurements of particle radiation

The emission characteristics of the carbon particles formed behind shock waves have been much less investigated. The problem is that such measurements strongly depend on the real temperature of the particles, which for various reasons can differ from the calculated “frozen” temperature of the mixture, usually determined from the velocity of the shock wave (see Section 2). Nevertheless, by means of emission measurements, a variety of interesting observations, reflecting both the spectroscopic properties of the particles and the thermal effects of the proceeding reactions, has been obtained [29,34,36,55–58]. In Fig. 11, an example of time profiles of particle radiation measured simultaneously at various wavelengths from visible to IR is demonstrated [58]. One can see that particles have a smooth spectral distribution of emissivity which gradually approaches equilibrium with the maximum at about $1.5 \mu\text{m}$.

In Fig. 12, the data on the change in particle emission spectra measured during toluene pyrolysis in [29] are cited. One can see that in the range of 200–400 nm at early times in pyrolysis, intense UV bands are observed, which were attributed by the authors to polyaromatic structures, while in the range of 400–700 nm at later

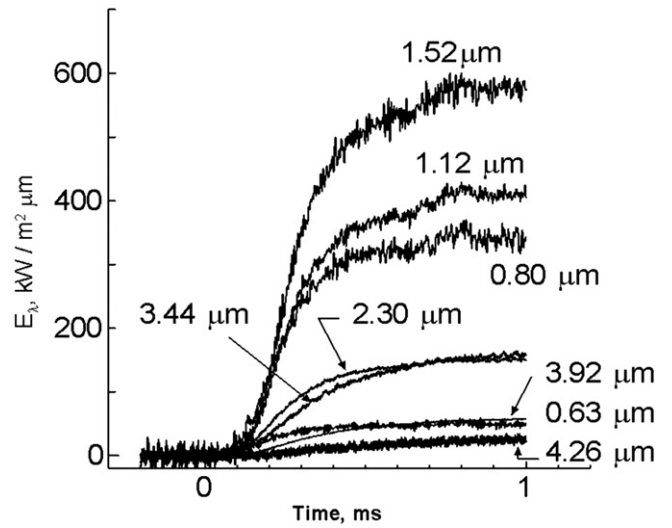


Fig. 11. Time profiles of thermal radiation of growing soot particles. Mixture 0.5% $\text{C}_6\text{H}_6 + \text{Ar}$. $T_5 = 1930$ K. Ref. [58].

times (500–1000 μs) the spectrum of particle radiation coincides well with the radiation of a black body. The radiation spectra measured by an intensified CCD-camera during the pyrolysis of a hydrogen-free precursor C_3O_2 [36] look somewhat different. In this process, hydrocarbon radicals, active in the UV spectrum, could not be formed, therefore it was possible to observe a pure spectrum of growing carbon particles. At an early time point $t = 50 \mu\text{s}$ in these smooth spectra (shown in Fig. 13), only intensive peaks of Swan-bands of the C_2 radical (at 473 nm) which, apparently, disappear with increasing reaction time, could be noted. At later reaction times (more than 400 μs), a decrease in the integral intensity of the radiation, explained in [36] by processes of particle coagulation, was observed.

One more important circumstance can be noted on the presented spectra. At early time points of the process (up to 400 μs), spectrum expansion toward the long wavelengths is appreciable. This effect can be most plausibly explained by the change in the optical properties of particles in the process of their growth, discussed in the previous Section 3.2.

More attentive analysis of the changes in particle optical properties during their growth has been performed in [56], where the data on the emission of growing particles at $1.3 \mu\text{m}$ have been analyzed jointly with extinction measurements at two wavelengths, $1.3 \mu\text{m}$ and 633 nm . Assuming that at each moment of time a unified value of refractive index m (6) can be attributed to all particles, and considering that the process of laser beam attenuation by the cloud of particles is determined by the sum of absorption and scattering processes, authors showed that the extinction ratio (see Eq. (11)) ER_λ at wavelengths λ_1 and λ_2 :

$$ER_\lambda \equiv \frac{\ln(I_1/I_{0,1})}{\ln(I_2/I_{0,2})} \approx \frac{\varepsilon_{\text{ext}}(\lambda_1)}{\varepsilon_{\text{ext}}(\lambda_2)} = \frac{\varepsilon_{\text{sca}}(\lambda_1) + \varepsilon_{\text{abs}}(\lambda_1)}{\varepsilon_{\text{sca}}(\lambda_2) + \varepsilon_{\text{abs}}(\lambda_2)} \quad (17)$$

could present information either about the particle size (assuming that the refractive index is known and constant), or about the change in refractive index, in particular, of its imaginary part k (6), responsible for absorption, which is very sensitive to the structure of particles and their temperature [16,21]. In ratio (17), $\varepsilon_{\text{abs}}(m, \lambda, d)$ and $\varepsilon_{\text{sca}}(m, \lambda, d)$ are the absorption and scattering coefficients, which depend on particle size D , $m = n + ik$ is the complex refractive index and wavelength is λ . Besides that, the ratio of extinction and emission at the same wavelength, expressed by the function F_λ :

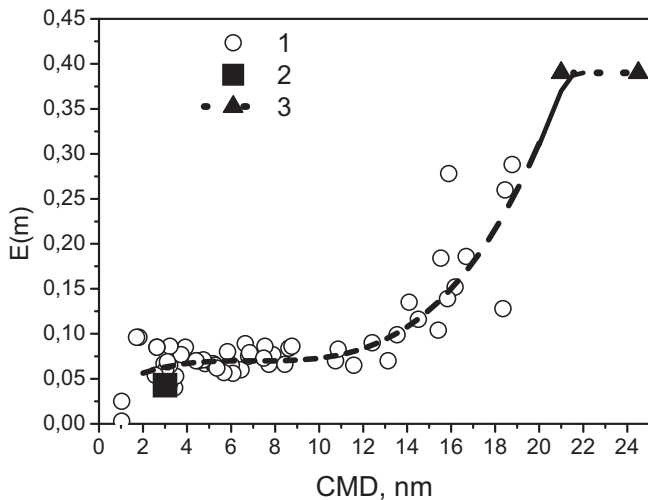


Fig. 10. The dependence of the refractive index function $E(m)$ on the count median diameter (CMD) of growing carbon particles at a wavelength of 1064 nm. 1 – experiment: $T = 1850\text{--}2050$ K, $P = 6\text{--}8$ bar, Ref. [45], 2 – data for nano-organic carbon in the UV range [19], 3 – results of $E(m)$ measurements for usual soot [54]. The dashed line shows the best fit of the experimental data.

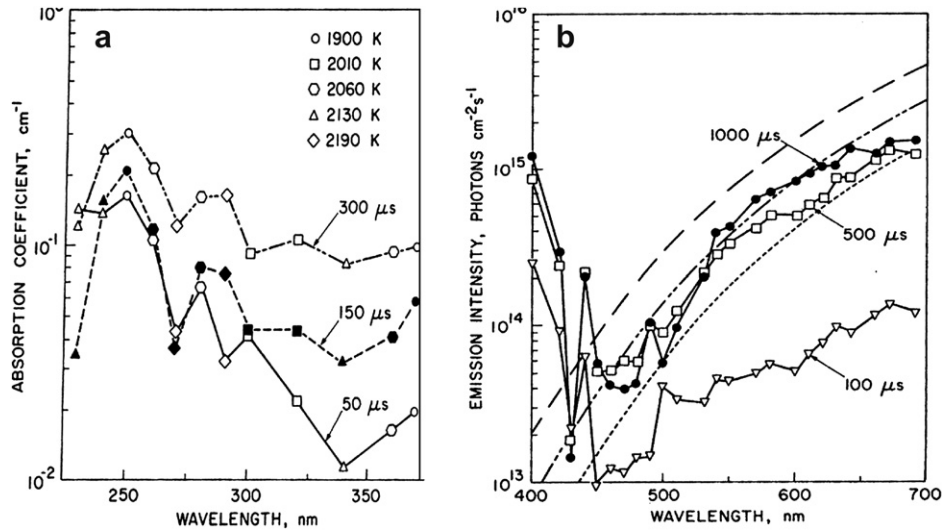


Fig. 12. The spectral distribution of ultraviolet (a) and visible (b) radiation during shock wave pyrolysis of C_7H_8 at different reaction times. The experimental temperature was varied from 1900 K to 2200 K. For comparison, in (b) the corresponding to “black body” emission is shown for — — —, 2000 K; — — — —, 1900 K; and - - - - -, 1800 K. Ref. [29].

$$F_\lambda \equiv \frac{\ln(I/I_0)}{\ln[1 - I_{em}(\lambda, T)/P(\lambda, T)]} - 1 \approx \frac{\varepsilon_{ext}}{\varepsilon_{abs}} - 1 = \frac{\varepsilon_{sca}}{\varepsilon_{abs}} \quad (18)$$

also presents information either about the particle size (again, assuming that $m = \text{Const}$), or about the change of the refractive index m . Here $P(\lambda, T)$ is the intensity of black body radiation in the range $\lambda \pm \Delta\lambda$ at the given temperature T .

Examples of such measurements, performed in [56], are given in Fig. 14 and Fig. 15. It can be seen that $ER_\lambda(1310 \text{ nm}/633 \text{ nm})$ (Fig. 15a) increases during the first 200 μs . This behavior of ER_λ could be qualitatively interpreted as growth in particle size at the early stage of their formation. The function F_λ (Fig. 15b) during the first 300 μs remains close to zero, reflecting the negligible contribution of scattering compared to absorption. This looks reasonable for Rayleigh particles $D \ll \lambda$. Later, the contribution of scattering increases noticeably. This could likely be related to the agglomeration of primary particles to a rather large size. It is notable that the observed behavior of the extinction ratio could be caused by the

change of the refractive index, in particular its imaginary part, responsible for absorption. So, these observations could serve as independent evidence of the essential change in particle optical properties during their growth as described above (see Section 3.2 and Fig. 10).

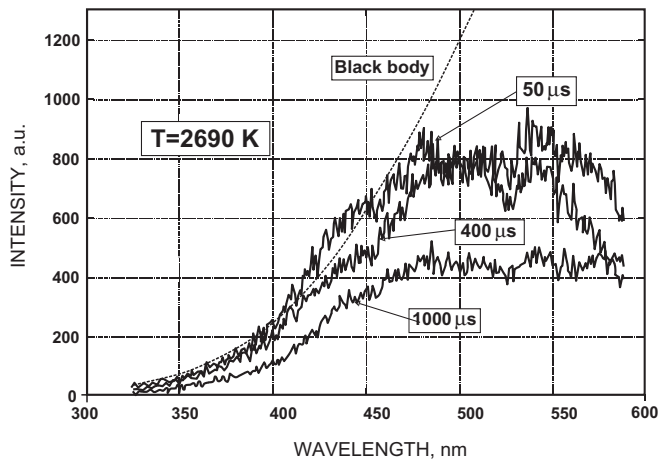


Fig. 13. CCD-camera measurements of particle emission spectrum during C_3O_2 pyrolysis at 2690 K at different times (noisy lines) compared with the black body spectrum distribution (smooth line) calculated for the same temperature and normalized to the experimental curve for $t = 50 \mu\text{s}$ in the spectral range 330–450 nm. Ref. [36].

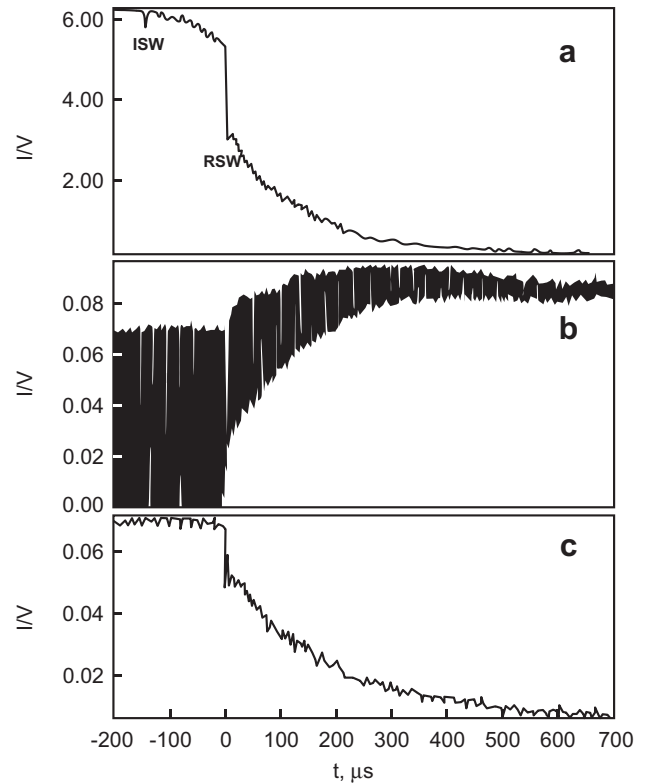


Fig. 14. Typical time profiles of laser extinction and emission at carbon suboxide pyrolysis behind shock waves. a) He–Ne laser extinction (peaks marked ISW and RSW – fronts of incident and reflected shock waves), b) modulated IR-diode laser signal. Lower part of the envelope represents the emission intensity in the range $1.31 \pm 0.05 \mu\text{m}$ and upper part represents the difference in extinction and emission. c) time profile of IR extinction, extracted from the data given on the plot b). Mixture 1% $C_3O_2 + \text{Ar}$, $T_5 = 3083 \text{ K}$, $P_5 = 21.6 \text{ bar}$. Ref. [56].

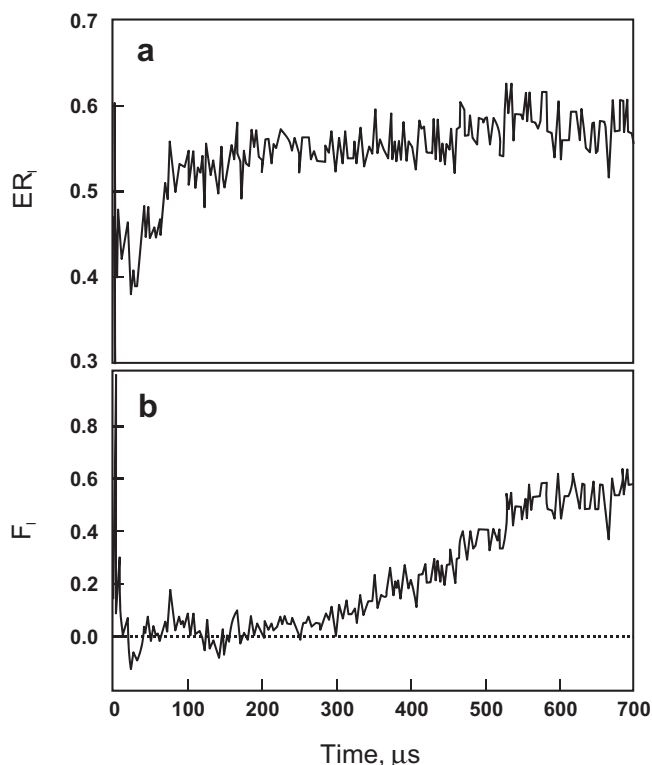


Fig. 15. The time profiles of the extinction ratio for 1310 nm/632.8 nm (function ER_λ (17) – a), and extinction/absorption ratio at 1.31 μm (function E_λ^- (18) – b) behind the reflected shock wave under the experimental conditions shown in Fig. 14. Ref. [56].

3.4. Current particle temperature measurements

One of the major parameters characterizing the process of particle formation is the current temperature of the mixture. In the beginning of this paper (see Section 2), we underlined that one of the most important advantages of a shock tube is reliable control of the temperature of a mixture extracted directly from the measurements of the velocity of the shock wave. However, the thermal processes proceeding during the pyrolysis of initial substances and subsequent nanoparticle formation can essentially influence the current temperature of the mixture. To decrease such effects, the majority of researchers try to work in mixtures containing no more than several percent of reacting substances in an inert gas. Nevertheless, the high energy of the pyrolysis processes often results in an essential deviation of the real temperature of a mixture from the values calculated by the velocity of the shock wave without chemical transformations. A special section of the paper will be devoted to these effects (see Sections 6.1 and 6.2).

As the characteristic time needed for the thermal relaxation of nanoparticles with the surrounding gas at atmospheric pressure is less than 1 μs [59], usually it is not meaningful to distinguish the temperature of the particles and the temperature of the surrounding gas. However, in certain situations, the intensity of non-equilibrium processes is so high that, for some time (usually no more than 10–20 μs), the temperature of the particles could considerably differ from the ambient temperature [57]. Such situations shall be especially considered, and here we will dwell on the methods allowing for measuring the unified temperature of a gas-particle mixture.

It was already noted above that at a known absorption coefficient of particles and total optical density of the investigated volume, measurement of the spectral distribution of intensity of

radiation bears information on particle temperature. However, the temperature measurements based on the simultaneous registration of emission and absorption characteristics of a medium are the most reliable. Application of methods of emission-absorption spectroscopy for investigations of shock heated gases has allowed for simple and high-speed schemes, suitable for the measurement of not only temperatures, but also densities of the population at the molecular states, including under non-equilibrium conditions [14,60–63].

Usage of these methods requires, along with the registration of radiation from the investigated medium, the determination of the absorbing properties in the same spectral range. Emission-absorption methods in the visible and UV spectral ranges, corresponding to electronic transitions in atoms and molecules [60], are now most widespread and developed. However, at temperatures below 2000 K, the intensity of emission signals in the UV and visible ranges sharply decreases; therefore, the most informative measurements are in the IR range, allowing for determining the level of vibrational excitation of molecules of an investigated gas [63]. Among the methods combining measurements of emission and absorption for flame pyrometry, it is possible to allocate one-color modulated absorption-emission (MAE) pyrometry [64], two-colored MAE [65] and a method of temperature measurement in the form of the lines of molecular bands [66]. But, for the measurement of temperature behind shock waves, perhaps the most widespread method has become the so-called generalized spectral line reversal method [14,61].

In Fig. 16, the typical scheme of temperature measurements in a particle-loaded gas mixture by means of the double-beam generalized spectral line reversal method in the IR range [67] is presented. As a reference source, the high-temperature “black body” lamp with Planck radiation spectrum in a wide spectrum range is usually applied.

A peculiarity of spectral temperature measurements in a particle-loaded gas mixture is the presence of emission and absorption of the condensed particles. The spectrum of radiation of particles is usually continuous, therefore it can shield bands and lines in the spectrum of molecules and atoms, which is used for the determination of temperature in the gas medium. Therefore, in particle-loaded mixtures, in most cases, temperature is determined by emission and absorption of the formed particles. If the sizes of particles are in the range of 20–30 nm, the influence of scattering in the visible and IR ranges of the spectrum can be neglected (see Section 3.1) and the all relationships used for the treatment of emission and absorption measurements in a gas mixture can be applied.

Thus, the intensity of the signal from the reference source of the given wavelength, registered by the detector, can be expressed as:

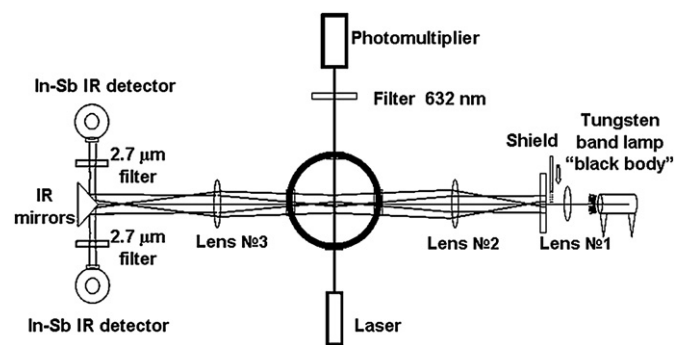


Fig. 16. Schematic of temperature measurements by double-beam generalized spectral line reversal method in the IR range in combination with laser extinction measurements used for carbon particle formation in shock wave pyrolysis processes. Ref. [67].

$$I_0 = A \cdot P(\lambda, T) \quad (19)$$

where A is the instrumental factor and $P(\lambda, T)$ is the Planck function:

$$P(\lambda, T) = \frac{4\pi^2 hc^2}{\lambda^5} \left(\exp \left(\frac{2\pi hc}{\lambda k T} \right) - 1 \right)^{-1}. \quad (20)$$

(k is the Boltzmann constant, h is the Plank constant and c is the speed of light).

The temperature of a reference source T_0 is usually chosen close to the expected temperatures in an investigated mixture. Radiation of a source is divided by the separating plate into two identical channels, one of which in the course of measurements is shielded. This channel serves for the measurement of the intensity of the mixture's emission I_e which at temperature T_m is equal to:

$$I_e = A \cdot [1 - \exp(\varepsilon_\lambda l)] P(\lambda, T_m) \quad (21)$$

where ε_λ is the absorption coefficient and l is the length of the optical pass in the investigated mixture.

Simultaneously to this, the second, open channel records the sum of the mixture's emission and the unabsorbed part of the radiation of the reference source:

$$I_a = I_e + I_0 \exp(\varepsilon_\lambda l) \quad (22)$$

Solving the system of equations (19)–(22), one can obtain the relationship between the reference source temperature T_0 and the mixture temperature T_m :

$$T_m(t) = \frac{h\nu}{k} \left\{ \ln \left[1 + \left(e^{\frac{h\nu}{kT_0}} - 1 \right) \left(1 - \frac{I_a(t) - I_0}{I_e(t)} \right) \right] \right\}^{-1} \quad (23)$$

It can be clearly seen from Eq. (23) that the results of such measurements are determined only by the current magnitudes of the measured intensities $I_e(t)$ and $I_a(t)$ and do not depend on the absolute value of the absorption coefficient and the optical thickness of the investigated mixture. In thermodynamic equilibrium, the measured temperature $T_m(t)$ is equal to the temperature of the mixture independently of the kind of radiating transition. In the simplest case $I_a = I_0$ (exact reversal), the temperature of the mixture T_m is equal to the temperature of the reference source T_0 .

It is easy to see from Equation (23) that the error of the temperature measurements by the described method is determined by the signal/noise ratio of the performed measurements and the relationship between the characteristic temperature of the registered wavelength $\Theta = h\nu/k$ and the measured mixture temperature T_m , as well as by the difference between the brightness temperature of the reference source T_0 and the temperature of the mixture $\Delta T = T_m - T_0$. The maximum accuracy of measurements is reached at $T_m = T_0$. For example, at $T_m = T_0$, a signal/noise ratio of 100 and $\lambda = 2.7 \mu\text{m}$ which corresponds to $h\nu/kT = 3.55$, the error is only 0.3%. On the other hand, with an increase in the difference between T_m and T_0 , the error of the measurements essentially increases, and at $\Delta T = \pm 300 \text{ K}$, it exceeds 20–30%.

Note once again that only the emission or only the absorption measurements require for interpretation additional data on the real form of the spectral lines and instrumental function. Simultaneous measurements of emission and absorption exclude such a necessity which is a distinctive feature of the given method.

In Fig. 17, examples of temperature profile measurements during the formation of carbon nanoparticles during the shock wave pyrolysis of C_3O_2 are shown. Measurements were performed at a wavelength of $2.7 \mu\text{m}$. For an increase in the sensitivity of measurements before the onset of particles in the mixture, 5% CO_2

was added. CO_2 molecules have a strong absorption band in this range of the spectrum and they are quite inert at temperatures below 2500 K. The left plots show measurements in the test mixture 5% $\text{CO}_2 + \text{Ar}$. The measured values of temperature extracted from the Equation (23) are in a good accordance with the calculated values determined from the shock wave velocity (see lower left plot). In the right plots, the results of the measurements carried out in the mixture 3% $\text{C}_3\text{O}_2 + 5\% \text{CO}_2 + \text{Ar}$ are given. Besides measurements by the double-beam generalized spectral line reversal method at $2.7 \mu\text{m}$, laser extinction measurements at 633 nm, directly reflecting the formation of condensed particles, have been carried out. The lower temperature plot extracted from the experimental data shows an essential temperature increase simultaneously with the growth of the particles, reflecting release of the heat of condensation. The description of this phenomenon will be presented below in Section 6.2.

3.5. Method of laser-induced incandescence

New possibilities for the diagnostics of nanoparticles were opened by active developments in recent years in the method of laser-induced incandescence (LII), which was proposed for the first time by Melton [59]. This method has been widely used in the analysis of particles in stationary conditions (flames, exhaust jets, etc.) [68–71]; however, it was recently applied in shock tubes [36,45,72–75]. The method is based on fast nanoparticle heating by a laser pulse and the analysis of registered thermal radiation of nanoparticles, heated above the initial temperature. The intensity of the LII signal is proportional to the volume concentration of the condensed phase, and the time of decay depends on the size of the nanoparticles. Thus, the method allows for performing measurements on particle size, their total concentration, and in certain situations, their properties. Unlike scattering measurements, LII measurements weakly depend on the optical properties of particles; however, they extremely strongly depend on the efficiency of energy exchange between the laser-heated particles and the surrounding gas. This circumstance sometimes brings serious uncertainty to the measurements, some examples of which will be described below.

Other problem is connected to the fact that besides LII signals, as a result of the action of a laser impulse in the mixture, radiation can emerge caused by the effect of laser-induced fluorescence (LIF) from PAH molecules and the precursors of soot [76]. The intensity of the LIF signal essentially depends on the wavelength of laser radiation; it is well known that in the majority of small molecule fluorescence is caused only by UV radiation; however, heavier molecules, including PAH and soot precursors, can fluoresce under the influence of visible radiation. This effect of laser influence at $\lambda = 532 \text{ nm}$ has been investigated in some studies [77,78]. Thus, authors have noted that the duration of the LIF signal should not be more than 50 ns; therefore; for an exception of the influence of fluorescence on measurements of LII signals, some authors have excluded an initial part of the signal in the analysis of performed measurements. It is important to note that when using a laser with a wavelength of 1064 nm, these fluorescence signals are not observed. This fact has allowed authors [77,78] to apply two-wave excitation at 532 nm and 1064 nm to perform simultaneous measurements of LIF from PAH and soot precursor signals and LII signals from soot particles.

A typical scheme of two-channel time resolved LII measurements is presented in Fig. 18. As a source of nanoparticle heating, a pulsed Nd:Yag laser at a wavelength of 1064 nm with the pulse time about 10 ns is usually used. The time-resolved signals of incandescence are registered on two wavelengths in the optical range by means of the registration device, which includes the two-

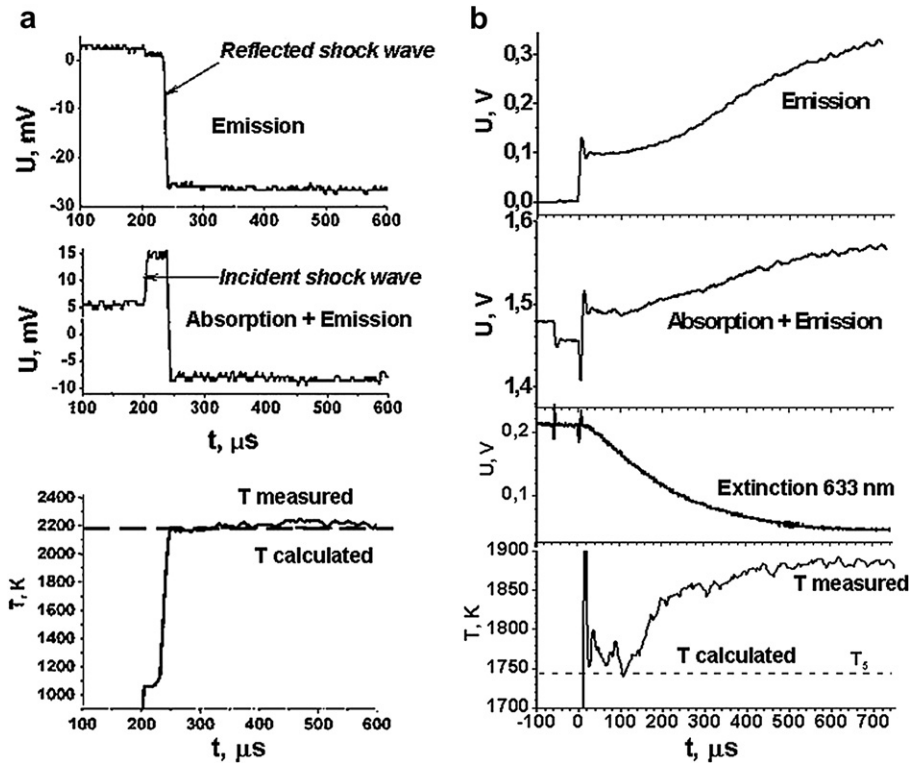


Fig. 17. Examples of temperature measurements by double-beam generalized spectral line reversal method at $2.7 \mu\text{m}$ (a) test mixture 5% $\text{CO}_2 + \text{Ar}$. (b) carbon particle formation in the mixture 3% $\text{C}_3\text{O}_2 + 5\% \text{CO}_2 + \text{Ar}$; initial temperature behind the shock wave was $T_5 = 1743 \text{ K}$; temperature of reference source was $T_0 = 1690 \text{ K}$. Ref. [67].

channel optical scheme from lenses, half-transparent mirrors and filters, and two photomultipliers. The obtained data are recorded in a digital oscilloscope with a pass-band not less than 500 MHz.

An example of LII signals is presented in Fig. 19. As a result of laser heating, particle radiation over several nanoseconds reaches a maximum, and then decreases due the cooling process.

For the analysis of the results of these measurements, a corresponding model of laser-induced incandescence based on the laws of energy and mass conservation during heating by the laser pulse and the subsequent cooling processes of the nanoparticles has been developed [45,59,71,79,80]. The energy of the nanoparticles, obtained by a laser pulse, is consumed by convective heat exchange with molecules of the surrounding gas, by the thermal radiation of nanoparticles and by their evaporation. The shape of nanoparticles in the model is usually accepted as spherical which allows simplifying the calculations, and deviations from the spherical form (<20%) do not result in noticeable alterations in the description of radiation time-profiles [81].

For the majority of conditions in which LII measurements are carried out, convective heat exchange proceeds in a free-molecular regime due to collisions between nanoparticles and the molecules of the surrounding gas. The basic uncertainty in the calculation of convective heat exchange in a free-molecular regime is related to the magnitude of the accommodation factor of the thermal energy of the molecules of the surrounding gas on the surface of nanoparticle α .

In the first studies on LII, the accommodation factor was accepted as equal to 1 [71,75,79], i.e. it was assumed that the molecules of the surrounding gas after a collision with a particle obtain a kinetic energy determined by the current temperature of the particle. Later, the modeling calculations showed that α , as a rule, is much less than 1 and depends as on the weight and

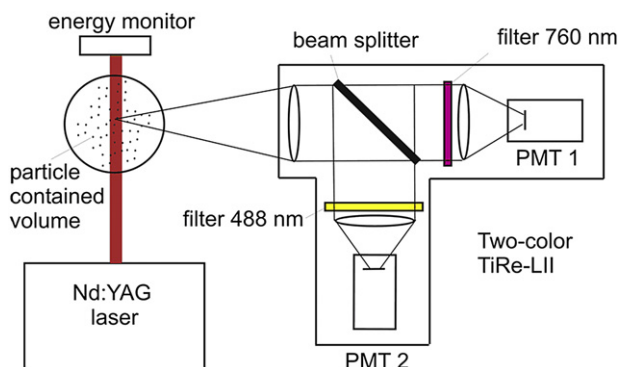


Fig. 18. Setup for LII measurements. Ref. [45].

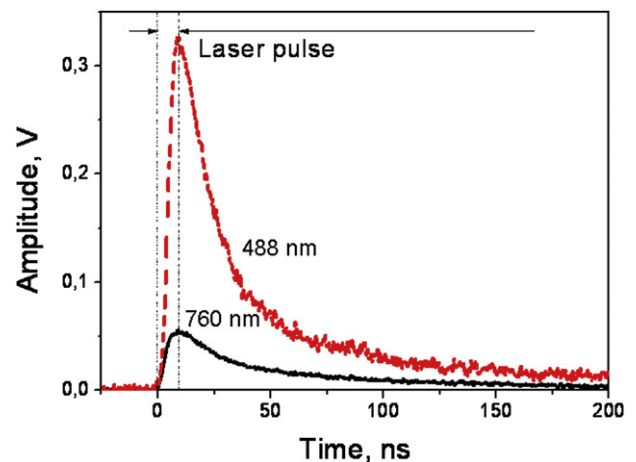


Fig. 19. Typical LII signals from carbon nanoparticles at two wavelengths. Ref. [45].

structure of the colliding gas molecule [82], as well as on its temperature [83].

For carbon nanoparticles, the magnitude of this factor in different references varies from 0.2 to 1 [71]. The uncertainty of α can be eliminated, by using diagnostics with independent measurements of nanoparticle sizes by other methods in addition to LII [84–86].

If a nanoparticle heats up to temperatures exceeding its temperature of evaporation, atoms or larger clusters can leave a particle surface. It is usually assumed that a substance evaporated from a nanoparticle remains in the gas (vapor) phase and the vapor temperature is equal to the temperature of the nanoparticle [87]. An analysis of the contribution of carbon atoms and small clusters C_2 – C_{10} to heat losses in the evaporation carbon nanoparticles was carried out in [80]. According to their conclusions [80], it is usually assumed that all clusters evaporated from a particle surface are C_3 clusters (molecular weight is $W_V = 36$ g/mol), i.e. their contribution in the general flux of carried-away substances is much higher than the contribution of other clusters. The value of the enthalpy of vapor formation for these clusters is $\Delta H_V = 7.78 \times 10^5$ J/mol [88]. For determination of carbon vapor pressure over the surface of a carbon nanoparticle, the data for graphite $P_{ref} = 1$ bar and $T_{ref} = 3915$ K [80] are usually used. The value of the energy of the laser pulse absorbed by the nanoparticle is determined by the function of particle refractive index $E(m)$ (16), which generally should depend both on the particle size and on the wavelength of laser radiation. However, in the absence of such data for any carbon nanoparticles, the majority of authors use empirical dependence $E(m)$ for wavelengths in the visible and near-IR range for soot, which are presented in [54,89–91]. One commonly used relation: $E(m) = 0.232 + \lambda(1.2546 \times 10^3 \text{ cm}^{-1})$ has been suggested in [54].

The solution of the system of differential equations for the conservation of energy and mass relative to the current temperature of the nanoparticle $T_p(t)$ allows for presenting the LII signal at wavelength λ from a single spherical nanoparticle with a diameter D and temperature T_p , at a surrounding gas temperature T_g in the form of [86]:

$$S_d(t) = C \cdot \left[\frac{D^3}{\exp\left(\frac{\chi \cdot T_g}{T_p(t)}\right) - 1} - \frac{D_0^3}{\exp(\chi) - 1} \right] \quad (24)$$

where:

$$\chi = \frac{h \cdot c}{\lambda \cdot k \cdot T_g} \quad (25)$$

Here, D_0 is the initial particle size before evaporation and C is the instrumental factor. An integral signal of the ensemble of nanoparticles with the size distribution $p(D)$ (8), is:

$$S(t) = \int_{d_1}^{d_2} S_d(t, D) \cdot p(D) \cdot dD \quad (26)$$

Since the size of a nanoparticle is determined only by the decay time of the LII signal (cooling time), in the model, the normalized magnitudes of the calculated signal are used, which allows for avoiding exact knowledge of the constant C in calculations. Due to this, the normalized experimentally-measured LII signal at the chosen wavelength is approximated by a calculated curve (26) through a variation of the count median diameter (CMD) of the nanoparticle and a geometrical deviation σ_g from the average size. In the field of values CMD and σ_g , the method of least squares searches for the best solution. If measurements of the LII signal are performed at two wavelengths simultaneously, the maximum amplitude of experimental LII signal at the second wavelength can be used for the selection of value of the function $E(m)$. The example of such LII data processing allowed for determining the dependence of $E(m)$ on particle size, as given above (see Section 3.2 and Fig. 10).

Thus, the model allows for describing incandescence signals from laser-heated carbon nanoparticles with any content of the surrounding gas and at temperatures from 300 to 3000 K. Since, in the model, the convective mechanism of particle heat exchange with the surrounding gas is considered, it is not applicable at Knudsen numbers less than 1, which approximately corresponds to a range of elevated pressures more than 10 bar.

In Fig. 20, examples of size time profiles of growing nanoparticles measured during the pyrolysis of propane and benzene at various temperatures and concentrations behind shock waves [75] are shown. One can see that the method allows for analyzing nanoparticle growth starting from sizes around 2–4 nm. Note, however, that in this study, the optical properties of the particles independent of their size were considered corresponding to normal soot, and the accommodation factor α was assumed to equal 1, which could cause serious inaccuracies in the absolute values of the extracted particle sizes. In a later work [45], both of these imperfections were eliminated. In this study, the two-color time resolved LII measurements allowed for independent measurements of $E(m)$ (see Fig. 10) and particle size. Additionally, the corrected value of the accommodation factor $\alpha = 0.23$ was taken from [92]. In Fig. 21, the particle size time profiles during acetylene pyrolysis at different temperatures, measured in [45], are shown.

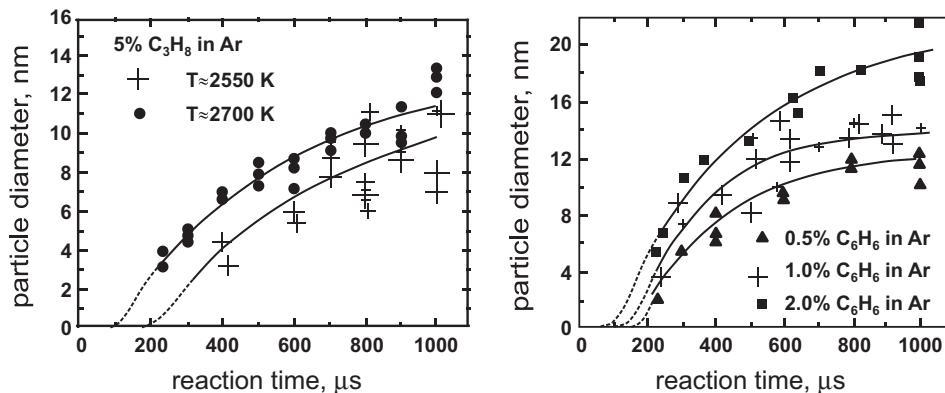


Fig. 20. Soot particle diameter of a monodisperse distribution measured at different reaction times during the pyrolysis of C_3H_8 /Ar (left part) and of C_6H_6 /Ar (right part). Lines – best fit of experimental data. Ref. [75].

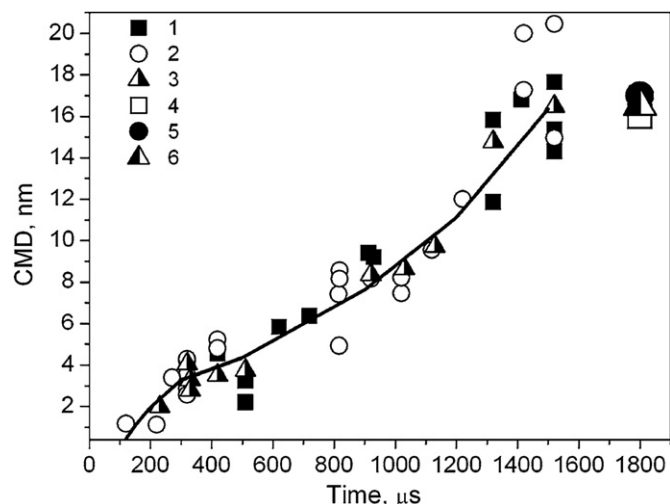


Fig. 21. The results of LII measurements of increasing carbon particle sizes during acetylene pyrolysis at different temperatures and final carbon particle sizes obtained by TEM. Symbols: 1, 2, 3 - LII measurements at temperatures 1850 K, 1950 K, 2050 K, respectively; 4, 5, 6 - corresponding results of TEM sizing; lines - best fit of the experimental data. Ref. [45].

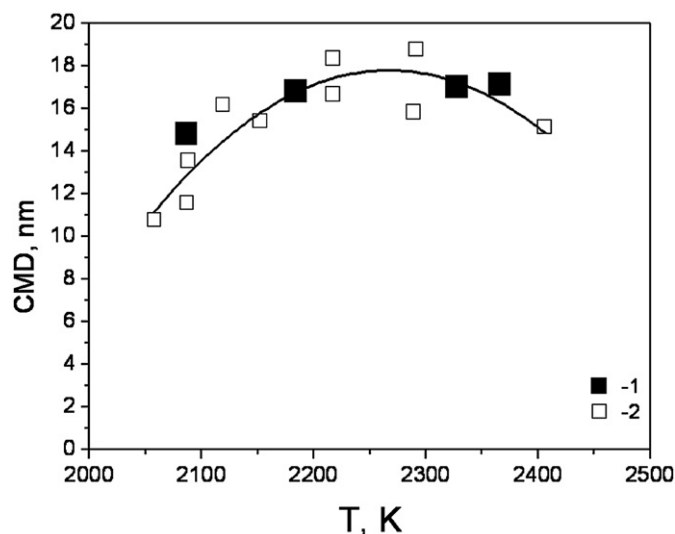


Fig. 23. Final size of carbon nanoparticles obtained during shock wave pyrolysis of a mixture of 3% C_2H_2 + Ar measured by TEM (1) and LII (2). Curve is an approximation of the experimental data. Ref. [93].

In Fig. 22 and Fig. 23, the temperature dependence of the final sizes of soot particles formed during the pyrolysis of benzene [72] and acetylene [93] are demonstrated. In both works, LII data were verified by direct measurements of the final sizes of the obtained nanoparticles. For this, samples of particles deposited on the walls of the shock tube at the end of experiment were analyzed by transmission electron microscopy (TEM). For the calculation of particle size from LII measurements in [45], the optical properties of soot and the accommodation factor $\alpha = 0.23$ were used. Apparently, comparison of the data on particle sizes obtained by LII and electronic microscopy, shown in Fig. 23, fit well with each other, and the selected values of a standard deviation from the average size $\sigma = 1.1$ are also in a good accordance with the data from electronic microscopy. Note, however that mature particles collected after experiments could differ from the young particles registered by LII; therefore, such a comparison has in a certain sense a qualitative character. The reasons for possible differences in

the particles observed by LII and collected from the walls of the shock tube and some attempts to overcome this problem are described below in Section 3.7.

It is interesting to note that the temperature dependence of the final sizes of the particles, measured by LII, reproduces the bell-shaped temperature dependence of particle yield, measured by extinction (see Section 3.1 above). In [36], such simultaneous measurements of the sizes and relative yield (or normalized optical density) of carbon particles formed under hydrogen-free conditions in the pyrolysis of C_3O_2 and CCl_4 have been performed in a wide range of temperatures. A comparison of these dependences is shown in Fig. 24. The analysis of the true reasons for such a remarkable similarity of these dependences will be given below, in the section devoted to finding the generalized temperature dependence of the processes involved in the formation of carbon nanoparticles (see Section 7.1).

3.6. Time resolved time-of-flight mass spectrometry

A basic feature of the process of formation of condensed particles in gas phase reactions is the extremely wide mass range of the molecules, radicals, clusters and particles participating in the reaction. In the early stages of the process, more and more heavy gas molecules and clusters are formed, which increase in their mass numbers up to 1000 amu (which corresponds to 84 carbon atoms and a size of about 1 nm) and start to acquire properties of condensed particles [94–96]. Diagnostic methods for gas reactions in shock waves are widely described in the literature (see, for example [8,14,61,97]) and their description is beyond the present review; therefore, all methods described above in Sections 3.1–3.5 concern diagnostics of the late stages of the process, beginning with the inception of condensed particles. The problem is that heavy molecules and clusters, formed at an intermediate stage of the process with mass numbers ranging from several hundred to several thousand amu have an extremely complex spectrum of absorption in the UV range. They are difficult to resolve by molecular spectroscopy methods, but they are still rather transparent in the visible range, therefore they cannot be registered by the extinction methods, scattering and LII described above.

From this point of view, time-of-flight mass spectrometry (TOF-MS) is perhaps the unique diagnostic means which allows

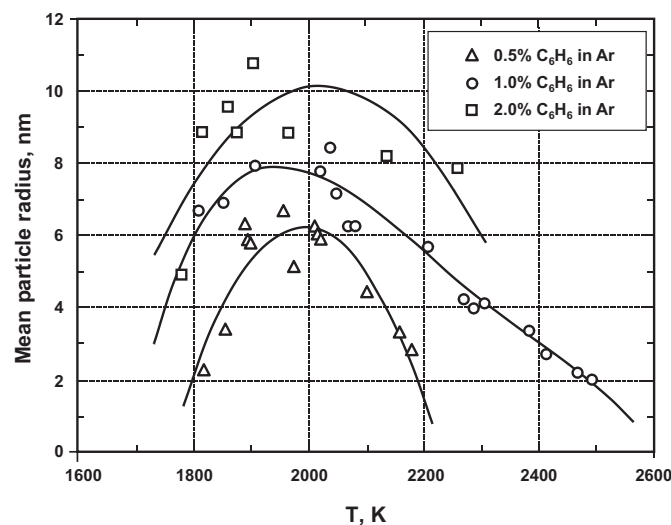


Fig. 22. Mean particle radius for a fixed reaction time of $t = 1$ ms versus temperature. Curves show the approximate behavior of soot yield at the same reaction conditions. Ref. [72].

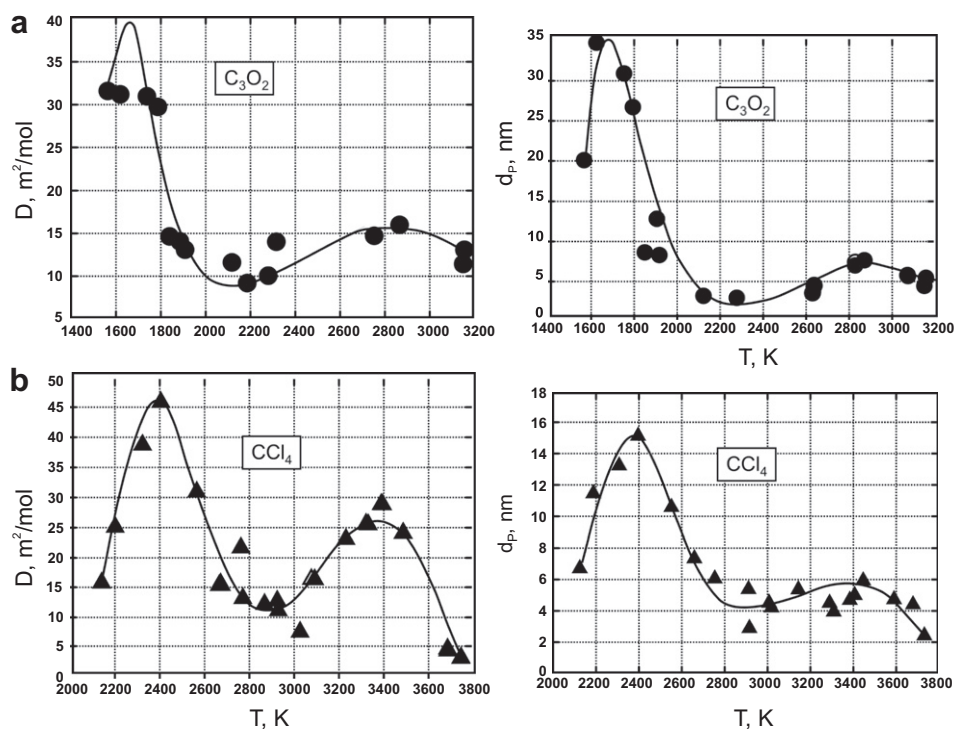


Fig. 24. Temperature dependencies of the normalized optical density D_n and particle size D during the pyrolysis of C_3O_2 (a) and CCl_4 (b), measured at the fixed time 1 ms after the reflected shock wave passage through the measuring section. $P = 1.3\text{--}4.5$ bar. Ref. [36].

registering heavy hydrocarbon radicals and carbon clusters with mass numbers above 50–100 amu. The main difficulty in the application of TOF-MS diagnostics for shock tube experiments is that the particles arriving at the mass spectrometer have passed through a system of skimmers from the test section of the shock tube to the high vacuum chamber, where any collision processes are “frozen”. In this zone, particles are exposed to the influence of an ionizing electric field, and the time of flight of particles (which is greater with a higher particle mass) is often comparable or exceeds the time of particle growth behind a shock wave. Therefore, excited and ionized particles may have time to undergo spontaneous decay, and the mass content of a mixture registered by a spectrometer can differ from the initial mixture contents in a shock tube. These problems seriously hamper the application of MS methods for shock wave investigations.

Early studies of the kinetic processes in shock waves with the use of TOF-MS were carried out in 1960s in classic works by Kistiakovsky and coauthors [98,99]. However, wide application of this technique in shock tubes started in the works of Kern and coauthors [8,97,100–103]. In these studies, the authors managed to measure the time profiles of various hydrocarbon radicals with mass numbers of the order of 100 amu and above a time resolution of about 10^{-5} s. In the last decade, a new generation of shock tube TOF-MS has been developed, primarily for applications in high temperature reactions important in combustion [104,105].

The apparatus described in [104] takes advantage of modern instrumentation to enhance the data acquisition rate of the mass detector. The construction of sampling of the gases from the shock tube has also been seriously modified. The shorter time intervals in the new instrument improve the resolution in the early stages of the reaction from which rate coefficients can be best determined for the initial reactions. The sampling interface between the shock tube and TOF-MS has been designed to minimize the effects of the end wall thermal boundary layer that can severely compromise

chemical kinetic measurements. Furthermore, this interface increases the range of pressures in the shock tube to about 10^3 mbar, yet remains compatible with the necessary high vacuum in the TOF-MS, about 10^{-5} mbar. In Fig. 25, the typical concentration profiles measured by TOF-MS during the pyrolysis of cyclohexene behind the shock wave are shown [104]. Evidently, this kind of measurement represents a novel step in the investigation of the kinetics of high molecular species. It is likely that within the next few years one can expect new distinguished results obtained with the usage of this diagnostic.

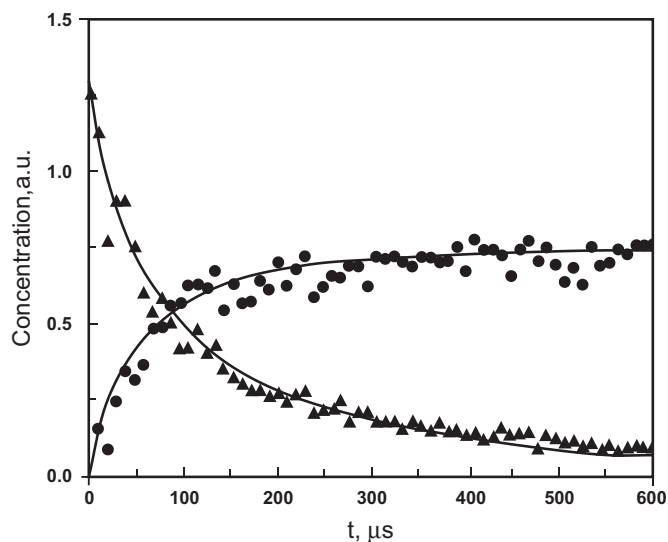


Fig. 25. Concentration time profiles for the reaction $C_6H_{10} = C_4H_6 + C_2H_4$ measured by TOF-MS combined with shock tube. $P = 0.81$ mbar, $T = 1424$ K; \blacktriangle cyclohexene; \bullet ethylene; — simulation. Ref. [104].

3.7. Post-shock analysis of formed nanoparticles

Carbon nanoparticles, formed during a shock wave experiment, and deposited on the walls of the shock tube or substrates specially placed in the shock tube, could be exposed to detailed analysis by means of transmission electronic microscopy of low or high resolution (LR and HR TEM), raster electron microscopy (REM), diffraction electronic microscopy (MDF), X-ray structural and elemental analysis, Raman spectroscopy, etc. The examples of the most typical electronic exposures of carbon nanoparticles formed during shock tube pyrolysis experiments are shown in Fig. 26 and Fig. 27. From the low resolution exposures, it is possible to measure the particle size distribution, and the data from high resolution TEM and MDF allows for studying the structure of the obtained particles.

Besides the methods of electron and X-ray spectroscopy, in recent years, new methods of laser desorption-ionization time-of-flight mass spectrometry (LDI-TOFMS) have been successfully applied to the analysis of gaseous species adsorbed by soot particles [107–110]. At first, this technique was used to investigate soot precursors in flames by means of laser microprobe mass spectrometry (LMMS) [107]. It was shown that this method could clearly detect many species in the 200–300 amu range which characterizes the polycyclic aromatic hydrocarbons (PAHs). Subsequent modification of LDI-TOFMS applied for the investigation of samples of soot formed in flames [108] and behind shock waves [109,110] presented valuable data on the nature of gases (mainly PAHs) which are absorbed by soot particles and soot precursors with masses up to ~ 2000 amu. In Fig. 28, the examples of mass spectra in the range of 350–380 amu obtained from soot formed by toluene and thiophene pyrolysis behind the shock wave and the correlated PAH species [110] are shown.

However, within the limits of the given review, we will not dwell on the detailed description of the cited methods, as all of them have been widely applied to the analysis of carbon nanoparticles synthesized by other methods (see for example the recent reviews [1,111,112]).

Let us note here only two important circumstances. First, the results of the post-experimental analysis of particles are very important for independent control and verification of various measurements obtained during the experiment. For example, the absolute sizes and distributions of the sizes of the particles, determined by electron microscopy methods, can be compared

with the final sizes of particles, measured directly in the course of the reaction by scattering methods and LII. The example of such a comparison is demonstrated above (see Fig. 23). The structure and elemental content of the formed particles give important additional information in the analysis of the kinetic mechanisms and thermodynamic parameters of the growing particles. Additionally, all methods for the post-shock analysis of formed particles have special importance for the elaboration of practical methods for the synthesis of various types of carbon nanoparticles for applications in industry.

On the other hand, the specificity of shock tube experiments is that after the termination of “working time” which is, as a rule, no more than several milliseconds (see Section 2), the investigated mixture is exposed to complex gas dynamic processes including secondary shock waves, rarefaction waves, turbulent mixing with the driving gas, etc. During these processes, the pressure, temperature and mixture content are changed in uncontrollable ways. Therefore, the properties of the particles deposited on the tube walls or substrates can essentially differ from those observed at the end of the working time of a shock tube.

To overcome such uncertainty, some researchers have used a method of instant “freezing” of formed particles by the supersonic expansion of an investigated mixture into the vacuum chamber through a small outlet in one end plate of a shock tube [36,113]. However, even in this case, it is impossible to exclude the possibility of changes to the properties of young particles in a supersonic flow. So, for example, the big (to 100 nm in diameter) hollow spheres observed in [36] could have a similar origin.

Summarizing the review of diagnostics methods for the process of formation of carbon particles behind shock waves, it is possible to conclude that modern methods can determine not only such integrated parameters as the volume fraction of the condensed phase, particle yield and their number density, but also more detailed characteristics of the particles, such as their current size, refractive index and current temperature. Based on such experimental data, various groups of investigators have accumulated a huge volume of scientific information on the kinetic characteristics of the process of nanoparticle formation, the properties of formed particles, the thermodynamics of pyrolysis and particle formation processes, etc., for a wide range of concentrations, temperatures, pressure and of some other determining parameters of pyrolysis.

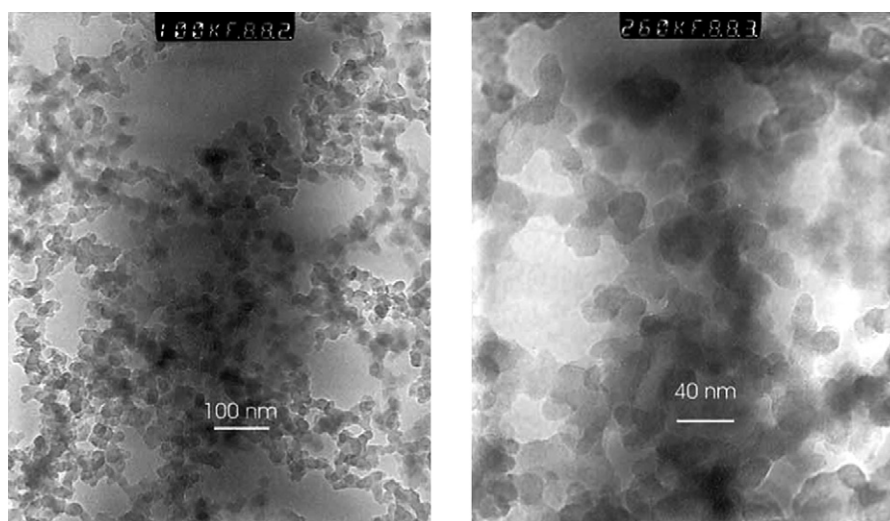


Fig. 26. TEM micrographs of soot formed in shock wave pyrolysis of the mixture 2% C_6H_6 in Ar, $T = 1903$ K, $P = 1.21$ bar. Ref. [72].

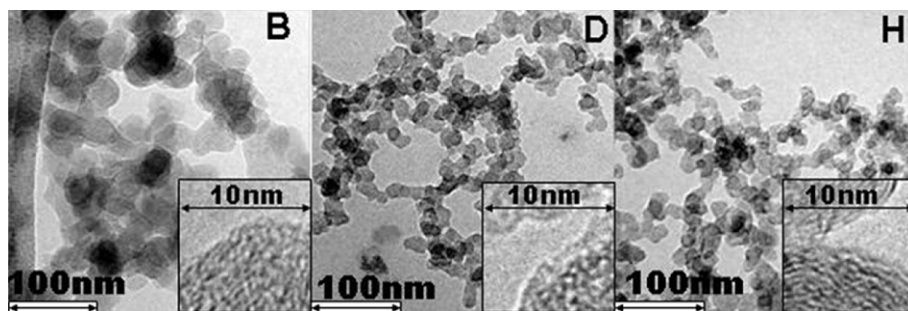


Fig. 27. Low and high resolution (insertions) transmission electron microscope images of carbon nanoparticles formed behind shock waves in 20% C_3O_2 (B), 20% $\text{C}_3\text{O}_2 + 10\% \text{H}_2$ (D) and 20% C_2H_2 (H). Ref. [106].

4. Kinetic characteristics of the particle formation process

4.1. Induction time of particle inception τ_{ind}

The time profiles of yield, and the volume fraction of particles listed above as well as their sizes and optical properties, extracted from these measurements, allow for analyzing the basic kinetic characteristics of nanoparticle formation. Since the process of formation and growth of particles is only the final stage of a complex set of pyrolysis processes initiated by a shock wave, in most cases it is possible to observe a distinct delay in the appearance of any signals of the measurements connected with particles relative to the moment of the passage of a shock wave. Therefore, since the earliest

investigations of carbon nanoparticle formation in shock waves one of the major characteristics of this process is assigned – an induction time of particle inception τ_{ind} [6,114,115]. In the majority of works this time is determined from extinction measurements [26,31,33,51,115], though the emission measurements data [22,114] are also sometimes used for this purpose. The quantitative value τ_{ind} is usually defined as the intersection of the inflectional tangent to the extinction profile with the time axis (see Fig. 3).

Whereas shock tube experiments easily allow varying of the temperature of a process, practically in all works a temperature dependence of induction time has been measured, and it has been noticed that τ_{ind} quickly reduced as temperature increased. Usually these dependences are represented in Arrhenius coordinates $\ln \tau \sim 1/T$. In the Fig. 29 and Fig. 30 show examples of experimental measurements of induction time of soot appearance at pyrolysis of various precursors, measured by extinction profiles at 633 nm. One can see that they really do obey Arrhenius-like behavior.

As is well known, the slope of these dependences determines a barrier (activation energy) of the reaction described. The value of activation energy of the reactions, comprising the induction time of particle inception for different substances, varies in a range of

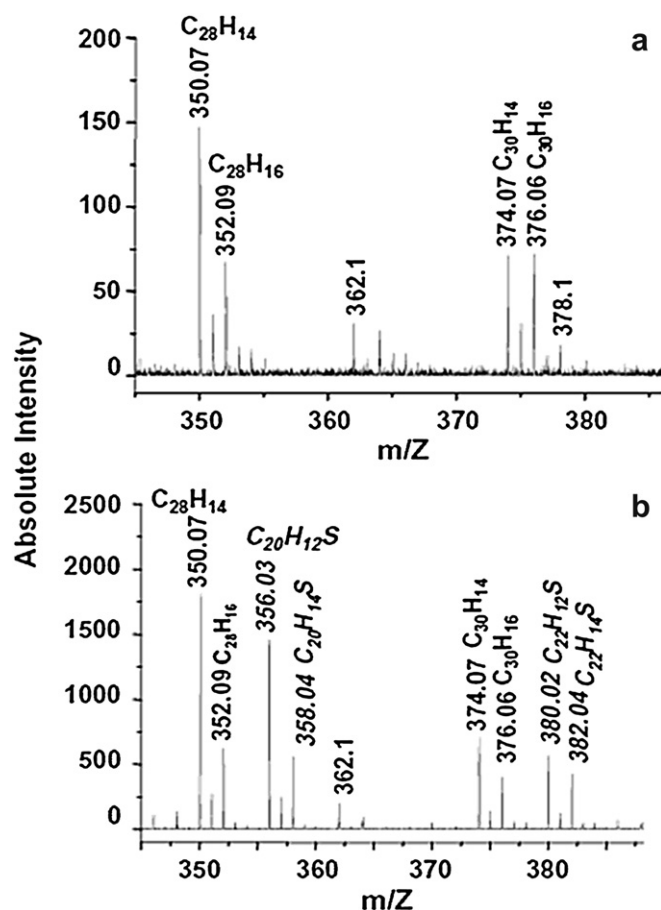


Fig. 28. LDI-ToFMS spectra obtained from soot formed by toluene (a) and thiophene (b) pyrolysis behind shock waves. Ref. [110].

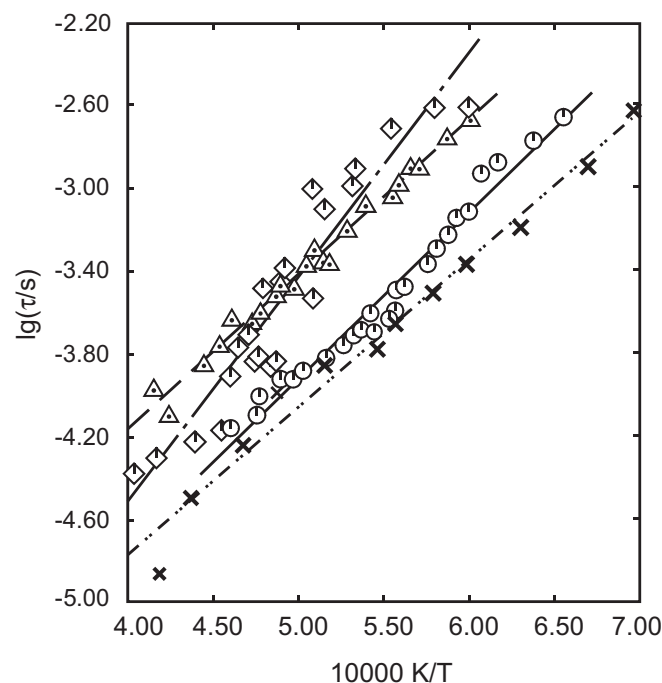


Fig. 29. Induction times for soot appearance determined at 633 nm for acetylene (\diamond); allene (\circ); 1,3-butadiene (Δ) and toluene (\times). Ref. [26].

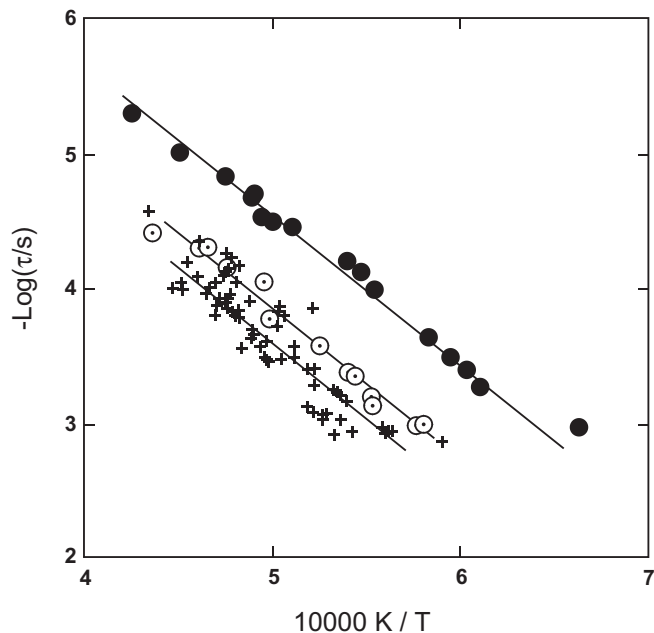


Fig. 30. Arrhenius-type plot of $\log(1/\tau_{\text{ind}}) \sim 1/T$ for benzene (●); ethylene (○) and n-hexane (+) measured by extinction at 633 nm. Ref. [31].

100–300 kJ/mol (see Table 1). To comprehend the reason for the strong temperature dependence of induction time, it is once again emphasized that this time characterizes the complexity of reactions beginning from the mixture heating in a shock wave front, up to the occurrence of the condensed particles actively absorbing laser radiation. Among all these reactions, the primary dissociation of the initial molecules possesses the greatest activation energy, while, the subsequent exchange and recombination reactions, as a rule, have no considerable energy barriers and proceed at higher rates. Therefore it is possible to draw the conclusion that the induction

times are determined by the rates of the early stages of pyrolysis, consisting of the endothermic reactions of primary molecule decomposition.

Analyzing the dependences of absolute values of induction times on the type of precursors, many authors noticed that the greatest times are observed in the saturated hydrocarbons. Olefins have shorter times; while the aromatic hydrocarbons are characterized by the shortest induction time of particle formation (see Figs. 29–31). Note that in hydrogen-free precursors induction times still essentially appear shorter (see Fig. 32).

The next problem concerns the dependence of induction time on concentration. Since the parameter τ_{ind} is intrinsically a phenomenological characteristic of process and it cannot be adhered directly to any specific chemical reaction during pyrolysis, the order of this reaction, i.e. its dependence on concentration of a precursor and a total pressure of a mixture, is a priori also not clear. Experimental data on τ_{ind} obtained both from extinction and emission measurements indicate considerable stratification of the points measured at different pressures and concentrations of carbon bearing molecules [20,22,31,118] (see examples in Fig. 33a, b). Attempts to generalize the dependences obtained has led various authors to completely different degrees of n and m in the following equation:

$$\tau_{\text{ind}} = A \exp(E/RT) [C]^{-n} [M]^{-m} \quad (27)$$

(see Table 1). Usually authors do not consider the dependence of τ_{ind} on concentrations of gas-diluter $[M]$, and therefore index m is accepted as equal to 0. Quite weak dependence of τ_{ind} on argon concentration ($m = 0.179$) was only observed in [26]. On the other hand, the dependences of induction time on carbon concentration are characterized by rather wide dispersions of indexes n . One can see from Table 1 that this index varies from 0.23 up to 1.57, and in this case an effective energy of activation E also changes. Note that some authors, following the correlation of ignition delay [10], have postulated the simplest case $\tau_{\text{ind}} \sim [C]^{-1}$ [6,22,106,117].

It is necessary to emphasize one circumstance. We have already considered the change of the optical properties of carbon particles in their growth process (see [34,45]). This phenomenon should

Table 1

Approximations of experimental data on induction time of carbon particle formation, according formula (27) used in different works.

	Index n	Index m	E (kJ/mol)	Ref.
CH ₄	0.35	0	145	[48]
C ₃ H ₈	0.42	0	149	[48]
C ₇ H ₁₆ n-heptane	0.46	0	149	[48]
Heptylbenzene	—	—	180	[116]
1-Methylnaphtalene	—	—	183	[116]
C ₂ H ₂	0.41	0	130	[22]
	0	0.179	92	[26]
	0.84	0	122	[26]
	(3.39 μm)			
	0.75	0	228	[33]
	1	0	276	[106]
	1	0	270	[115]
			($T > 2000$ K)	
	1	0	115	[115]
			($T < 2000$ K)	
C ₂ H ₄	0.23	0	117	[22]
	0.45	0	141	[48]
C ₂ H ₆	0.42	0	151	[22]
C ₆ H ₆	0.75	0	260	[31]
Toluene	1.57	0	181	[27]
	—	—	189	[116]
C ₃ O ₂	0.5	0	183	[20]
			($T > 1750$ K)	
	0.5	0	103	[20]
			($T < 1750$ K)	
	1	0	226	[106]

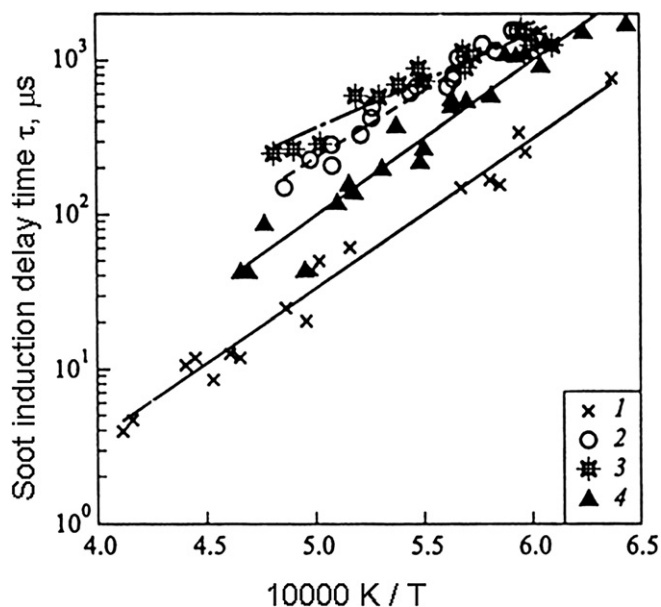


Fig. 31. Arrhenius-type plot of induction time for different hydrocarbon/argon mixtures. Carbon concentration in all experiments is $[C]_5 = (1.9 \pm 0.4) \times 10^{19} \text{ cm}^{-3}$. 1 – toluene, 2 – 1-hexene, 3 – iso-octane and 4 – ternary mixture [117].

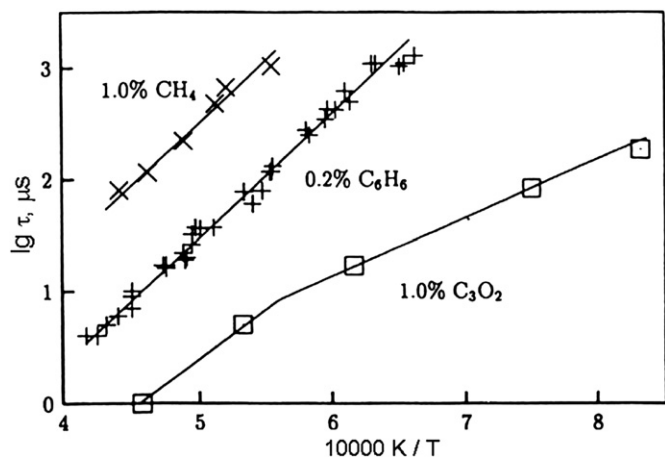


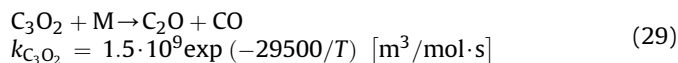
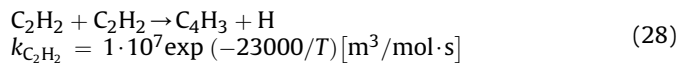
Fig. 32. Induction time in carbon suboxide pyrolysis compared with those of methane and benzene at similar carbon concentrations. $P_5 = 55$ bar. Ref. [20].

inevitably affect the extinction (and emission) measurements. Thus, measured induction times can essentially differ depending on the wavelength at which extinction measurements are made. Different authors have paid attention to this fact [26,34], however the unified approach to such data in the literature has not been developed. Note, for example, that rise in extinction at 633 nm, interpreted in [34,42,45] as a sharp change in the particle refractive index at this wavelength upon the increase in their sizes above 5–10 nm, can be also be caused by the appearance of the heavy PAH, for which the absorption spectra extend in the process of their growth from UV to the visible range up to 500–600 nm [119].

Therefore during the analysis of dependence of an induction time on the concentration of reagents it is necessary to consider the influence of concentration on the size of particles formed. In the literature there are few such measurements, one of examples on particle growth in benzene [75] is shown in Fig. 20 (right). One can see from this plot that the final size of the particles increases approximately as $[C]^{0.5}$, while the time of achievement of the current size of particles (for instance 10 nm) is reduced approximately as $[C]^{-1}$.

We have tried to summarize a considerable quantity of various data, and we can suppose that the most plausible value of n is unity, corresponding to the initial dissociation reactions which often represent a rate limiting step for the whole process (see above), and all deviations from this dependence are most likely caused by the neglect of changes of the optical properties of particles at the early stages of their growth, which corresponds to the induction time.

Interesting conclusions have recently been drawn from the comparison of data on the induction time in acetylene and carbon suboxide [106] (see Fig. 34). One can see that from the given coordinates, the magnitudes of $\ln \tau_{\text{ind}}[C]$, plotted versus the reversal calculated ("frozen") temperature behind a shock wave $1/T$, do not practically show any dependence on carbon concentration varying from 0.03% to 30%. This fact not only confirms the legitimacy of the generalization $\tau_{\text{ind}} \sim [C]^{-1}$, but also the insignificance of thermal effects at this stage of the process. In reality, as it will be shown in Section 6.1, the processes of pyrolysis and growth of particles are accompanied by considerable thermal effects leading to an essential deviation of the current temperature of a mixture from initial "frozen" values. It is obvious that these deviations should increase with the growth of concentration of the reacting molecules. Nevertheless, the results shown in Fig. 34 demonstrate that the induction times obtained at a variation of the concentration by 1000 times are well generalized by dependences on "the frozen" temperature T_5 . At the same time, the delay of particle appearance in hydrogen free mixtures of C_3O_2 is shorter by almost two orders than in the hydrocarbon system. From this fact it follows that the long induction times observed in acetylene (and other hydrocarbons) (see Figs. 29–33) are caused by growth stages of poly-hydrocarbons that are transparent in the visible range of a spectrum, while in C_3O_2 the particle growth begins directly after decomposition of the initial molecules. To confirm this statement let us compare the rates of primary reaction of acetylene and carbon suboxide decomposition, which are assumed to be the rate limiting steps of the whole process [115,120]:



It is easy to evaluate that in the temperature range 1600–2000 K these rates only differ by factor 3–6. Thus induction times of the inception of condensed particles in acetylene are comparable with the characteristic time of reaction (28) $\sim (k_{C_2H_2} \cdot [C_2H_2])^{-1}$, while in carbon suboxide the particles already appear at a time that is approximately a factor of 100 shorter than the characteristic time of reaction (29). In other words, these estimations visually confirm that in carbon suboxide each act of decomposition of an initial molecule immediately leads to the formation of the condensed particles, while in acetylene these two processes are separated by a long stage of polymerization of the hydrocarbons.

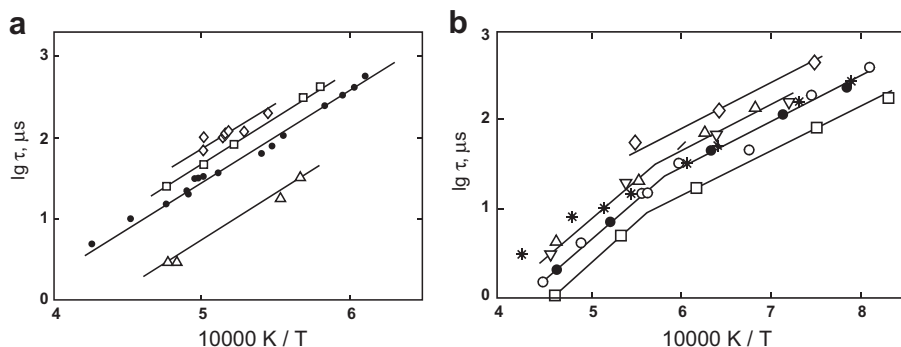


Fig. 33. Induction times of carbon particle formation measured at different concentration of carbon bearing molecules in C_6H_6 ($[C] = 0.4$ (\diamond), 1.0 (\square), 4.0 (\bullet) and 40 mol/m³ (Δ)) - (a) Ref. [118] and C_3O_2 ($[C] = 0.1$ (\diamond), 0.3 (Δ), 1.0 (\bullet) and 3.0 mol/m³ (\square)) - (b) Ref. [20]. Lines – best fit of experimental data.

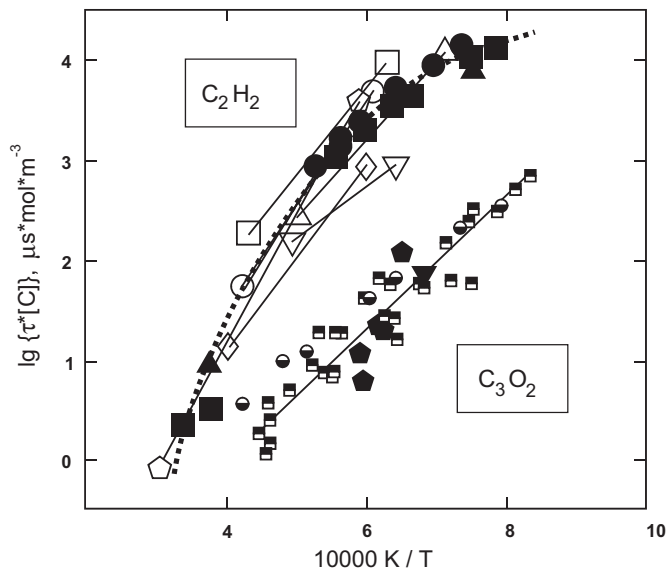


Fig. 34. Induction times of extinction increase in the rich mixtures: ● - 10% C₃O₂ + Ar; ■ - 20% C₃O₂ + Ar; × - 20% C₃O₂ + 10% H₂ + Ar; ● - 20% C₂H₂ + Ar, P = 5.5–6.4 bar; ▴ - 20% C₂H₂ + Ar, P = 7.9–14 bar; ▲ - 20% C₂H₂ + Ar, P = 29.9–30.4 bar (all data from [106]), in comparison with data from previous studies on highly diluted mixtures: – - 10% C₂H₂, [115]; □ - 5% C₂H₂, [118]; ○ - (0.2–1%) C₂H₂, [22]; △ - 2% C₂H₂, 10–12 bar, [22]; ▽ - 2% C₂H₂, 1–2 bar, [22]; ◇ - (1–20%) C₂H₂, [26]; ■ - (0.3–1%) C₃O₂, [20]; ● - (0.33% C₃O₂ + 0.33% H₂), [20]. Curved dotted line – approximation of the data [106].

4.2. Rate constant of particle formation k_f

The stage of the process following the induction time is characterized by the rapid growth of extinction and thus reflects a sharp increase in the volume fraction of the condensed particles f_v . It was already noted above that extinction measurements do not allow for determining with what effect the increase of f_v is connected, i.e. with an increase in the number of particles, their sizes or with the change of their refractive index. To solve this problem, it is necessary to perform independent measurements of particle sizes, as has been done by the scattering method in [37,39,48–52] or LII [36,38,72–75]. Nevertheless, measurements of f_v increase present the important phenomenological characteristic of the process of nanoparticle formation, which is quite valuable for elaborating the kinetic mechanisms of particle growth.

As was stated in [6,121], soot growth could proceed by two different ways: by coagulation, whereby two particles collide and fuse to form one larger particle, or by surface growth in which gas-phase hydrocarbon species or carbon atoms and small carbon clusters directly become attached to and incorporated into the existing particles. It is clear that coagulation leads to a reduction in particle number density while the volume fraction remains unchanged. On the other hand, surface growth does not alter the particle number but does lead to an increase in particle size and volume fraction. Haynes and Wagner [121] have shown that the process of surface growth of particles could be described by equations of the relaxation type:

$$\frac{df_v}{dt} = k_f \cdot (f_v^\infty - f_v) \quad (30)$$

where f_v^∞ is the final observed value of f_v . This equation determines one more quantitative kinetic parameter of the process, an effective rate constant of particle growth k_f . Later, in studies [31,48], such approach was applied to the analysis of the profile of f_v extracted from the measurements of extinction profiles in investigations of carbon particle formation in shock wave pyrolysis experiments. In

Fig. 3, one can see an example of such a treatment of the time profile of particle volume fraction. Now, such method for the analysis of the kinetics of particle growth is commonly accepted (see for example [33,34,41,42,51]).

Data from the majority of studies testifies that the growth rate of the volume fraction of the condensed phase sharply increases in the temperature range up to 2000–2200 K and, as well as the induction time of particle inception, is well-described by Arrhenius-like temperature dependences. A slope of these dependences allows for determining the activation energy of the process of particle growth, which for different substances varies in the range from 150 to 220 kJ/mol [20,31,33,42,44,106,116,118].

In Figs. 35–37, examples of experimental data on the effective rate constant of particle formation during the pyrolysis of various carbon precursors are given. Attention has to be drawn to the fact that the lowest particle growth rates are observed in saturated (methane, hexane) and unsaturated (acetylene, ethylene) linear (aliphatic) hydrocarbons, while particles grow noticeably faster in aromatic precursors (benzene, phenyl-acetylene) [31,33,118] and the fastest growth of particles takes place in hydrogen-free mixtures (C₃O₂, CCl₄) [20,41]. These data represent important information for understanding the role of hydrocarbons of various structures in the growth mechanisms of carbon nanoparticles.

Special questions cause the break of the Arrhenius-like dependence of the particle growth rate, observed in the majority of hydrocarbons at temperatures above 2000 K [31,33,48,118] (see Figs. 36 and 37). Certainly, when approaching the evaporation temperature of carbon, a process of particle fragmentation should be observed. Such a process was investigated in [122] at temperatures above 3500 K. The influence of this reversal process with temperature rise should necessarily lead to a gradual delay of the particle growth rate and even to its decrease. However, at temperatures close to 2000 K, which are rather far from the temperature of phase transition in carbon, it is unlikely that a sharp break in the temperature dependence of particle growth rate would be associated with the beginning of particle fragmentation.

Therefore, a clear physical interpretation of this phenomenon has not yet been suggested. In some studies [24,31,33,51], the interrelation of the behavior of particle growth rate with a temperature dependence on the induction time and particle yield is discussed, and in [42,44], the dependence of k_f on the wavelength of the extinction profile measurements was analyzed. According to the conclusions of these works, as well as a later study [106], such a strange decrease in the particle growth rate at high temperatures

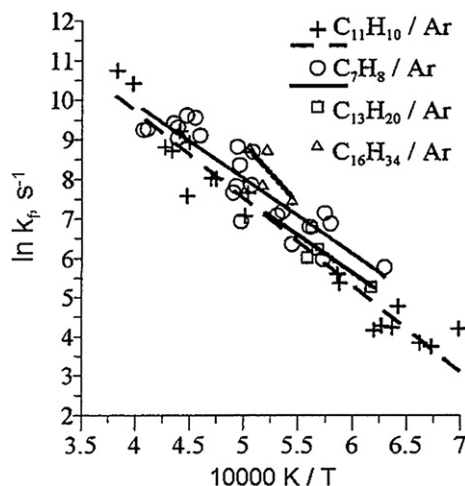


Fig. 35. Influence of temperature and nature of the hydrocarbon on the soot growth constant. Ref. [116].

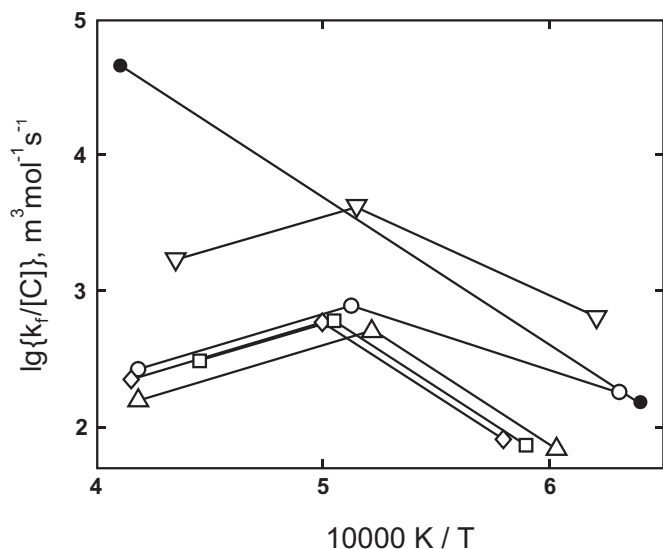


Fig. 36. Temperature dependence of the normalized first-order rate constant ($k_f/[C]$) for benzene (●), phenyl-acetylene (▼), acetylene (○), ethylene (△), methane (◇) and n-hexane (□). Ref. [118].

is most likely caused by the peculiarities of measurements in shock tubes and actually reflects only secondary processes of coagulation of small (transparent) carbon particles. In more detail, these processes will be described below in Section 7.2 which is devoted to the temperature dependence of the processes of carbon nanoparticle formation behind shock waves.

One more important reason of a divergence in the data for k_f , measured under various conditions, consists of neglecting the thermal effects of pyrolysis and the subsequent particle growth. The problem is that, in the majority of investigations, the obtained data is related to the initial “frozen” temperature behind the shock wave, which does not account for its change in the course of the chemical reaction. The amendments arising because of temperature drop in the course of the endothermic reactions of pyrolysis and heat release during particle formation were considered for the first time in [57] and have allowed for overcoming these divergences. Later, based on these corrections, the more general dependence of particle growth rate, describing various conditions

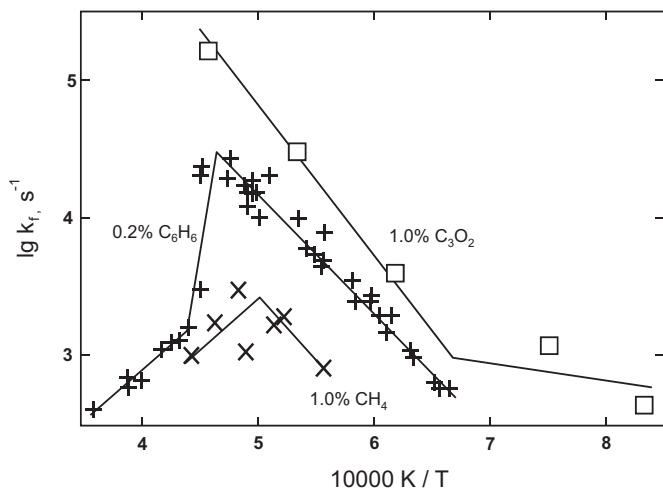


Fig. 37. Soot growth rate in carbon suboxide pyrolysis compared with those of methane and benzene at similar carbon concentrations. Ref. [20].

of pyrolysis, has been proposed [42,44]. In more detail, these effects are considered below in Section 7.

4.3. Kinetics of particle size growth

The rate constant of particle volume fraction growth, determined from extinction measurements, gives only an indirect representation of the kinetics of condensation. To get direct data on particle growth, measurements from the time profiles of the particle sizes are necessary. It has been shown above that such measurements are possible using scattering methods (Section 3.2) and laser-induced incandescence (LII) (Section 3.5). Examples of such measurements are demonstrated in Figs. 20 and 21. Unfortunately, such measurements are quite labor-intensive and consequently are few in number. Due to this, quantitative data on the rate constants of particle size growth are absent in the literature. Nevertheless, simultaneous measurements of the sizes and volume fraction of the particles performed in [36,48–51] provide the opportunity to trace not only the process of particle size increase by surface growth, but also to extract the time profile of their number density reflecting the process of coagulation. The first attempts to determine the partial contributions of these two processes by means of simultaneous scattering and extinction measurements have been made by Graham [23,39,47]. Further, a similar analysis of the role of the process of coagulation has been performed by Kellerer et al. [50,51]. In Fig. 38, estimations of the change in the rate of particle surface growth during the pyrolysis and oxidation of n-heptane at various temperatures are shown. It can be seen that at temperatures above 1600 K, the rate of particle surface growth sharply decreases at beyond 1 ms and, thus, the further growth of particles proceeds mainly by coagulation processes.

This conclusion has been confirmed by measurements performed in a recent study [123]. Joint consideration of time profiles of particle size D , measured by LII, and particle volume fraction f_v measured by extinction, allowed the authors to construct the profiles of particle number density N_p , specifying a more sharp decrease of N_p and an acceleration in particle size growth beyond 1 ms. Based on these results, the authors suggested dividing the whole process into three stages (see Fig. 39) I - C_2H_2 thermal decomposition and nucleation (0–250 μs), II - particle surface growth (250–1100 μs) and III - particle coagulation (beyond 1100 μs).

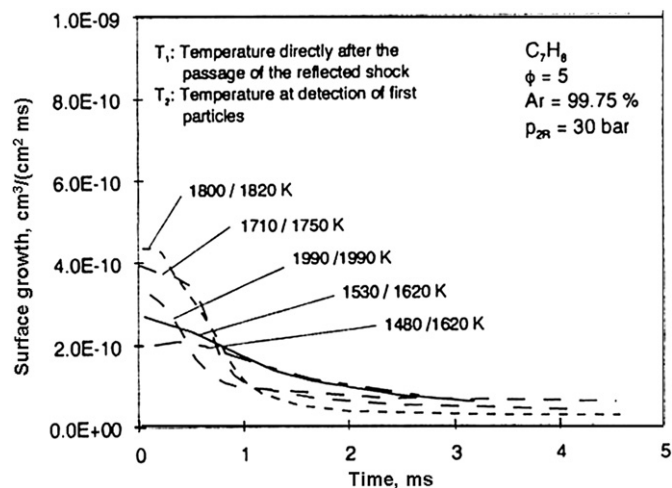


Fig. 38. Estimated rates of particle surface growth during pyrolysis and oxidation of n-heptane at different temperatures. Ref. [50].

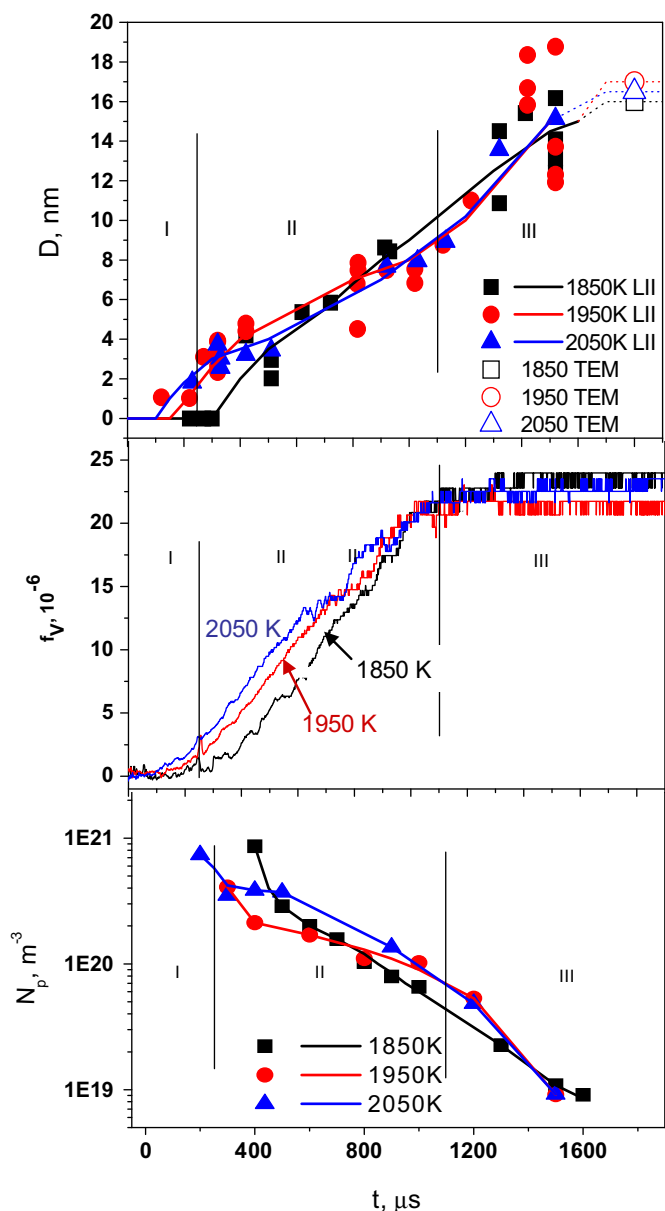


Fig. 39. Simultaneous measurements of particle size D (by LII), volume fraction f_v (by extinction) and values of particle number density N_p , calculated from them. Vertical lines show the conventional separation of three stages of the process: I – decomposition of C_2H_2 and nucleation; II – particle surface growth; III – coagulation. Ref. [123].

It is obvious that such a rather qualitative interpretation of the obtained data requires further analysis of the processes taking place, based both on a more extensive volume of experimental data and on detailed modeling calculations.

5. Size and structure of formed carbon particles

The sizes, chemical content, structure and other properties of the soot formed in combustion processes have been investigated quite comprehensively. However, shock wave pyrolysis presents considerably wider opportunities for the variation of key parameters of the process. First of all, it has a wide temperature range (from the lower border of pyrolysis at 1200–1400 K up to the disintegration of particles at 3000–3500 K). Besides that, in addition to the easy variation of pressure (from ~ 1 bar–100 bar) and concentration (from ~ 100 ppm to ~ 10 –30%), carbon sources

including not only flammable hydrocarbons but practically any volatile carbon-containing species can be used. Therefore, questions on the properties of the carbon particles formed in shock wave pyrolysis processes are of special interest.

Since the process of condensed particle formation in shock waves lasts about 1–3 ms, a sampling of particles at different stages of the process (as is possible in flames) is almost unfeasible, and for an analysis of the current properties of formed particles, only in situ diagnostics can be used. It was shown above that different methods can be used to measure the time profiles of particle size and their optical properties. However, detailed analysis can be performed only for particles deposited on the shock tube walls or substrates after the experiment, using the methods described in Section 3.7.

It has already been noted above that the size of the particles formed during the pyrolysis of hydrocarbons in the temperature range close to flame temperatures (1600–1800 K) is rather similar to the typical size of soot particles formed in flames (15–25 nm). The structure of particles in this temperature range represents amorphous graphite. At lower and higher temperatures, and also with a decrease in the concentration of the precursor, particle size decreases slightly (see [36,48,72,93] and Figs. 9, 20 and 22–24). At temperatures up to 2500 K, together with a decrease in particle size, an insignificant crystallization of particles is observed. The elemental analysis of these particles confirms that they completely consist of carbon, and the hydrogen content in these particles is below the limit of sensitivity of the measurement ($H/C < 0.03$) [36,106].

Many more diverse particles during the pyrolysis of hydrogen-free species have been observed. In the first studies investigating carbon particle formation during the pyrolysis of carbon-chlorides [40,41], white or light-lemon particles were found out on the tube walls, and the assumption was expressed [40] that they were composed of chaoite, a modification of the one-dimensional carbon crystal carbyne. However, later experiments [36] did not confirm this assumption. In more detail, the question of obtaining carbyne nanoparticles during the pyrolysis of carbon suboxides was discussed in [34]. In this work, a large diversity of particle sizes and structures were formed in a wide temperature range from 1500 K to 3500 K. In Fig. 40, TEM exposure of the particles formed at different temperatures of C_3O_2 pyrolysis are shown. One can see that particles formed from C_3O_2 at usual flame temperatures 1500–2000 K look similar to normal soot from hydrocarbons (e.g. C_2H_2): spheres 10–30 nm in size. At temperatures from 2100 to 2600 K, two different kind of particles were found: large balls with a nearly spherical structure and gigantic film-like spheres with a size up to 700 nm, which could be formed due to the rapid agglomeration of small “liquid clusters” during cooling after the shock. The peculiarity of the high temperature (2700–3200 K) process of carbon particle formation during C_3O_2 pyrolysis was the high degree of crystallization of the final particles. The particle size was again in the range of 20–30 nm. The structure of the observed crystals was hexagonal layers with lattice spacing similar to that of graphite. For $T > 2000$ K, crystallization of particles was high enough to perform MDF studies. In Fig. 41, an example of the ring structure pattern is given. The image shows the clearly developed ring structures of the d_{002} , the d_{100} and the d_{110} reflexes [124,125]. In Table 2, the results of these MDF measurements are given in comparison with those of graphite [126], carbyne [127] and the test mixture, carbon black [124]. One can see that in none of these cases were carbyne crystals found. This fact was explained in [34] by the strong dependence of carbyne conservation on the cooling rate [128]. Evidently, in shock tube experiments, the cooling process proceeds in rarefaction waves and by diffusion processes in the boundary layer, and therefore it is not too fast. Due to this reason and due to the very short time of condensed particle growth, shock tube experiments

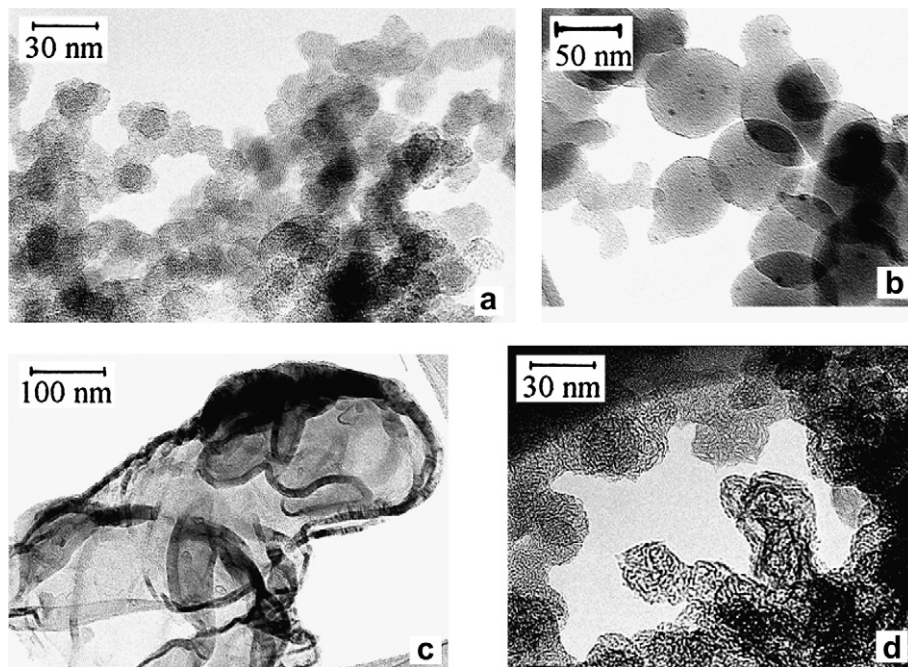


Fig. 40. High resolution transition electron microscope (HRTEM) images of carbon particles, formed during C_3O_2 pyrolysis at different temperatures: a) $T = 1646$ K, $P = 26.2$ bar b) and c) $T = 2214$ K; $P = 24.4$ bar; d) $T = 3002$ K, $P = 46.4$ bar. Ref. [34].

are probably not very promising for the investigation of such specific carbon nanoparticles as fullerenes and nanotubes.

6. Thermal effects and ionization of particles forming in pyrolysis processes behind shock waves

6.1. Endothermic effects of pyrolysis reactions

One of the basic advantages of experiments in shock tubes is the possibility of reliable control of parameters of the mixture during

an experiment. As noted above (see Section 2), due to the one-dimensional flow in a shock tube, the temperature and pressure behind the shock wave can be quite precisely determined from measurements of shock wave velocity. Certainly, such calculations are based on knowledge of the thermodynamic parameters of the mixture under given conditions. Therefore, to avoid uncertainties caused by the chemical transformations behind shock wave, the majority of researchers tend to work on mixtures highly diluted with inert gas. Such an experiment allows for neglecting the thermal effects of chemical reactions and the change in total heat capacity and density of a mixture during reactions.

Most investigations on carbon particle formation in shock waves have been carried out using such an approach. The concentration of the reacting species is, as a rule, no more than 1–3%. In the majority of such studies the “frozen” temperature behind a shock wave, not considering the effects of chemical reactions, was determined by measurements of shock wave velocity. In Fig. 17a (Section 3.4), an example of a measurement of the temperature time profile of in a non-reacting mixture is shown. One can see that the measured temperature with good accuracy coincides with the calculated values determined from the measured velocity of a shock wave.

All obtained results on particle formation were referred to these temperature values. Attention was drawn to possible errors of such assumptions for the first time [57]. In this work, heat consumption during the pyrolysis of initial hydrocarbons (ethylene, n-hexane) and the subsequent heat release during the growth of particles were considered. The authors predicted possible overheating of particles at an initial stage of their growth owing to the intensive energy release in condensation reactions.

In more detail, questions on the influence of endothermic pyrolysis of the initial species on the decrease in the real temperature of a mixture is considered in [41,42,44,67], and the temperature increase, caused by the heat release of condensation in [67,129]. Direct experimental observation of non-equilibrium excitation of small carbon C_2 clusters during the pyrolysis of C_3O_2 is reported in [130,131], and attempts to observe an overheating (or

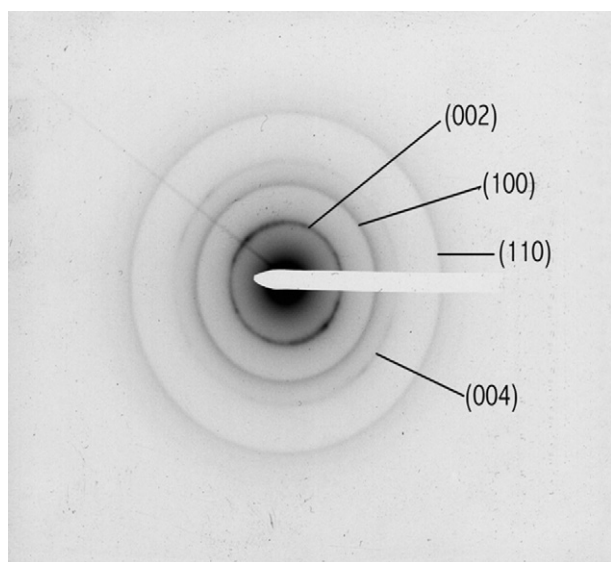


Fig. 41. Micro-diffraction (MDF) image of carbon particles obtained during C_3O_2 pyrolysis at $T = 2214$ K, $P = 24.4$ bar. The lines together with the numbers in brackets characterize the position and the main lattice spacing d_{hkl} of the studied particles. The ring pattern is made up of contiguous circles which results in a finer grain size. Ref. [34].

Table 2

Results of MDF measurements for various carbon particles formed at shock wave pyrolysis of C_3O_2 at different temperatures. (1) - Results from spherical particles. (2) - Results from gigantic large particles. Ref. [34].

Substance	T [K]	d_{002} [Å]	d_{100} [Å]	d_{110} [Å]	d_{100}/d_{110}
Graphite [98]	300	3.3756	2.1386	1.234	1.733
Carbyne [100]	300	2.204	4.408	2.545	1.732
Carbon Black (Test subst.) [97]	300	3.42	2.09	1.21	1.73
C_3O_2	2214	3.40	2.07	1.20	1.73
(1) C_3O_2	3002	2.96	2.03	1.19	1.71
(2) C_3O_2 OOOO	3002	3.27	1.99	1.17	1.70

cooling) of larger particles relative to the surrounding gas are presented in [58,132].

All these works have shown that the use of an isothermal approach for the analysis of experimental data on carbon particle formation in pyrolysis processes is not always justified, even at concentrations of the reacting substances less than 1%. In the majority of systems, the most essential endothermic effects of the pyrolysis of the initial species appear. In practice, the problem of exactly calculating the temperature drop of a mixture in a pyrolysis reaction becomes complicated due to simultaneous secondary reactions of polyatomic hydrocarbons or direct carbon particle growth with poorly known thermodynamic properties and, hence, uncertain thermal effects.

One of brightest examples of this considerable temperature drop is seen in the pyrolysis of CCl_4 . Endothermic decomposition



is 585 kJ/mol, therefore even in the mixtures containing 1% CCl_4 in argon, the temperature drop during pyrolysis can reach 300 K [41,42,67]. Indeed, reaction (31) does not proceed directly, and actually the pyrolysis of CCl_4 occurs by a consecutive abstraction of chlorine atoms [40,41]. Additionally, initial carbon appears in a mixture not in the form of C atoms, but basically as clusters of C_2 [67]. Therefore, the real temperature drop is slightly less than this limiting estimation. Nevertheless, the total thermal balance of CCl_4 pyrolysis and subsequent particle growth is essentially negative. The measurement of the current temperature in mixtures containing 1.5% and 3% CCl_4 in argon have been carried out in [42,67] by means of a two-channel emission-absorption line-reversal method in the IR spectrum range [14,63,133]. To increase the sensitivity of the measurements at early stages of the process before formation of the condensed particles in the mixture 5% CO_2 (which is rather inert below 2500 K) was added and measurements were performed in the intensive band of CO_2 at 2.7 μm . The details of such temperature measurements have been described above (see Section 3.4). In Fig. 42, examples of IR emission-absorption and laser extinction measurements and extracted temperature profiles are shown. Since decomposition of CCl_4 proceeds very quickly, over several microseconds, the stage of temperature drop could not be resolved; therefore, only the final, established temperature values were measured. Note that the beginning of particle formation was reflected by the increase in all signals in this case but had no noticeable influence on the current temperature.

In Fig. 43, a dependence of measured (established) T_{exp} and calculated “frozen” T_5 temperatures behind the reflected shock wave on the velocity of an incident shock wave is shown. One can see that it is linear and the angle of the slope of the measured temperature plot is essentially less than the angle of the slope of the calculated temperature. This fact testifies to the increase in the difference between the calculated and measured temperatures with increased velocity of the initial shock wave. The analysis of

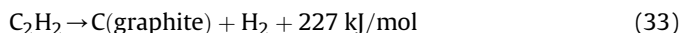
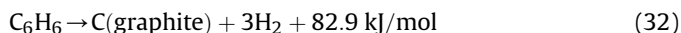
these results was performed in [67], which concluded that the main reason for this effect was the increase in the degree of decomposition of CCl_4 and its fragments with the temperature increase.

Experimental temperature profiles in benzene have a much more complex shape (see Fig. 44). Benzene decomposition proceeds more slowly and it is possible to observe the final stage of temperature drop after passage of the shock wave front. Additionally, with the increase of initial temperature T_5 , the secondary growth of temperature, which is most likely caused by the exothermic reaction of particle formation, becomes more and more noticeable. Nevertheless, the final value of temperature in this mixture also lies essentially below the initial values (see Fig. 45) and the depth of cooling of the mixture increases with increased initial temperature of pyrolysis. Similar to CCl_4 , this effect is caused by the increase in the degree of decomposition of C_6H_6 and its fragments. The nonlinear dependence of temperature drop on the concentration of C_6H_6 in a mixture is notable. One can see from Fig. 45 that with a four-fold increase in the C_6H_6 concentration, the temperature drop increases only two-fold (at $T_5 = 2000$ K). This effect is explained in [67] by the increased contribution of exothermic reactions of hydrocarbon formation from benzene fragments with the increased C_6H_6 concentration in the mixture.

Similar effects on the temperature drop of a mixture were observed in ethylene and n-hexane [57,58].

6.2. Heat effects of particle formation

The effects of temperature variation in pyrolysis processes of carbon-bearing mixtures, considered above, were basically determined by the essential endothermic decomposition of the initial species. However, the reverse situation, when the total heat balance of the mixture as a result of pyrolysis and particle formation processes appears to be positive, is also known. In this case, the final temperature exceeds the initial “frozen” values. In Fig. 46, the data of temperature measurements [58] in benzene, n-hexane and acetylene in comparison with the frozen temperatures behind shock waves are shown. These measurements, unlike those in [67], were performed by the registration of emission in the spectrum range from 0.63 μm up to 4.26 μm with the assumption of an invariable extinction coefficient of soot. The data from these measurements show that benzene pyrolysis, as well as acetylene pyrolysis, has a positive heat balance. From the point of view of the limiting thermodynamics of these processes (at 298 K)



Ref. [134] such an effect is quite justified, although the actual heat release is determined by the real magnitude of the volume fraction of the condensed phase f_V at a given stage of the process. From this point of view, a disagreement in the data from [67] and [58] can be explained by the higher pressures in [58] that allowed for observing the later stages of the condensation process, corresponding to a larger yield of condensed particles during the observation time.

An even more essential temperature increase, caused by the release of energy from the condensation of carbon nanoparticles, was observed during the pyrolysis of carbon suboxide [129]. The molecule of carbon suboxide in the ground state represents a linear structure where central carbon atom is bound to two CO ligands ($OC \equiv C \equiv CO$). Therefore, the thermal decomposition of carbon suboxide proceeds by consequent detachment of these ligands:

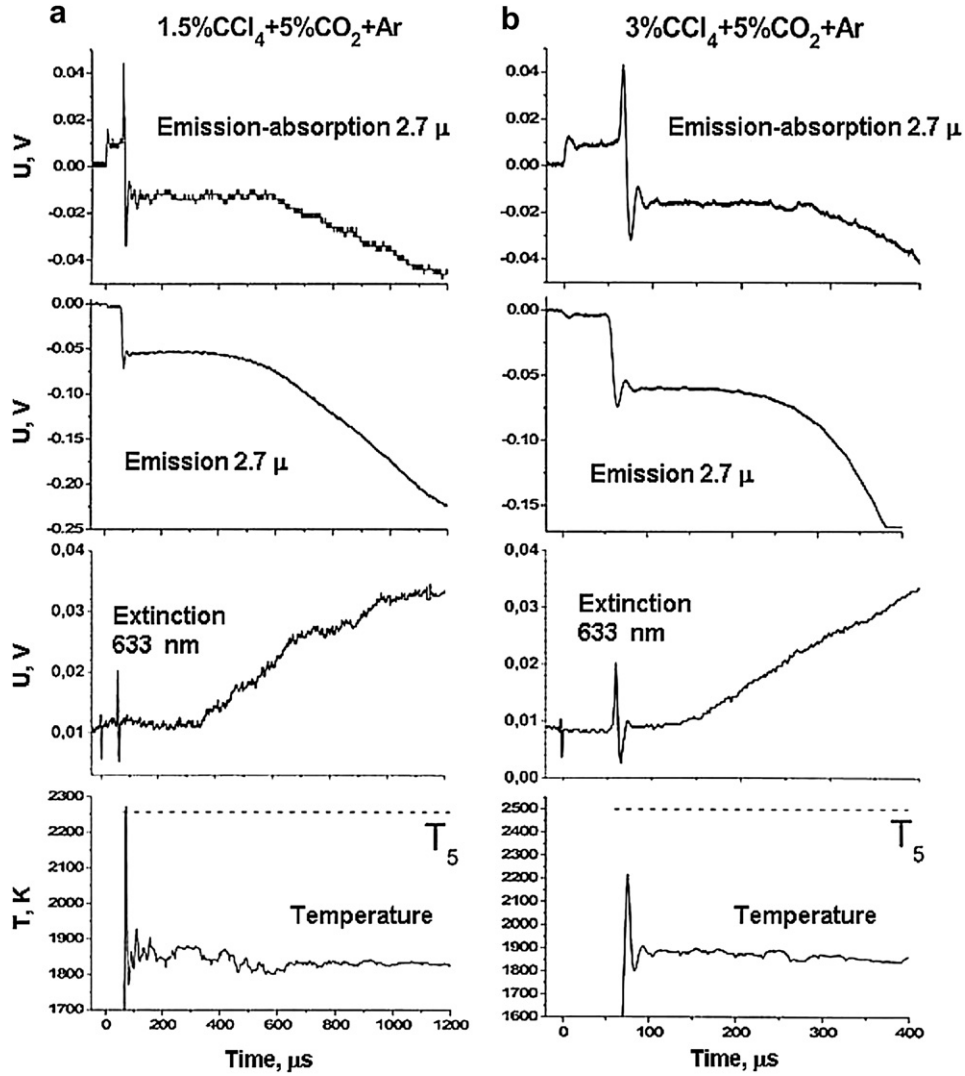


Fig. 42. Absorption, emission and laser extinction signals and extracted temperature profiles in the mixtures: a) 1.5% CCl₄ + 5% CO₂ + Ar at $T_5 = 2256$ K, $P_5 = 3.2$ bar; b) 3% CCl₄ + 5% CO₂ + Ar at $T_5 = 2498$ K, $P_5 = 3.1$ bar. Ref. [67].

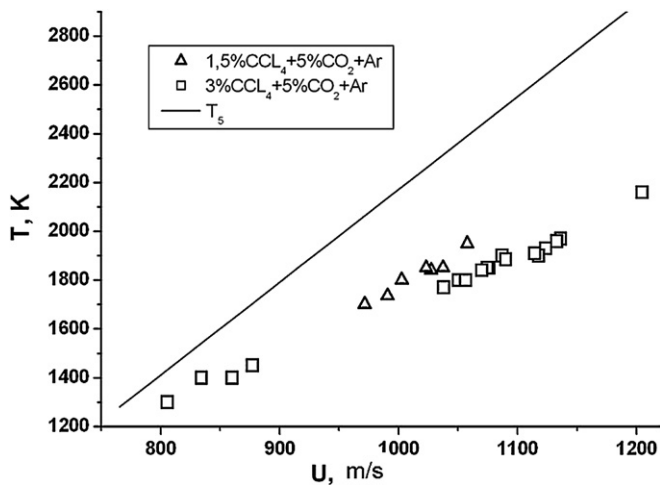
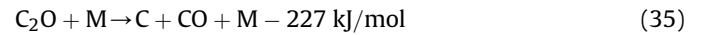
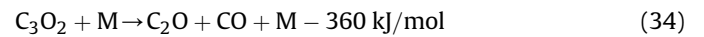
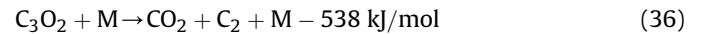


Fig. 43. Calculated ("frozen") temperature behind the reflected shock wave T_5 and experimentally measured temperatures at a later stage of the pyrolysis process in the mixtures 1.5% CCl₄ + 5% CO₂ + Ar and 3% CCl₄ + 5% CO₂ + Ar depending on the velocity of the incident shock wave U . Ref. [67].

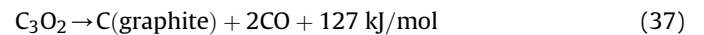


while the channel of CO₂ formation



is quite improbable [120].

The total heat effect of condensed carbon formation in this process is noticeably less than in the pyrolysis of acetylene [33]:



However, the rate of particle growth in this case is essentially higher; therefore, the whole process is completed depending on temperature and pressure over several hundreds of microseconds or less.

In the experiments in [129], in which temperature measurements similar to those described above in Section 3.4 were performed, the temperature increase was directly observed simultaneously with the increase in extinction signals, characterizing an increase in the volume fraction of the condensed phase. In

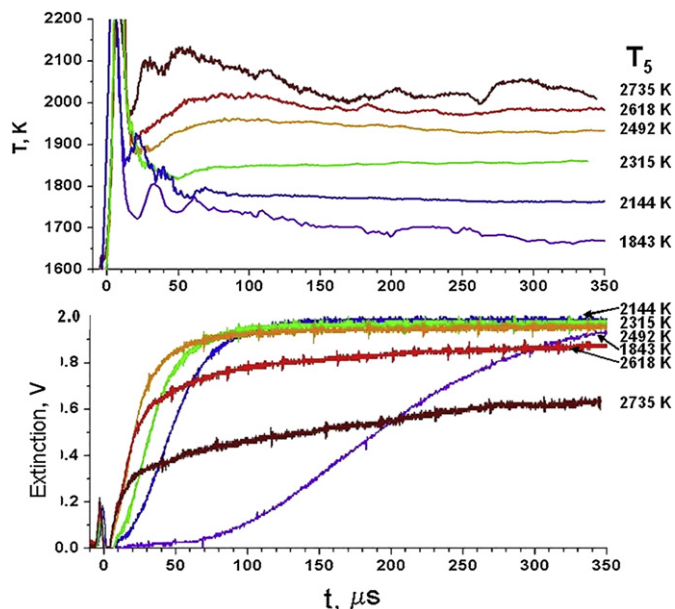


Fig. 44. Temperature and extinction profiles measured in the mixture 2% C_6H_6 + 5% CO_2 + Ar at the initial ("frozen") temperatures $T_5 = 1840$ – 2740 K and pressures $P_5 = 2.8$ – 3.5 bar. Ref. [67].

Fig. 17b the example of the time profiles of extinction and temperatures during the pyrolysis of 3% C_3O_2 + 5% CO_2 + Ar is shown. The initial temperature behind the reflected shock wave was 1730 K, and after the completion of particle growth, it was 1900 K. With an increase in the initial temperature, the total heat release of the reaction also increased, such that at an initial temperature of 2200 K its increase $\Delta T = T_{exp} - T_5$ reached 300 K (see Fig. 47).

The authors of [129] connected this effect to a decrease in the final size of the formed particles during the temperature increase. This has allowed for determining that the heat release of a single-atom-to-particle condensation decreases from ~ 200 kJ/mol for particles containing ~ 1000 atoms to ~ 50 kJ/mol for particles containing $\sim 10^6$ atoms.

It is worth adding that, based on these results, in recent experiments [135] the new physical phenomenon of a detonation

wave of condensation was observed for the first time. In this case, the authors used richer mixtures containing 10–30% C_3O_2 in argon and heating the mixture to about 1000 K. As a result of this energy release, the shock wave was accelerated and transformed into a detonation wave.

Another interesting example of the release of the energy of condensation in the same mixtures at the earliest stages of the pyrolysis process was observed in [130,131]. In this case, the small carbon C_2 clusters were formed mainly in electronically-excited states, and authors succeeded in observing not only non-equilibrium excitation of the Swan bands of C_2 radicals, but even inversion of separate electronic-vibrational transitions.

The given examples show how essential thermal effects can be on pyrolysis processes in shock waves, even in rather diluted mixtures. It is important to underline that the absolute value of temperature deviation is dependent on the integral heat balance of pyrolysis of a given mixture; therefore, it is impossible to make any general recommendations about the maximum allowed concentration for the simplified isothermal approach. Due to this, any investigations of the temperature dependence of either parameters of the particle formation process should be based on knowledge of the real temperature of the mixture which can appear to be lower or higher than the initial "frozen" temperature determined by shock wave velocity measurements.

6.3. Formation of charged particles

Negatively and positively charged carbon particles are observed in premixed and diffusion flames [136–140] and in low temperature plasma [141]; however, the problem of charged carbon nanoparticles, formed in the pyrolysis processes behind the shock wave, is poorly studied. Among some early works, one can find only one short letter [142] about the ionization of soot behind shock waves.

In the 1980s, there was a controversy about the ionic or non-ionic mechanisms of soot formation in flames [137,143,144]. A detailed modeling of soot charging in flames performed recently [145,146] did not reveal the essential influence of charged particles on soot formation. Note, however, that these works analyzed chemi-ionization processes with the participation of large poly-aromatic hydrocarbons (PAH) only, while alkali metals as additional electron sources were not considered. On the other hand, it is known that, in the presence of typical atmospheric concentrations of alkali metals (10^{12} – 10^{13} cm^{-3} [147–150]), soot becomes charged even at temperatures of ~ 2000 K.

In a recent work [151], processes for charging carbon nanoparticles, formed during the pyrolysis of C_3O_2 in a shock tube, were investigated at various temperatures and concentrations. The selection of C_3O_2 as the carbon particle precursor was caused by the absence PAH that allowed for neglecting the processes of chemi-ionization and considering only thermo-ionization processes. Investigations were carried in a shock tube equipped with two high-sensitivity electric Langmuir probes. The diameter of each probe was 6 mm, and the electric voltage of the probes could be changed in the ± 80 V range. In Fig. 48, the scheme of the experimental set-up and the diagnostic equipment is shown.

Fig. 49 shows an example of the time profiles of laser extinction and signals from the positive and negative probes, measured in a mixture of 1% C_3O_2 in Ar at $T_5 = 2350$ K, $P_5 = 22$ bar. One can see from the extinction signal that the particles are formed rather quickly at times $t \sim 10$ μs and that they are stable during the entire measurement time. The rise-time of ion- and electron-probe signals show similar values of ~ 30 μs , and after a sharp maximum, both probes show a subsequent decrease which lasts for about 300 μs .

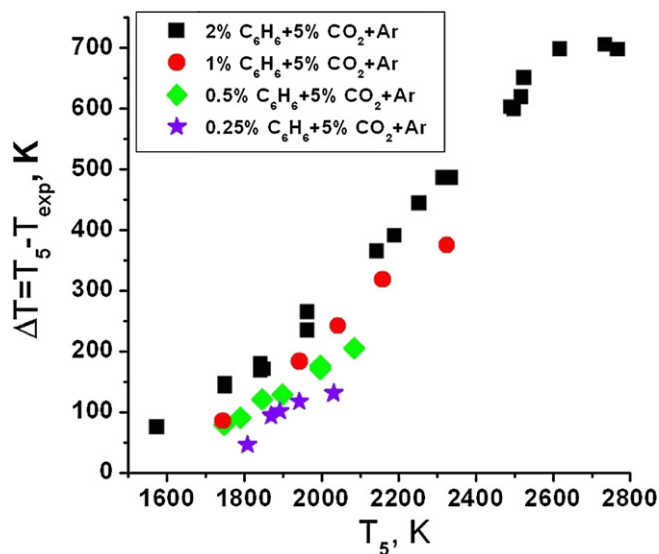


Fig. 45. Temperature decrease $\Delta T = T_5 - T_{exp}$ during the pyrolysis of benzene depending on the initial temperature behind the shock wave. Ref. [67].

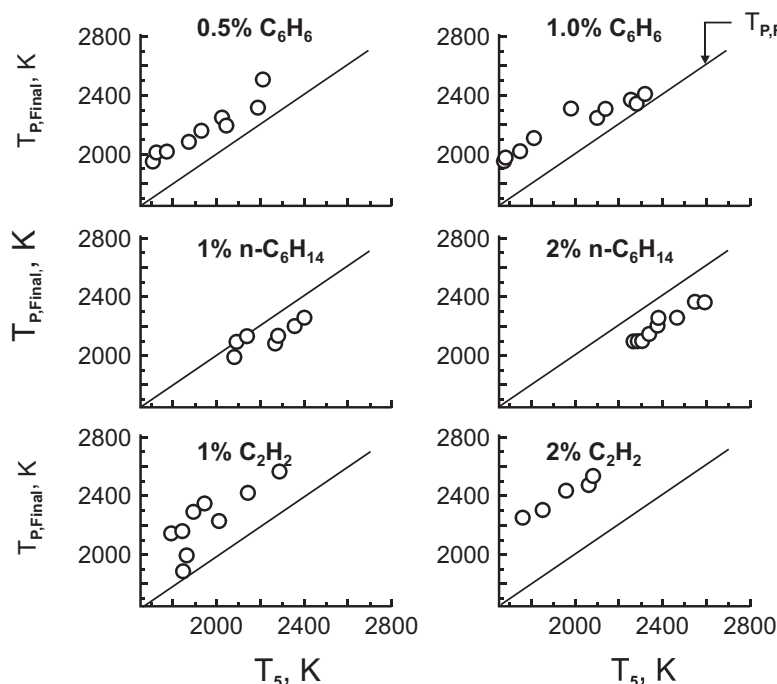


Fig. 46. Final values of measured temperature in comparison with the initial “frozen” temperatures behind shock waves during the pyrolysis of benzene, n-hexane and acetylene. Ref. [58].

The analysis of the obtained data has allowed authors to conclude that the processes of carbon particle charging under the given conditions are not caused by thermo-electronic emission of particles, and are the result of sticking of free electrons, formed by the ionization of a natural impurity of sodium which is always present in any gas. In Fig. 50, the measured values of the final electron concentration in a mixture with particles are shown. For comparison, the equilibrium electron concentration in the absence of the particles, caused by sodium ionization, is demonstrated. Thus, the authors [151] showed that the process of sticking of free electrons to carbon particles leads to the majority of particles acquiring a negative charge; the equilibrium concentration of free electrons in the mixture with particles is much less than in the same gas without particles; and the decrease in the electron concentration N_e is proportional to the square of the concentration of particles.

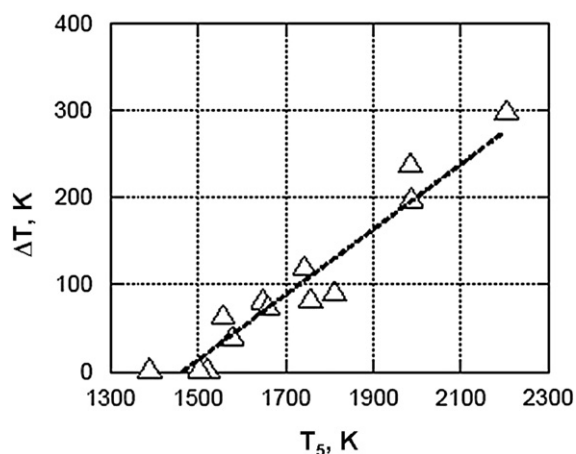


Fig. 47. Final temperature increase $\Delta T = T_{\text{exp}} - T_s$ during the pyrolysis of 3% $\text{C}_3\text{O}_2 + 5\%$ $\text{CO}_2 + \text{Ar}$ depending on the initial temperature behind the shock wave. Ref. [129].

Based on the analysis of experimental data, the authors [151] have suggested a simplified description of the kinetics of the governing processes. At early times $t \sim 10 \mu\text{s}$, a fast capture of electrons by the particles causes the additional ionization of sodium which results in an increase in the positive ion concentration. Later, the

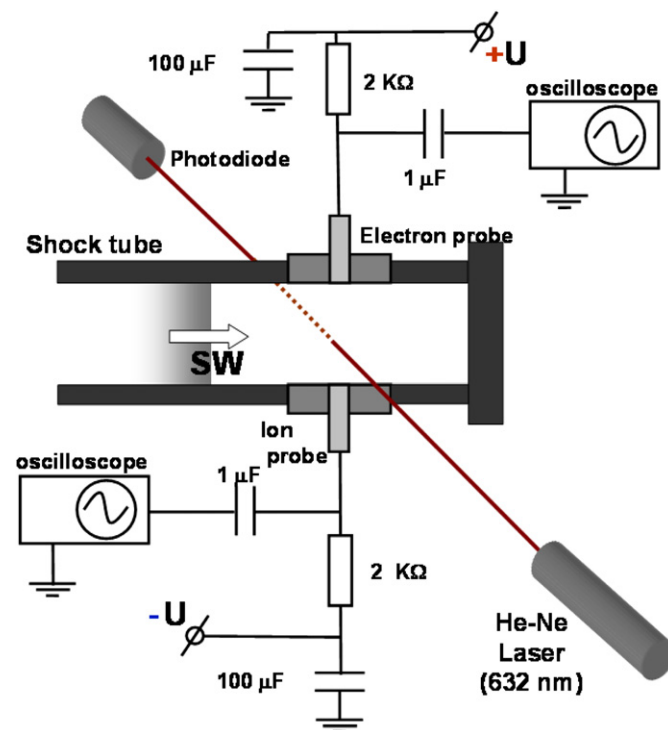


Fig. 48. Scheme of shock tube equipped with two high-sensitivity electric Langmuir probes and the laser extinction technique for the investigation of carbon particle charging. Ref. [151].

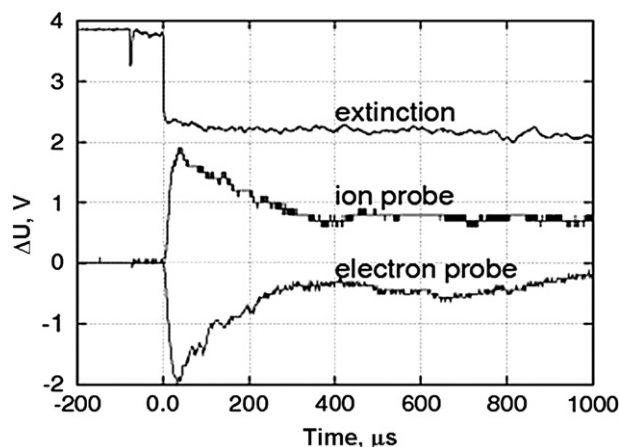


Fig. 49. Example of the time profile of laser extinction and signals from the positive and negative probes, measured in a mixture of 1% C_3O_2 in Ar at $T_5 = 2350$ K, $P_5 = 22$ bar. Ref. [151].

ion flux toward the particle is the governing process with a rate that is determined by the ratio of the Debye length and the ion-drift velocity. The final concentration ratio of negatively-charged particles and free electrons is in most cases $\gg 1$. Therefore, the electrostatic properties of the investigated mixtures are determined by the charged particles only.

The authors [151] claim that such a result opens up new possibilities for controlling particle behavior in combustion systems by charging them by the addition of alkali metals.

7. Temperature dependences of the particle growth process

7.1. Particle yield and volume fraction

The temperature dependences of all the parameters of process of particle formation: final values of the volume fraction of the condensed phase, particle yield and their size, and also kinetic parameters: induction time and the rate constant of particle growth, are among the major characteristics of this process extracted from shock wave experiments. Perhaps the most remarkable characteristic of the process of carbon nanoparticle formation in pyrolysis and combustion processes is the so-called

“bell-shaped” temperature dependence of a soot yield. Such a shape for dependence, at first observed in flames [152], has been much more distinctly measured in a number of shock wave pyrolysis experiments ([20,25–28,31,33,35,37,41,48] and many others). Above, we mentioned that the position and width of observable “bells” essentially differs for various precursors, pressures and concentrations.

A discussion of the possible kinetic and thermodynamic mechanisms of the origin of the bell-shaped temperature dependence of soot yield and the reason of its distinction has been raised in [25,26]. The authors associated the formation of bell-shaped dependences with a competition between the reactions of growth and destruction of aromatic hydrocarbons, which were supposed to be the basic material for the formation of condensed carbon particles. Such a hypothesis allowed authors [25,26] not only to qualitatively explain the occurrence of bell-shaped temperature dependences of soot yield in various aromatic and aliphatic precursors, but also to explain their shift toward high temperatures with an increase in the concentration of reacting molecules. Therefore, authors [25,26] have claimed that by their estimations, the shift in the real temperature of a mixture because of the thermal effects of occurring reactions is insignificant and has no appreciable influence on the position of the curve, related to the initial temperature behind the shock wave. Thus, all phenomena of the appearance of bell-shaped curves and their behavior in various mixtures were attributed to the kinetics of formation and decay of various hydrocarbons.

Nevertheless, in later work by the same authors [40], and also in [20] and [41], similar temperature dependences were observed in hydrogen-free mixtures where the formation of carbon nanoparticles proceeds in the total absence of hydrocarbon species. Moreover, the maximum shift of bell-shaped dependences toward high temperatures was observed in carbon-chlorides with maximum endothermic decomposition [40,41]. In the previous Sections 6.1 and 6.2, devoted to temperature measurements in pyrolysis processes, it has been noted that the “isothermal” approach is not always justified for the analysis of the processes of pyrolysis and the growth of particles behind shock waves, even in strongly diluted mixtures.

How essential the knowledge of the real temperature is during the formation of carbon particles is shown in Fig. 51 [67] in which the temperature dependences of the final relative particle yield $Y_f = Y \times E(m)$ are compared in CCl_4 , C_2Cl_4 and C_6H_6 , related to the “frozen” temperature T_5 and to the real temperature, directly measured at a later stage of particle growth.

It can be clearly seen on the upper plots that all experimental dependences in different precursors and at different concentrations of the reacting molecules are essentially dispersed. The same data on the lower plots show bell-shaped curves, which are quite similar for all precursors as seen by the position of the maximum (around 1800 ± 50 K) and on the half-width of the dependence amounting to 350–400 K.

The demonstrated data allows us to draw a conclusion that the maximum particle yield is observed in each precursor approximately at the same real temperature T_{max} independently of the initial concentration of carbon-bearing molecules. Note that the values of T_{max} for various precursors are little different (see Table 3), which could be attributed to various exothermic character of secondary reactions. However, as a whole, these values are very close to each other (all of them are in the temperature range of 1600–1850 K) and they are close to the values T_{max} observed in combustion processes [152,153]. The given conclusion can be considered as evidence of the commonality of mechanisms of the formation of carbon particles in all processes of pyrolysis and combustion.

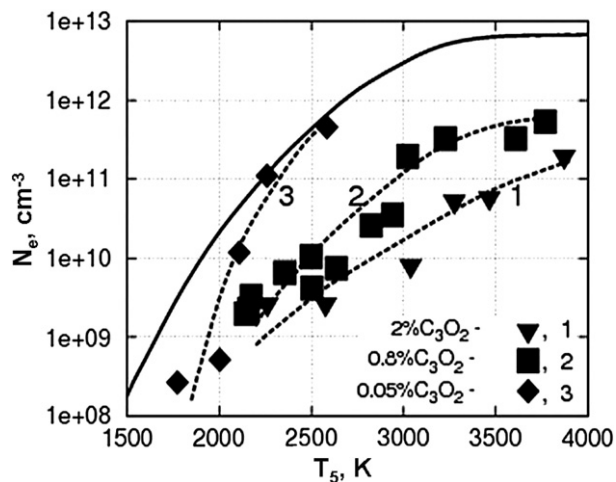


Fig. 50. Final electron concentrations $N_{e(eq)}$ measured at various particle concentrations. The solid line is the equilibrium electron concentration in argon with the natural admixture of sodium. Dashed lines – best fit of the experimental data Ref. [151].

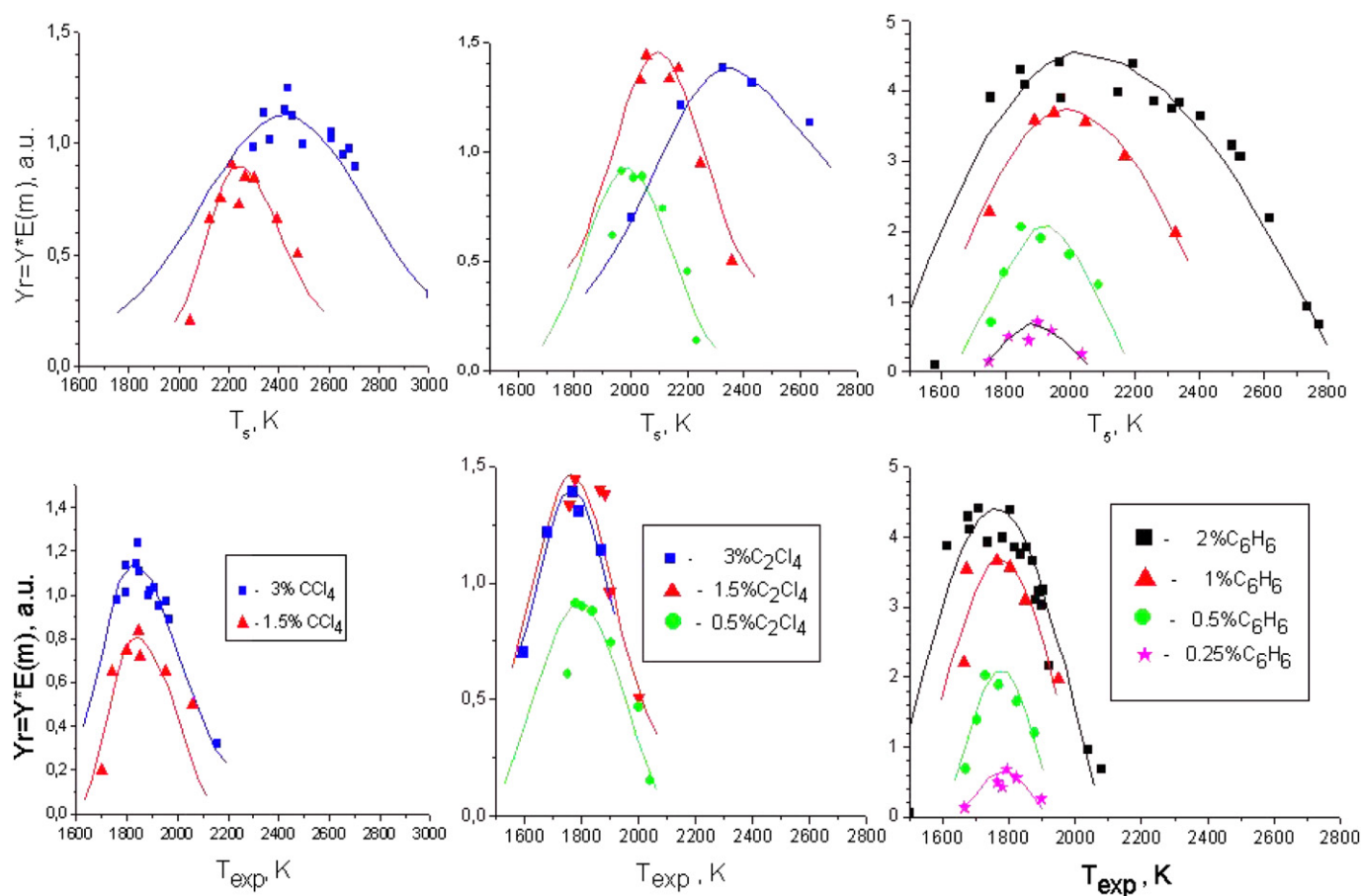


Fig. 51. Temperature dependencies of relative particle yield in various precursors, plotted versus initial (“frozen”) (upper plots) and experimentally measured temperatures (lower plots). Ref. [67].

The next important question, related to the correct understanding of the temperature dependence of the volume fraction or particle yield, is connected to accounting for the change in particle optical properties depending on their size. Unfortunately, in the literature, few studies on the change in the final size of particles with a variation in temperature during pyrolysis are available [36–38,48,51,72,93] (see Figs. 22–24). However, all available data specify that the shape of the temperature dependence of final particle sizes almost completely coincides with the dependence of the volume fraction or particle yield. This fact is not only surprising, but gives rise to suspicions. In fact, the ascending branch of the temperature dependence of particle yield, observed at temperatures between 1400 and 1700 K (see Fig. 51) can be reasonably explained by the increase in the degree of decomposition of the initial molecules and corresponding growth of the particles, but a decay in the yield of condensed particles at temperatures above 1800 K, observed in many hydrocarbons as well as in hydrogen-free mixtures, is difficult to explain. Generally, it is obvious that the thermodynamic stability of any gaseous carbon-bearing molecule decreases with an increase in temperature, and all carbon up to temperatures at which the decomposition (evaporation) of carbon nanoparticles becomes noticeable ($T \geq 3000\text{--}3500\text{ K}$ [122,154–156]) should be in the condensed state. Therefore, an observable decrease in the volume fraction or particle yield can be interpreted only as a decrease in the fraction of particles registered by extinction [25,26], or as a decrease in the coefficient of extinction of particles with increased temperature. Recent measurements of the size dependence of the coefficient of extinction of carbon particles [45] (see Fig. 10) in a combination with data on the

decrease in particle size with increased temperature (Figs. 22–24) indicate that an observable decrease in particle yield at $T > 1800\text{ K}$, measured by extinction with a He–Ne laser, can be completely attributed to a decrease in the particle refractive index function $E(m)$ with a decrease in particle size.

Interesting observations confirming this conclusion were made in [42]. The authors measured the temperature dependence of the final optical density in a mixture of $0.2\% \text{ C}_3\text{O}_2 + \text{Ar}$ at various wavelengths from $0.22\text{ }\mu\text{m}$ to $1.3\text{ }\mu\text{m}$. Unlike many hydrocarbons, during the pyrolysis of C_3O_2 , no gaseous species absorbing in the near-UV range are formed; therefore, any attenuation of probing radiation can be definitely attributed to the appearance of condensed particles. Note that investigations into the optical properties of small carbon nanoparticles in diffusion flames [19,157,158] have shown that particles with a size of $2\text{--}4\text{ nm}$ are transparent in the visible range, but actively absorb in the near-UV range. In Fig. 52, the results of optical density measurements at temperatures above 1800 K, corresponding to the high-temperature wing of the “bell-shaped” curve are shown. It can be seen that with a decrease in wavelength, this wing is extended, and in the UV range, it transforms to a plateau up to temperatures close to 3000 K at which the processes of disintegration of the particles begins to prevail over growth processes [122].

Thus, it is possible to state that the commonly accepted conclusion on the decrease in yield and volume fraction of soot at temperatures above 1800 K, based on extinction measurements at 633 nm, could be justified only by the strict definition that “soot” is carbon particles in a narrow range of sizes (usually $20\text{--}40\text{ nm}$) with invariable extinction coefficients. If the yield and volume fraction of

Table 3

Temperatures of maximum of carbon particle yield in pyrolysis of various carbon bearing species. Ref. [67].

Carbon precursor	C ₃ O ₂	CCl ₄	C ₂ Cl ₄	C ₆ H ₆
T_{\max} , K	1600	1850	1770	1770

the condensed phase are attributed to all carbon particles, to some extent possessing properties of the condensed phase (i.e. containing more than ~ 100 carbon atoms and having a size not less than 1 nm; see [94]), then the temperature dependence of particle yield should be reconsidered.

The demonstrated data testify that the real volume fraction of the particles does not decrease with increased temperature, but instead the average size of particles is reduced, which leads to a decrease in the extinction coefficient in the visible range. If this assumption is correct, and the volume fraction remains approximately invariable in the temperature range from 1600 to 2800 K (see Fig. 52), the decrease in particle size should be connected with a corresponding growth in the particle number density in this temperature range. In other words, it is possible to suppose that increased temperature leads to slowed coagulation of primary clusters and results in an increase in the particle number density and, therefore, to a decrease in particle size at the moment when the initial carbon is consumed and the particle yield reaches 100%. A similar increase in the particle number density and a decrease in their size with increased temperature have also been observed in flames [152,153].

Indeed, for the ultimate conclusion about the invariability of yield and volume fraction of condensed particles in the temperature range starting from 100% decomposition of the initial molecules (1600–1800 K) and finishing at the temperature of noticeable particle disintegration (2800–3000 K), additional careful measurements of particle size and their optical properties are necessary.

7.2. Condensed phase growth rate

The next basic remarks concern the temperature dependence of the particle growth rate. Above, it was mentioned that the problems in understanding the observable dependences can be caused

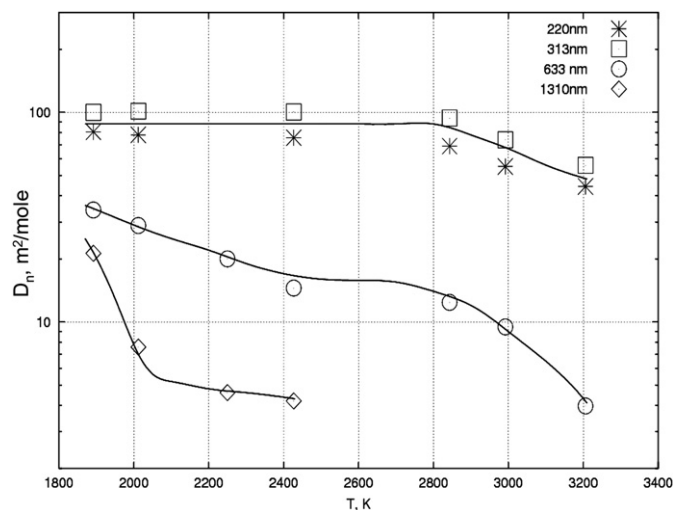


Fig. 52. Temperature dependence of final optical density D_n , observed during the pyrolysis of 0.2% C₃O₂ + Ar at different spectral wavelengths. Lines are the best fit of the experimental data. Ref. [42].

by disregarding the thermal effects of pyrolysis as well as the changes to particle optical properties. Let us consider these circumstances in more detail.

One such phenomena, difficult to interpret, is the break of temperature dependence of particle growth rate, observed in shock wave pyrolysis of a majority of precursors in the temperature range from 2200 to 2500 K [31,33,41,122] (see Figs. 36 and 37). One can see that up to these “break temperatures”, the rate of particle formation accelerates in all precursors. However, it is obvious that such behavior is correct until the reversal reactions of cluster and nanoparticle decay come into play. Toward higher temperatures, comparable with carbon evaporation (~ 4000 K), the particle formation rate becomes slower and, according to observations [122] at $T > 3400$ K, the rate of particle decay (evaporation) is already higher than the formation rate. Nevertheless, at temperatures below ~ 3000 K, these reversal processes are negligible and the kinetics of particle growth has to obey general regularities. We have already pointed out in Section 4.2 that temperatures of the observed break of dependencies $\ln k_f \sim 1/T$ are much less than the temperature of carbon phase transitions, so therefore the influence of the reversal process of particle decay on the apparent rate constant of particle growth is quite improbable. Therefore in the papers [42,44] another explanation for this phenomenon has been suggested.

To get a better understanding of the process of particle formation at various temperatures, let us look at the transformation of extinction time profiles with increased temperature, measured in [44] during the pyrolysis of C₃O₂ (Fig. 53). The first plot at $T = 1979$ K represents a typical one-stage process, which proceeds at this temperature very rapidly and results in considerable extinction. With a further temperature increase, the first stage of the process becomes even faster, but results in less extinction. However, on the following plot corresponding to $T = 2472$ K, besides the first rapid stage, it is possible to see a secondary process which develops after some delay and leads to additional extinction. A further temperature increase (see the plot at $T = 3343$ K) leads to a further decline and acceleration of the first stage and increase and slowing-down of the second stage of extinction growth. Thus, looking at these profiles, it becomes clear that it is necessary to consider the processes of primary growth of particles at low temperatures and secondary particle growth at higher temperatures as absolutely different phenomena. Therefore, for the analysis of primary particle growth in [44], it was suggested to analyze the data from the first stage of extinction increase with a continuously accelerating increase in temperature separately.

In Fig. 54a, b data are presented on the rate constant of particle growth k_f , obtained by approximation of the profiles of primary extinction growth during the pyrolysis of various precursors using the relaxation Equation (30). In Fig. 54a, the data are plotted versus the initial “frozen” temperature behind the shock wave, and in Fig. 54b versus the actually measured temperature of a mixture after pyrolysis and particle growth. One can see by such a consideration that the rate constant of particle growth in all considered mixtures can be described by a unified dependence:

$$k_f^{(1)} = 1.08 \cdot 10^{10} \exp \left(-195 (k \cdot \text{mol}^{-1}) / RT \right) (s^{-1}) \quad (38)$$

It is important to note that the obtained value of activation energy (195 kJ/mol) coincides well with the energy of activation of the rate constants of soot formation in the majority of the hydrocarbons measured not only in pyrolysis processes, but also in flames [6,31,33,121,152,153] (about 190 ± 20 kJ/mol). For the other hand, the absolute values of k_f , measured under various conditions, differ by more than one order of magnitude. Among the reasons for the difference in absolute values of k_f can be the different wavelengths

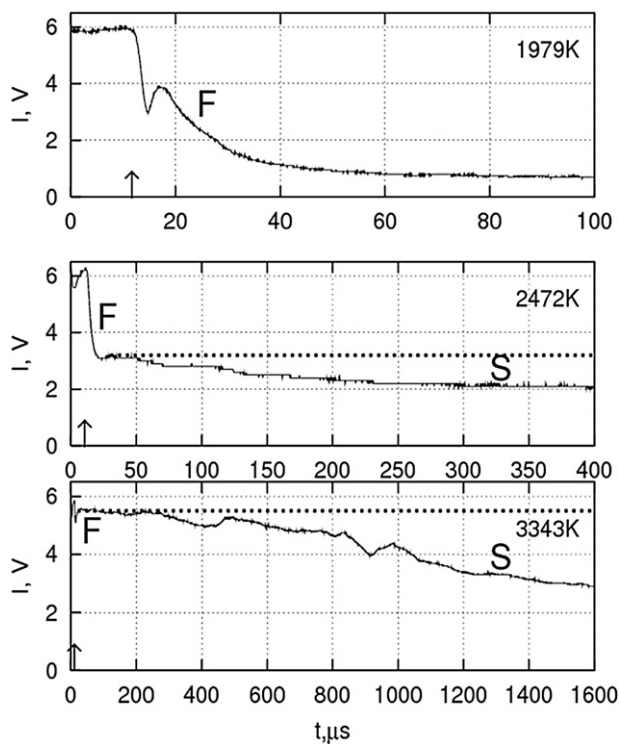


Fig. 53. Typical examples of extinction profiles, observed behind reflected shock waves at various temperatures. Mixture of 1% $C_3O_2 + Ar$. Pressures 15–20 bar. Vertical arrows mark the moment of reflected shock wave front passage. The stage F is the first extinction rise, the stage S is the secondary rise. The vertical scale is the same on all plots, while the horizontal time scale is more dense on each subsequent plot. Ref. [44].

at extinction used for k_f measurements [34] and neglecting the thermal effects of pyrolysis which cause a shift in the temperature scale (see Fig. 54a, b). Therefore, it is possible to draw a conclusion that the stage of carbon particle formation, registered by extinction, or more exactly, the rate of condensed phase growth, proceeds in all conditions approximately by the same mechanism, irrespective of the kind of a precursor and even the process type (pyrolysis or combustion).

The remaining question regards the physical reason for the acceleration of particle formation with increased temperature. The

apparent activation energy of about 200 kJ/mol should correspond to high threshold reactions, which do not match with the recombination-like reactions of particle surface growth. One interesting explanation for this phenomenon, based on the correlation of the decrease in particle size and the acceleration of particle formation with increased temperature, has been suggested in [42,44].

In these works, it was noted that the reduction in the final size of particles and the shortened time of achievement of this size obey the same laws. Analyzing this interrelation, the authors showed that the rate of achievement of a fixed size of particles does not change with temperature, i.e. the real processes of surface growth of particles do not accelerate with increased temperature (which is quite plausible neglecting the weak temperature dependence of the frequency of collisions). Thus, the observable acceleration in particle growth with increased temperature reflects only a faster completion of the process the surface growth, since the subsequent process of particle coagulation proceeds at much greater time scales and, as a rule, does not result in a noticeable contribution during observation in shock tube experiments (about 1–3 ms).

This important conclusion should stimulate further progress in modeling the very complicated process of carbon nanoparticle formation in gas phase reactions. In our opinion, at present, despite considerable efforts and a large body of published works, many debatable and ambiguous approaches still remain.

In Section 8, we will try to characterize in brief the present state-of-the-art in modeling the processes of carbon nanoparticle formation during the pyrolysis of various carbon-bearing species behind shock waves.

8. Numerical modeling of particle formation processes in pyrolysis reactions

Numerical modeling of carbon nanoparticle formation during pyrolysis and combustion has been investigated in a large number of studies. However, discussions on the kinetic mechanisms of formation and growth of condensed particles in the gas phase and modeling of these processes still continue.

The basic difficulty in kinetic modeling of the processes of cluster formation and micro-heterogeneous particles in chemically reacting systems is the elaboration of the numerical algorithm which allows for keeping the discrete character of any elementary chemical transformation with the participation of micro-

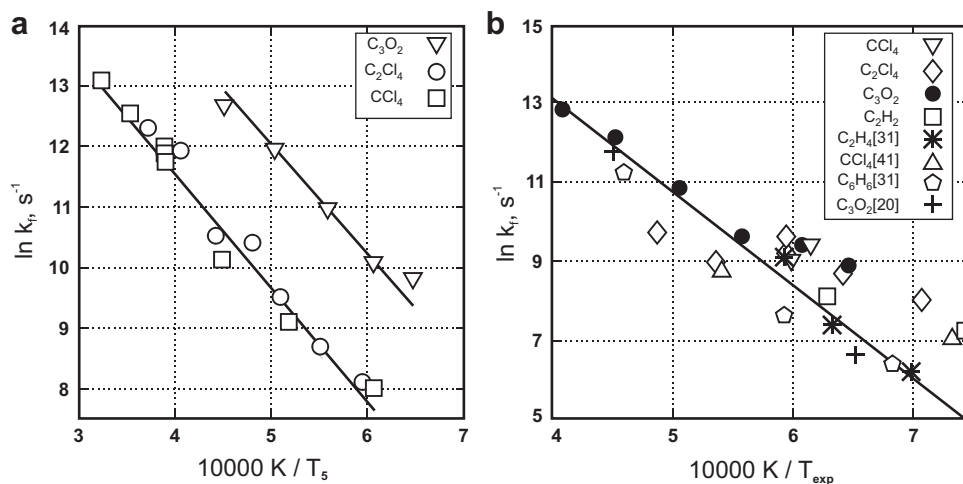


Fig. 54. Arrhenius dependence of rate constant of particle formation in various precursors plotted versus initial “frozen” temperature T_s (a) and versus real temperature T_{exp} (b) Ref. [44].

heterogeneous particles of any size, and to combine the kinetics of changes of all gas phase components and ensembles of micro-heterogeneous particles of the reacting system.

A fundamental problem of the kinetics of formation, growth and destruction of micro-heterogeneous particles is accounting for their structural characteristics, their influences on physical and chemical properties and the phase transitions of particles. From the point of view of fundamental science, clusters consist of atoms of various elements, so it is possible to consider them as a unique natural object. In the process of cluster formation and growth, cluster properties gradually change from purely molecular to macroscopic properties of the bulk material.

For a detailed model of the process of carbon nanoparticle formation, modern kinetic models consider gas phase reactions, which describe not only the pyrolysis and oxidation of an initial hydrocarbon molecule with the formation of simple fragments, but also the formation of heavy aliphatic and polyaromatic species consisting of several aromatic rings. However, already at this stage, the quantity of elementary stages can reach several thousand. Attempts to move forward on the scale of the particle sizes in such a way are doomed to failure. The quantity of elementary stages with the participation of more and more heavy particles, and, hence, the differential equations describing the time profiles of their concentration, will grow catastrophically. At the same time, the experimentally measured average sizes of carbon particles at characteristic times of about several milliseconds are in the 10 nm range, which corresponds to a number of atoms in the carbon particle of several hundred thousand or more. Therefore, in addition to gas kinetics methods, developing models should describe the growth of clusters of different sizes up to condensed particles. Moreover, to cover all aspects of the process of nanoparticle formation, models should consider not only the composition, but also the shape and structure of particles. The simplest modeling particles have a spherical form [159]. The following level of description is represented by fractal models [160]. In these models particles are described by two coordinates: size and certain form factors such as surface area [161].

For kinetic modeling of the formation of condensed carbon particles from the gas phase, the method of the moments [162,163] is currently most widely used. In this case, the system of the differential equations describing the block of gas phase reactions is completed by several new differential equations for the moments of the size distribution function of the condensed particles. The quantity of these equations depends on the number of condensed particles of various types, which are described in the language of the moments of function of the distribution and on the total number of considered moments of each size distribution function for particles of a certain type. Strictly speaking, only an infinite number of such moments are equivalent to the full particle size distribution function. However, for most practical applications and for the simulation of experimentally measured parameters, such as the molar fraction of soot, the specific surface of the ensemble of soot particles and the efficiency of absorption and scattering of optical radiation by the ensemble of particles is quite enough to describe several moments of the distribution function.

The methods of the moments are very fast, but they are limited by the one-dimensional or two-dimensional spaces of particles since the number of the moment equations exponentially increases with the number of coordinates of the particles. They also do not allow for determining the particle size distribution (PSD) without further assumptions on shape.

The discrete Galerkin method [164,165] represents another rather widespread approach for kinetic modeling of carbon particle formation in pyrolysis processes. The essence of this method consists of a representation of non-stationary PSD in the form of

series expansion in an orthogonal polynomial (Laguerre or Chebyshev) depending on a discrete parameter, the quantity of “monomers” in the condensed particle. Due to expansion by this discrete parameter, the given method allows for keeping the discrete structure of the kinetic equations, as well as in the case of a standard direct kinetic problem when each reaction is described by a separate differential equation. The description of the kinetics of transformations of micro-heterogeneous particles is based on the calculation of non-stationary PSD for particles of different kinds.

In the last few years the sectional schemes providing for discretization of H/C ratio in each section have been developed [166,167]. These models make it possible to follow not only the mass evolution of the particles, but also their hydrogen content. In addition, a fixed sectional aerosol dynamic model [168–172], valid over the entire Knudsen number regime, has been successfully implemented for studying the formation of soot agglomerates by simultaneous nucleation, coagulation, surface growth and condensation. These models have the advantage of decreasing numerical diffusion and increasing computational stability [170]. They provide a useful tool for studying nanoparticle formation behind shock waves. Sectional methods are also fast and they allow for calculating PSD; however, they are not suited for the description of different states of growing particles.

In the last ten years, Monte-Carlo algorithms have begun to be applied for the description of processes of nanoparticle formation [173–175]. The application of a kinetic Monte-Carlo method (KMC) and a method of molecular dynamics (MD) [176–178] has allowed for investigating the growth of single PAH molecules and graphene sheets. These methods can model very complex particles; however, high computing expenses currently interfere with the use these methods for modeling entire particle ensembles. Based on MD simulations in particular, authors [178] have suggested that particle inception can be considered as the result of a chemical growth and a physical coagulation. The contribution of these two pathways to the particle inception rate varies according to the combustion (or pyrolysis) conditions. In situations where the temperature and H concentration are relatively high ($T \sim 2200$ K), the inception rate is well described by the chemical growth. At lower temperatures, ($T \sim 1400$ K) with a relatively high PAH concentration and low H atoms available, particle inception can be mainly due to physical coagulation.

Coming back to the question of the detailed kinetic mechanisms of the formation of carbon particles, it is necessary to underline once again that until now, in the literature, there was no common opinion on the elementary processes which provide the most important contribution to the gradual transition from hydrocarbon molecules formed during pyrolysis reactions to the final structure composed of condensed carbon particles.

Note that the detailed analysis of various approaches to modeling the mechanisms responsible for the formation of condensed carbon particles is beyond the current paper and should be the subject of an independent review. For information on the modern concepts on the mechanisms of soot growth in combustion and pyrolysis processes, we address the reader to the surveys of Wang [111], Richter and Howard [179], Miller, Pilling and Troe [180] and also to recent original articles [175,181–183]. Here, we will give only a short summary on the basic kinetic models for the formation of soot and carbon nanoparticles, which can be found in the literature.

Historically, the first and up to now the most accepted kinetic model of soot growth is the so-called HACA (hydrogen abstraction carbon addition) model. According to this model, the key moment of the soot formation process is the surface mass growth of soot particles by reactions with gas phase molecules on the surface of soot particles. Frenklach and Wang [159] have proposed this HACA

abbreviation for the detailed kinetic mechanism of surface growth of soot particles based on the postulate that chemical reactions on the soot particle surface are similar to the chemical reactions of large polyaromatic hydrocarbon molecules. The essence of this mechanism is the reactions involving the detachment of a hydrogen atom and the addition of an acetylene molecule at certain sites of the polyaromatic hydrocarbon molecule, where four surface carbon atoms after the introduction of acetylene molecule directly form a new aromatic six-membered ring.

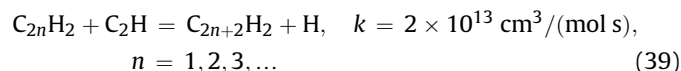
Later, Frenklach [184] showed that during the growth of polyaromatic molecules, a “zig-zag” surface is formed. This mechanism is inconsistent with the formation of special “arm-chair” sites on a particle surface for direct embedding of acetylene molecules with the formation of new aromatic rings (see Fig. 55, lower scheme). This contradiction was resolved by considering surface growth as a process involving the formation of hydrocarbons with aromatic-aliphatic bonds, or as a process connected with the formation five-membered rings on a surface of soot particles with the addition of acetylene molecules to the active center on the zig-zag surface of a soot particle (Fig. 55, upper scheme). After the formation of such a five-membered ring, it serves as a “nucleus” for the growth of the whole new layer on the soot particle surface.

The essence of the HACA model is most succinctly and clearly stated in the recent article by Frenklach [185]. The developed mechanism represents the growth of soot particles as a repetitive reaction sequence of two principal steps: (i) abstraction of a hydrogen atom from the reacting hydrocarbon by a gaseous hydrogen atom, followed by (ii) addition of a gaseous acetylene molecule to the newly-formed radical site. The first step activates a molecule for further growth by converting it to a radical and this reaction is reversible, while the reversibility of the second step, contributing to molecular growth, is dependent on the stability of the forming aromatics. So, the coupling between the “thermodynamic resistance” of the reaction’s reversibility and the kinetic driving force is the defining feature of the HACA model.

In the literature, it is possible to find other kinetic models of soot growth, in particular considering the polyacetylene pathway of soot formation. For the first time, the role of polyacetylene in soot formation was considered in the works of Homann-Wagner [186,187]. Later, in other studies [188,189], it was suggested as the so-called ‘polyynne model’.

The basic justification for the polyynne model is based on the fact that the thermodynamic stability of acetylene and polyynes C_nH_2 ($n = 2; 3; \dots$) grows as the temperature increases, whereas the stability of all other hydrocarbons decreases. In this model, it is assumed that the formation of condensed particles proceeds by the rapid polymerization of ‘supersaturated polyynne vapor’, continues with polymeric growth and, finally, pyrolytic carbon formation. Based on the high reaction ability of polyynes [190], Krestinin

[188,189] has affirmed that compared to a rather slow, multistage increase in the number of aromatic rings in PAHs, the polyynes grow in a simple and fast way [191,192], typically in:



The additional argument presented in [188,189] in support of the polyynne model is that the concentrations of the polyynes C_4H_2 , C_6H_2 , C_8H_2 are high enough to be detected as major hydrocarbon intermediates in both pyrolysis and combustion processes [186,192].

On the other hand, as it was noted by Richter-Howard [179], the model [188,189] does not include sufficiently detailed chemical reaction pathways to allow for a thorough assessment of its consistency with experimental observations. In particular, the chemical identity of the soot nucleus is not defined and the elementary reaction steps involved in their formation are not discussed. So, up to now, the weak point of the polyynne model is the absence of detailed description: how are the aromatic species formed and what are the structures of the initial cyclic products?

Additional arguments against the polyynne model have been reported in the recent papers [193,194], in which it was concluded that acetylene addition could be important for soot loading but does not contribute to particle inception. Therefore, later works have mostly considered the PAH pathway of soot formation [179–183]. Nevertheless, the possible contribution of aliphatic species to soot formation deserves further attention, and the latest discussion of this problem can be found in a recent review [111].

Note that all the models mentioned are based on an essential role of hydrocarbon molecules in soot building. However experiments carried out recently on hydrogen-free mixtures [20,34,36,40–42,44,56,122,129] have shown that the kinetics of formation and the structure of formed carbon particles in such systems is similar to those of usual soot. It has stimulated the development of the new kinetic models, describing the consecutive growth of carbon clusters (without hydrogen participation) up to the formation of micro-heterogeneous condensed particles.

Based on recent experimental results [122,195], authors [95,196] have proposed a model of condensation of carbon atoms formed during thermal decomposition of the hydrogen-free precursor C_3O_2 behind shock waves. The kinetic model consisted of several sets of reactions: a set of gas phase reactions of the thermal decomposition of C_3O_2 , which was carefully investigated by Friedrichs and Wagner [120] and a set of gas phase reactions of small carbon clusters proposed in [197]. These complex chemical pathways of formation of small carbon clusters have been extended to describe large carbonaceous nanoparticles using a discrete Galerkin method. As a result, these authors have succeeded in describing quite well the experimentally measured parameters of the process of hydrogen-free particle formation: induction time (Fig. 56a), particle growth rate (Fig. 56b) and particle yield (Fig. 57) in the temperature range 1200–2500 K. However, in these studies, a large difference between the prediction and measurement of particle yields and average particle size at the higher temperature range (3000–4000 K) took place. This was attributed to the lack of description of the agglomerated structure of particles in these models [198].

Later, a fixed sectional aerosol dynamic model was successfully implemented [96] to describe more correctly the experimentally measured temperature dependence of carbon particle volume fraction in hydrogen-free mixtures. In Fig. 58, the results of modeling the double bell-shaped temperature dependence of carbon particle yield [42], presented in [96], are shown.

It is necessary to underline that a successful description of the processes of hydrogen-free carbon particle formation, which

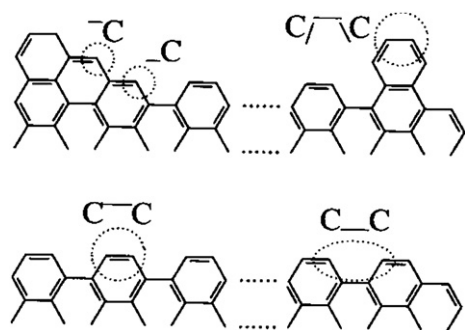


Fig. 55. A schematic diagram of the initial surface model with a one-dimensional armchair substrate (lower picture) and identification of reaction sites (upper picture). Ref. [184].

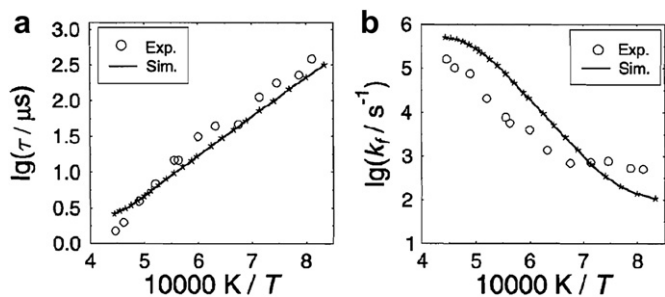


Fig. 56. Comparison of calculated and experimentally measured [20] induction time τ (a) and rate constant k_f (b) of carbon particle formation in the mixture of 0.33% C_3O_2 in argon at a pressure of 50 bar. Ref. [95].

appears to be rather similar to soot formation processes during the pyrolysis of hydrocarbons, has enhanced the discussion on the role of hydrogen and various types of poly-hydrocarbons in the formation of carbon nanoparticles.

In [199,200], an attempts were made to elaborate the kinetic model which combines the existing detailed kinetic models of soot formation (the H abstraction, C_2H_2 addition (HACA) [159] and polyne [189] models), the mechanism of acetylene pyrolysis [201,202] and the mechanism of pure carbon cluster formation [95] within a unique kinetic scheme. In this scheme, the authors kept the reaction mechanism and the entire set of the rate coefficients fixed. The calculations were performed for hydrocarbons with different chemical structures (aliphatic and aromatic) within a wide temperature and pressure range. The comparison of the calculations with the experimental measurements of the induction times, observable rates of soot particle growth and soot yields in the pyrolysis of different hydrocarbons in shock tube experiments have shown that the coincidence is quantitatively good for all the main parameters of soot formation. Later, based on these results, a simplified empirical (two-equation), model was suggested and applied for soot formation simulation [203]. Authors have shown that a good coincidence between the experimentally measured and calculated results can be achieved with relatively small computational effort.

Concerning the agreement between experiments and calculations, demonstrated in Figs. 56–58, it is necessary to make an

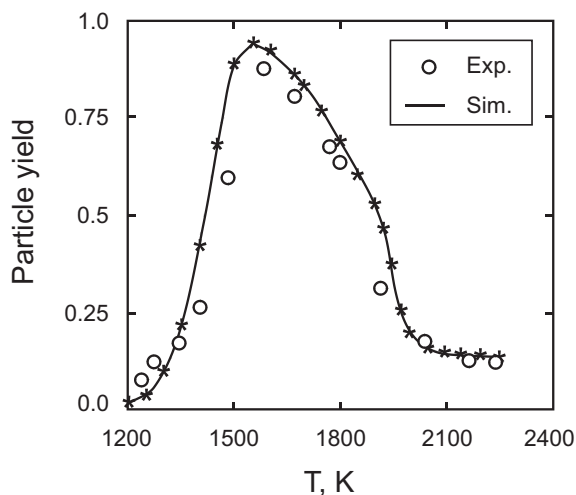


Fig. 57. Comparison of calculated and experimentally measured [20] yield of carbon particle formation in the mixture of 0.33% C_3O_2 in argon at a pressure of 50 bar. Ref. [95].

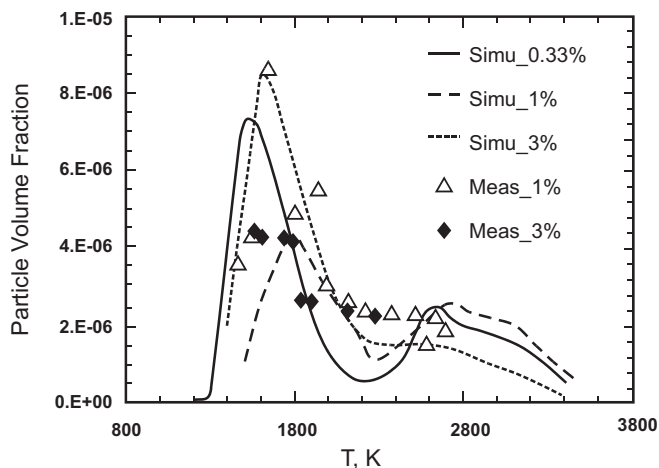


Fig. 58. Temperature dependence of particle volume fraction for different mixtures. Solid line for the 0.33% $\text{C}_3\text{O}_2/\text{Ar}$ mixture at 50 bar; long dashed line for the 1% $\text{C}_3\text{O}_2/\text{Ar}$ mixture at 20 bar; short dashed line for the 3% $\text{C}_3\text{O}_2/\text{Ar}$ mixture at 4.6 bar; measurements [42]; empty squares for the 1% mixture; solid diamonds for the 3% mixture. Ref. [96].

important point: Most experimental data on the induction time of particle formation, the rate constant of particle growth and particle yield, are obtained from extinction measurements at 633 nm. As has been discussed above (see Section 7), such measurements reflect the behavior of particles with sizes not less than 5–10 nm, since particles of smaller size are transparent at this wavelength. By rough estimates such particles contain not less than $n = 10^4$ carbon atoms. On the other hand, in calculations [95,96,196,198], the critical number of atoms at which particles are considered to be solid soot-like particles, is usually accepted equal as $n = 84$ [94], which corresponds to particles less than 1 nm in size. It is quite probable that an increase in the critical size of particles attributed in the calculations to the condensed phase, or a comparison with data from UV extinction studies registering smaller particles, would require appreciable amendments to the developed models.

Moreover, in our opinion, a number of key questions about these models remain unsolved, they are connected to the structural transformation of particles at the stage of transition from poly-hydrocarbon molecules or carbon clusters, which do not yet possess the properties of condensed particles, to final particles, the properties of which in all cases are close to the well-studied properties of soot particles.

It is necessary to underline once again that almost all experimental dependences used for the testing of modeling results are obtained with the assumption that the optical, and in some cases thermodynamic properties of registered particles are invariable (and as a rule, coincide with the known properties of soot), both at different process times and at different temperatures. However, we have shown that this is certainly not so, and an account of the real properties of particles at different stages of their growth and at different temperatures can essentially change the current picture of the process.

9. Conclusions

9.1. General remarks regarding the mechanisms of carbon particle formation in gas phase reactions

The present review demonstrates that in spite of nearly a half century of numerous investigations into the processes of carbon

nanoparticle formation from the gas phase in shock wave pyrolysis, this problem is still far from a final solution.

Indeed, it is now clear how this complex process develops over time, how formed particles appear at various temperatures, pressures and concentrations, and the various kinds of initial carbon-containing precursors. The collected experimental material represents extensive information on the induction times of carbon nanoparticle formation under various conditions; less exhaustive information is available about the growth rates of particles and their final sizes under different pyrolysis conditions. Yet, data on the detailed properties of formed particles – their structure, density, heat capacity and absorption spectra are lacking. The exception is, perhaps, only particles of usual soot, formed under typical combustion conditions; however, as has been shown in the current review, the conditions of shock-wave pyrolysis essentially expand the range of parameters of the process, and, accordingly, the range of properties of the formed particles.

Further progress in these investigations should be directed toward essential advances in understanding the complex (and still widely debated), mechanisms of formation and growth of carbon nanoparticles in high-temperature gas reactions. One of the key questions of this problem is the role of hydrogen in the formation of condensed carbon particles. It is well known that the pyrolysis of any hydrocarbon molecule does not directly yield carbon clusters, but instead propagates by way of consecutive growth of hydrocarbon radicals. Based on this, researchers disagree about the role of aliphatic and aromatic radicals in the formation of soot particles during the pyrolysis and combustion of various hydrocarbon fuels. However, the data summarized in the present review shows that the particles obtained from hydrogen-free precursors (i.e. formed by the direct growth of carbon clusters), have a structure similar to the structure of normal soot. So, the question is now at which stage of the process do both pathways (hydrocarbon and carbon cluster growth), combine to a unified mechanism of formation of condensed carbon particles?

Moreover, we have shown that the growth rates of condensed carbon particles observed in experiments are nearly identical for all precursors. Thus, the observed differences in the process of carbon nanoparticle formation during the pyrolysis of various substances are likely related only to the initial stages of growth of heavy hydrocarbons (or carbon clusters). The sub-nanometer particles formed at these stages of the process are transparent in the visible and near-UV spectral ranges; therefore they are very difficult to register, even by means of modern diagnostic methods. The only optically observed parameter at this stage of the process is the induction time of absorbing particles. Therefore certain prospects in this direction can be achieved only by the development of new diagnostic tools, for example time-of-flight mass spectroscopy (TOF-MS), which can register radicals and clusters with mass numbers up to 1000 amu and more with a time resolution of 10^{-6} – 10^{-5} s. Any experimental information on the behavior of such sub-nanometer particles can help to expand our understanding and the possibilities of modeling the mechanisms of their growth and thus, to complete an overall picture of this complex phenomenon.

Acknowledgments

The author would like to thank Professor H. Gg. Wagner (Göttingen), for the inspiration to write this review and for valuable discussions during the course of its preparation. The financial support of Deutsche Forschungsgemeinschaft and Russian Foundation for Basic Researches is gratefully acknowledged.

References

- [1] Merchan-Merchan W, Saveliev AV, Kennedy L, Jimenez WC. Combustion synthesis of carbon nanotubes and related nanostructures. *Prog Energy Combust Sci* 2010;36(6):696–727.
- [2] Goel A, Hebggen P, Vander Sande JB, Howard JB. Combustion synthesis of fullerenes and fullerene nanostructures. *Carbon* 2002;40(2):177–82.
- [3] Rashid A. CVD of carbon thin films and micro/nano-structures: light assisted chemical vapor deposition of carbon. LAP LAMBERT Academic Publishing; 2010.
- [4] Pierson HO. Handbook of chemical vapor deposition: principles, technology and applications. William Andrew; 1999.
- [5] Loutfy RO. Growth of carbon nanotubes by arc discharge and laser ablation. In: Carbon nanotubes science and applications. Boca Raton London New York Washington, D.C: CRC PRESS; 2005. 65–98.
- [6] Haynes BS, Wagner HG. Soot formation. *Prog Energy Combust Sci* 1981;7(4):229–73.
- [7] Glassman I. Soot formation in combustion processes. *Proc Combust Inst* 1989;22:295–311.
- [8] Kern RD, Xie K. Shock tube studies of gas phase reactions preceding the soot formation process. *Prog Energy Combust Sci* 1991;17(3):191–210.
- [9] Bhaskaran KA, Roth P. The shock tube as wave reactor for kinetic studies and material synthesis. *Prog Energy Combust Sci* 2002;28(2):151–92.
- [10] Wang H. Particulate formation and analysis. In: Ben-Dor G, Irga O, Elperin T, editors. Handbook of shock waves. Chemical reactions in shock waves and detonation, vol.3. San Diego, London: Academic Press; 2001. p. 257–308.
- [11] Michael JV, Lim KP. Shock tube techniques in chemical kinetics. *Annu Rev Phys Chem* 1993;44:429–58.
- [12] Tranter RS, Brezinsky K, Fulle D. Design of a high-pressure single pulse shock tube for chemical kinetic investigations. *Rev Sci Instrum* 2001;72:3046–54.
- [13] Zeldovich YB, Raizer YP. Physics of shock waves and high-temperature hydrodynamic phenomena. Moscow: Physmathgiz; 1963.
- [14] Gaydon A, Hurler IR. The shock tube in high-temperature chemical physics. London: Chapman and Hall Ltd; 1963.
- [15] Tsang W, Lifshitz A. Single pulse shock tube. In: Ben-Dor G, Irga O, Elperin T, editors. Handbook of shock waves. Chemical reactions in shock waves and detonation, vol.3. San Diego, London: Academic Press; 2001. p. 107–210.
- [16] Lee SC, Tien CL. Optical constants of soot in hydrocarbon flames. *Proc Combust Inst*; 1981:1159–66.
- [17] Dalzell WH, Sarofim AF. Optical constants of soot and their application to heat flux calculations. *J Heat Transfer*; 1969:91–100.
- [18] Smyth KC, Shaddix CR. The elusive history of $m = 1.57 - 0.56i$ for the refractive index of soot. *Combust Flame* 1996;107(3):314–20.
- [19] Basile G, Rolando A, D'Alessio A, D'Anna A, Minatolo P. Coagulation and carbonization processes in slightly sooting premixed flames. *Proc Combust Inst* 2002;29:2391–9.
- [20] Dörge KJ, Tanke D, Wagner HG. Particle formation in carbon suboxide pyrolysis behind shock waves. *Zeit Phys Chem* 1999;212:219–29.
- [21] Bohren CF, Huffman DR. Absorption and scattering of light by small particles. New York: Wiley; 1983.
- [22] Fussey DE, Gosling AJ, Lampard D. A shock-tube study of induction times in the formation of carbon particles by pyrolysis of the C_2 hydrocarbons. *Combust Flame* 1978;32:181–92.
- [23] Graham SC. The collisional growth of soot particles at high temperatures. *Proc Combust Inst* 1977;16:663–9.
- [24] Yoshizawa Y, Kawada H, Kurokawa M. A shock-tube study on the process of soot formation from acetylene pyrolysis. *Proc Combust Inst* 1979;17(1):1375–81.
- [25] Frenklach M, Taki S, Matula RA. A conceptual model for soot formation in pyrolysis of aromatic hydrocarbons. *Combust Flame*; 1983:275–82.
- [26] Frenklach M, Taki S, Durgaprasad MB, Matula RA. Soot formation in shock-tube pyrolysis of acetylene, allene, and 1,3-butadiene. *Combust Flame* 1983 Dec;54(1–3):81–101.
- [27] Alexiou A, Williams A. Soot formation in shock-tube pyrolysis of toluene, toluene-methanol, toluene-ethanol, and toluene-oxygen mixtures. *Combust Flame* 1996 Jan;104(1–2):51–65.
- [28] Wang TS, Matuda RA, Farmer RC. Combustion kinetics of soot formation from toluene. *Proc Combust Inst* 1981;18:1149–58.
- [29] Rawlins WT, Cowles LM, Krech RH. Spectral signatures (0.2–5 μ m) of soot initiation in the pyrolysis of toluene near 2000 K. *Proc Combust Inst* 1985;20(1):879–86.
- [30] Simmons B, Williams A. A shock tube investigation of the rate of soot formation for benzene, toluene, and toluene/n-heptane mixtures. *Combust Flame* 1988;71(3):219–32.
- [31] Bauerle S, Karasevich Y, Slavov St, Tanke D, Tappe M, Thienel T, et al. Soot formation at elevated pressures and carbon concentrations in hydrocarbon pyrolysis. *Proc Combust Inst* 1994;25(1):627–34.
- [32] Alexiou A, Williams A. Soot formation in shock-tube pyrolysis of pyridine and toluene-pyridine mixtures. *Fuel* 1994 Aug;73(8):1280–3.
- [33] Knorre VG, Tanke D, Thienel T, Wagner HG. Soot formation in the pyrolysis of benzene/acetylene and acetylene/hydrogen mixtures at high carbon concentrations. *Proc Combust Inst* 1996;26(2):2303–10.
- [34] Emelianov A, Eremin A, Jander H, Wagner HG, Borchers C. Spectral and structural properties of carbon nanoparticle forming in C_3O_2 and C_2H_2 pyrolysis behind shock waves. *Proc Combust Inst* 2002;29(2):2351–7.

- [35] D'Alessio J, Lazzaro M, Massoli P, Moccia V. Absorption spectroscopy of toluene pyrolysis. *Opt Lasers Eng* 2002;37(5):495–508.
- [36] Starke R, Kock B, Roth P, Eremin A, Gurentsov E, Shumova V, et al. Shock wave induced carbon particle formation from CCl_4 and C_3O_2 observed by laser extinction and by laser-induced incandescence (LII). *Combust Flame* 2003;135(1–2):77–85.
- [37] Iuliis SD, Chaumeix N, Idir M, Paillard CE. Scattering/extinction measurements of soot formation in a shock tube. *Exp Thermal Fluid Sci* 2008;32(7):1354–62.
- [38] Starke R, Roth P. Soot particle sizing by LII during shock tube pyrolysis of C_6H_6 . *Combust Flame* 2001;127(4):2278–85.
- [39] Graham SC, Homer JB, Rosenfeld JL. The formation and coagulation of soot generated by the pyrolysis of aromatic hydrocarbons. *Proc Roy Soc London* 1975;344:259–85.
- [40] Frenklach M, Hsu JP, Miller DL, Matula RA. Shock-tube pyrolysis of chlorinated hydrocarbons: formation of soot. *Combust Flame* 1986;64(2):141–55.
- [41] Starikovskiy AY, Thienel T, Wagner HG, Zaslonko IS. Soot formation in the pyrolysis of halogenated hydrocarbons. Part I, binary mixtures of carbon tetrachloride with hydrogen and iron pentacarbonyl. *Ber Bunsenges Phys Chem* 1998;102:1815–22.
- [42] Emelianov A, Eremin A, Gurentsov E, Makeich A, Jander H, Wagner HGG. Time and temperature dependence of carbon particle growth in various shock wave pyrolysis processes. *Proc Combust Inst* 2005;30:1433–40.
- [43] Agafonov G, Smirnov V, Vlasov P. Soot formation at pyrolysis of benzene, methyl-benzene and ethyl-benzene in shock waves. *Kinet Catal* 2011;52(3):358–70.
- [44] Emelianov A, Eremin A, Jander H, Wagner HGG. To the temperature dependence of carbon particle formation in shock wave pyrolysis processes. *Z Physikalische Chem* 2003;217:893–910.
- [45] Eremin A, Gurentsov E, Popova E, Priemchenko K. Size dependence of complex refractive index function of growing particles. *Appl Phys B* 2011;104(2):285–95.
- [46] Charalampopoulos TT, Chang H. In situ optical properties of soot particles in the wavelength range from 340 nm to 600 nm. *Comb Sci Technol* 1988;59:401–21.
- [47] Graham SC, Homer JB. Light scattering measurements on aerosols in a shock tube. 9th international shock tube symposium. In: Berschader D, Griffith W, editors. Recent development in shock tube research. Stanford: University Press; 1973. p. 712–9.
- [48] Kellerer H, Muller A, Bauer H-J, Wittig S. Soot formation in a shock tube under elevated pressure conditions. *Combust Sci Technol* 1996;113:67–80.
- [49] Kellerer H, Bauer H-J, Wittig S. Soot formation from rich hydrocarbon oxidation under elevated pressure conditions. 20th Int. Symp. on Shock Waves 1996;947–952.
- [50] Kellerer H, Wittig S. Growth and coagulation of soot particles at high pressures. In: Proc. of 21th Int Symp. on Shock Waves. 1998; 21:177–182.
- [51] Kellerer H, Koch R, Wittig S. Measurements of the growth and coagulation of soot particles in a high-pressure shock tube. *Combust Flame* 2000;120(1–2):188–99.
- [52] di Stasio S, Massoli P, Lazzaro M. Retrieval of soot aggregate morphology from light scattering/extinction measurements in a high pressure high temperature environment. *J Aerosol Sci* 1996;27(6):897–913.
- [53] D'Alessio A, Minutolo P, Gambi G, D'Anna A. Optical characterization of soot. *Ber Buns Phys Chem* 1993;97(12):1574–8.
- [54] Snelling D, Liu F, Smallwood G, Gülder Ö. Determination of the soot absorption function and thermal accommodation coefficient using low-fluence LII in a laminar coflow ethylene diffusion flame. *Combust Flame* 2004;136:180–90.
- [55] Tsuboi T, Ishii K, Omura H. Spectral intensity measurement for soot formation of benzene behind reflected shock waves. *Shock Waves* 2002;12:121–8.
- [56] Deppe J, Emelianov A, Eremin A, Wagner HGG. Formation of carbon nanoparticle in carbon suboxide pyrolysis behind shock wave. *Z Physikalische Chem* 2002;216:641–58.
- [57] Zhil'tsova IV, Zaslonko IS, Karasevich YK, Wagner HGG. Nonisothermal effects in the process of soot formation in ethylene pyrolysis behind shock waves. *Kinet Catal* 2000;41:76–89.
- [58] Ishii K, Ohashi N, Teraji A, Kubo M. Soot formation in hydrocarbon pyrolysis behind reflected shock waves. *Proc 22nd IDERS*; 2009. Minsk 27–31.
- [59] Melton LA. Soot diagnostics based on laser heating. *Appl Opt* 1984;23:2201–8.
- [60] Penner SS. Quantitative molecular spectroscopy and gas emissivities. Addison-Wesley Educational Publishers Inc; 1959.
- [61] Stupochenko EV, Losev SA, Osipov AI. Relaxation in shock waves. Berlin: Springer Verlag; 1967.
- [62] Vollrath Herausgegeben von K, Thomer G. Kurzzeitphysik. Wien, New York: Springer-Verlag; 1967.
- [63] Ahasov O, Kudriavtsev N, Novikov S, Soloukhin P, Fomin N. Diagnostics of nonequilibrium states in molecular lasers. Minsk: Nauka i tekhnika; 1985.
- [64] Dyer TM, Flower WL. In: Sieglar DC, Smith GW, editors. In particulate carbon: formation during combustion. New York: Plenum Press; 1981.
- [65] Jenkins TP, Hanson RK. Soot pyrometry using modulated absorption/emission. *Combust Flame* 2001;126:1669–79.
- [66] Jeffries JB, Schulz C, Mattison DW, Oehlschlaeger MA, Bessler WG, Lee T, et al. UV absorption of CO_2 for temperature diagnostics of hydrocarbon combustion applications. *Proc Combust Inst* 2005;30:1591–9.
- [67] Drakon AV, Emelianov AV, Eremin AV, Makeich AA, Schulz C. Experimental definition of thermal effects of processes of pyrolysis carbon containing molecules and carbon particles formation behind shock waves. Physical—chemical kinetics in gasdynamics. Available from: <http://www.chemphys.edu.ru/article/58/>; 2007.
- [68] Vander Wal RL, Dietrich DL. Laser-induced incandescence applied to droplet combustion. *Appl Opt* 1995;34:1103.
- [69] Ni T, Pinson JA, Gupta S, Santoro RJ. Two-dimensional imaging of soot volume fraction by the use of laser-induced incandescence. *Appl Opt* 1995;34(30):7083–91.
- [70] Snelling DR, Thomson KA, Smallwood GJ, Gulder OL. Two-dimensional imaging of soot volume fraction in laminar diffusion flames. *Appl Opt* 1999;38:2478–85.
- [71] Schulz C, Kock BF, Hofmann M, Michelsen H, Will S, Bougie B, et al. Laser-induced incandescence: recent trends and current questions. *Appl Phys B* 2006;83:333–54.
- [72] Starke R, Roth P. Soot particle sizing by LII during shock tube pyrolysis of C_6H_6 . *Combust Flame* 2002;127:2278–85.
- [73] Woiki D, Roth P. LII particle sizing in shock tube experiments on reactive gas/particle mixtures. *Proc 22nd int symp shock waves*; 2000. Southampton 417–421.
- [74] Woiki D, Giesen A, Roth P. Time-resolved laser-induced incandescence (LII) for soot particle sizing during acetylene pyrolysis behind shock waves. *Proc Combust Inst* 2000;28:2531–7.
- [75] Starke R, Kock B, Roth P. Nano-particle sizing by laser-induced-incandescence (LII) in a shock wave reactor. *Shock Waves* 2003;12(5):351–60.
- [76] Therssen E, Bouvier Y, Schoemaecker-Moreau C, Mercier X, Desgroux P, Ziskind M, et al. Determination of the ratio of soot refractive index function $E(m)$ at the two wavelengths 532 and 1064 nm by laser induced incandescence. *App Phys B Lasers Opt* 2007;89(2–3):417–27.
- [77] Lemaire R, Faccinotto A, Therssen E, Ziskind M, Focsa C, Desgroux P. Experimental comparison of soot formation in turbulent flames of diesel and surrogate diesel fuels. *Proc Combust Inst* 2009;32:737–44.
- [78] Lemaire R, Therssen E, Desgroux P. Effect of ethanol addition in gasoline and gasoline-surrogate on soot formation in turbulent spray flames. *Fuel* 2010;89:3952–9.
- [79] Roth P, Filippov AV. In situ ultrafine particle sizing by a combination of pulsed laser heatup and particle thermal emission. *J Aerosol Sci* 1996;27(1):95–104.
- [80] Michelsen H. Understanding and predicting the temporal response of laser-induced incandescence from carbonaceous particles. *J Chem Phys* 2003;118:7012–45.
- [81] Tekasakul P, Loyalka SK. Evaporation from non-spherical particles: the equivalent-volume and inscribed sphere approximations for nearly spherical particles. *Aerosol Sci* 2002;33:307–17.
- [82] Daun KJ, Smallwood GJ, Liu F. Molecular dynamics simulations of translational thermal accommodation coefficients for time-resolved LII. *Appl Phys B* 2009;94:39–49.
- [83] Michelsen HA. Derivation of a temperature-dependent accommodation coefficient for use in modeling laser-induced incandescence of soot. *Appl Phys B* 2009;94:103–17.
- [84] Daun KJ, Smallwood GJ, Liu F. Investigation of thermal accommodation coefficients in time-resolved laser-induced incandescence. *J Heat Transfer* 2008;130(12):121201–301.
- [85] Eremin AV, Gurentsov EV, Hofmann M, Kock B, Schulz C. TR LII for sizing of carbon particle forming at room temperature. *Appl Phys B* 2006;83:449–54.
- [86] Kock B, Kayan C, Knipping J, Ortner HR, Roth P. Comparison of LII and TEM sizing during synthesis of iron particle chains. *Proc Combust Inst* 2004;30:1689–98.
- [87] Smallwood GJ, Snelling DR, Liu F, Gulder OL. Clouds over soot evaporation: errors in modeling laser-induced incandescence of soot. *Trans ASME* 2001;123:814–9.
- [88] Leider HR, Krikorian OH, Young DA. Thermodynamic properties of carbon up to the critical point. *Carbon* 1973;11:555–63.
- [89] Köylü ÜÖ. Quantitative analysis of in situ optical diagnostics for inferring particle/aggregate parameters in flames: implications for soot surface growth and total emissivity. *Combust Flame* 1996;109:488–500.
- [90] Köylü ÜÖ, Faeth GM. Spectral extinction coefficients of soot aggregates from turbulent diffusion flames. *J Heat Transfer* 1996;118:415–21.
- [91] Krishnan SS, Lin K-S, Faeth GM. Extinction and scattering properties of soot emitted from buoyant turbulent diffusion flames. *J Heat Transfer* 2001;123(2):331–9.
- [92] Michelsen HA, Liu F, Kock B, Bladh H, Boiarciuc A, Charwath M, et al. Modeling laser-induced incandescence of soot: a summary and comparison of LII models. *Appl Phys B* 2007;87:503–21.
- [93] Gurentsov E, Eremin A. Measurement of size of carbon and iron nanoparticles by laser induced incandescence. *High Temperatures* 2011;49:668–75.
- [94] Ishiguro T, Takatori Y, Akihama K. Microstructure of diesel soot particle probed by electron microscopy: first observation of inner core and outer shell. *Combust Flame* 1997;108:231–4.
- [95] Sojka J, Warnatz J, Vlasov PA, Zaslonko IS. Kinetic modeling of carbon suboxide thermal decomposition and formation of soot-like particles behind shock waves. *Combust Sci Technol* 2000;158:439–60.

- [96] Wen JZ, Thompson MJ, Lightstone MF. Numerical study of carbonaceous nanoparticle formation behind shock waves. *Combust Theory Model* 2006;10(2):257–72.
- [97] Ben-Dor G, Irga O, Elperin T, editors. *Handbook of shock waves*. San Diego, London: Academic Press; 2001.
- [98] Bradley JN, Kistiakowsky GB. Shock wave studies by mass spectrometry. I. Thermal decomposition of Nitrous Oxide. *J Chem Phys* 1961;35:256–64.
- [99] Garnett SH, Kistiakowsky GB, O'Grady BV. Isotopic exchange between oxygen and carbon monoxide in shock waves. *J Chem Phys* 1969;51:84–92.
- [100] Kern RD, Singh HJ, Esslinger MA, Winkler PW. Product profiles observed during the pyrolyses of toluene, benzene, butadiene, and acetylene. *Proc Combust Inst* 1982;19:1351–8.
- [101] Singh HJ, Kern RD. Pyrolysis of benzene behind reflected shock waves. *Combust Flame* 1983;54(1–3):49–59.
- [102] Kern RD, Xie K, Chen H, Kiefer JH. High temperature pyrolysis of acetylene and diacetylene behind reflected shock waves. *Proc Combust Inst* 1991;23:69–75.
- [103] Kern RD, Singh HJ, Zhang Q. Chemical and combustion kinetics 16.1 mass spectrometric methods for chemical kinetics in shock tubes. *Handbook of shock waves*; 2001. 1–27.
- [104] Tranter RS, Giri BR, Kiefer JH. Shock tube/time-of-flight mass spectrometer for high temperature kinetic studies. *Rev Sci Instr* 2007;78:034101–11.
- [105] Giri BR, Tranter RS. Dissociation of 1,1,1-Trifluoroethane behind reflected shock waves: shock tube/time-of-flight mass spectrometry experiments. *J Phys Chem A* 2007;111:1585–92.
- [106] Emelianov AV, Eremin AV, Jander H, Wagner HGg. Carbon condensation wave in C_3O_2 and C_2H_2 initiated by a shock wave. *Proc Combust Inst* 2011;33:525–32.
- [107] Dobbins RA, Fletcher RA, Lu W. Laser microprobe analysis of soot precursor particles and carbonaceous soot. *Combust Flame* 1995;100:301–9.
- [108] Faccineto A, Desgroux P, Ziskind M, Therssen E, Focsa C. High-sensitivity detection of polycyclic aromatic hydrocarbons adsorbed onto soot particles using laser desorption/ionization/time-of-flight mass spectrometry: an approach to studying the soot inception process in low-pressure flames. *Combust Flame* 2011;158:227–39.
- [109] Mathieu O, Frache G, Djebaili-Chaumeix N, Paillard C-E, Krier G, Muller J-F, et al. Characterization of adsorbed species on soot formed behind reflected shock waves. *Proc Combust Inst* 2007;31:511–9.
- [110] Mathieu O, Frache G, Djebaili-Chaumeix N, Paillard C-E, Krier G, Muller J-F, et al. Laser desorption–ionization time-of-flight mass spectrometry for analyses of heavy hydrocarbons adsorbed on soot formed behind reflected shock waves. *Proc Combust Inst* 2009;32:971–8.
- [111] Wang H. Formation of nascent soot and other condensed-phase materials in flames. *Proc Combust Inst* 2011;33:41–67.
- [112] Vander Wal RL, Bryg VM, Hays MD. Fingerprinting soot (towards source identification): physical structure and chemical composition. *J Aerosol Sci* 2010;41(1):108–17.
- [113] Starke R, Kock B, Roth P. Nano-particle sizing by laser-induced-incandescence (LII) in a shock wave reactor. *Shock Waves* 2002;12(5):351–60.
- [114] Hooker WJ. Shock tube studies of acetylene decomposition. *Proc Combust Inst* 1959;7:949–52.
- [115] Tanzawa T, Gardiner Jr WC. Thermal decomposition of acetylene. *Proc Combust Inst* 1979;17(1):563–73.
- [116] Douce F, Djebaili-Chaumeix N, Paillard C-E, Clinard, Rouzaud J-N. Soot formation from heavy hydrocarbons behind reflected shock waves. *Proc Combust Inst* 2000;28:2523–9.
- [117] Djebaili-Chaumeix N, Ladril D, Paillard C-E. Experimental study on soot formation from heavy hydrocarbons representative of gasoline fuels. In: Roy GD, Frolov SM, Starik AM, editors. *Combustion atmospheric pollution*. Moscow: Torus Press; 2003. p. 411–7.
- [118] Tanke D. *Russbildung in der Kohlenwasserstoffpyrolyse hinter Stosswelle* [dissertation]. Göttingen Universität, Germany 1994.
- [119] Clar E, Kelly W, Robertson JM, Rossmann JM. Circumanthracene und dinaphtho (7': 1'-1: 13) (1'': 7'' -6: 8)-peropyrene. *J Chem Soc*; 1956:3878–81.
- [120] Friedrichs G, Wagner HGg. Investigation of the thermal decay of carbon suboxide. *Zeit Phys Chem* 1998;203(1):1–14.
- [121] Haynes BS, Wagner HGg. The surface growth phenomenon in soot formation. *Zeit Phys Chem* 1982;133:201–13.
- [122] Deppe J, Emelianov A, Eremin A, Jander H, Wagner HGg, Zaslonko I. Carbon particle formation and decay in two-step pyrolysis of carbon suboxide behind shock waves. *Proc Combust Inst* 2000;28:2515–22.
- [123] Eremin AV, Gurentsov EV, Popova EY, Priemchenko KY. Three stages of particle growth at acetylene pyrolysis behind shock waves. *WIPP abstracts 33 Int Symposium on Combustion*; 2010, Aug 1–6; Beijing China. Tsinghua University: W2P088.
- [124] Lahaye J, Prado G. Morphology and internal structure of soot and carbon blacks, in particulate carbon, formation during combustion. New York/London: Plenum Press; 1981.
- [125] Donnet JB, Voet A. Carbon black. Physics, chemistry and elastomer reinforcement. New York and Basel: Marcel Dekker, Inc.; 1976.
- [126] JCPDS. International center of diffraction data; 1997.
- [127] Borodina T, Fortov V, Lash AA, Zhuk AZ, Babaev VG, Gusev MB, et al. Shock induced transformations of carbyne. *J Appl Phys* 1966;80:3757–60.
- [128] Asinovskii E. Carbyne in phase diagram of carbon. Preprint No.1-449. Moscow: Institute of High Temp RAS; 2000.
- [129] Emelianov AV, Eremin AV, Makeich AA, Jander H, Wagner HGG, Starke R, et al. Heat release of carbon particle formation from hydrogen free precursors behind shock waves. *Proc Combust Inst* 2007;31:649–56.
- [130] Deppe J, Emelianov A, Eremin A, Friedrichs G, Shumova V, Wagner HGG, et al. Nonequilibrium excitation of C_2 radicals during the thermal decomposition of C_3O_2 behind shock wave. *Zeit Phys Chem* 2001;215(3):417–25.
- [131] Wagner HGG, Deppe J, Emelianov A, Eremin A, Zaslonko I. Overequilibrium excitation of C_2 radicals during thermal decomposition of C_3O_2 . *Doklady Chem* 2001;379:181–6.
- [132] Baranyshyn YA, Fisenko SP, Penyazkov OG. Heat transfer and growth of nano- and submicron particles of black carbon in nonequilibrium gas mixture. Experiment and simulation. *J Heat Mass Transfer* 2010;53:5465–71.
- [133] Eremin AV, Ziborov VS, Naboko IM. Experimental study of optical features of shock-heated jets. Optical methods in dynamics of fluids and solids. Berlin/Heidelberg/New-York/Tokio: Springer Verlag; 1985. 349–355.
- [134] Babushok VI, Miziolek AW. Condensation flame of acetylene decomposition. *Combust Flame* 2004;136(1–2):141–5.
- [135] Emelianov AV, Eremin AV, Fortov EV, Jander H, Makeich AA, Wagner HG. Detonation wave driven by condensation of supersaturated carbon vapor. *Phys Rev E Rapid Com* 2009;79:035303–6.
- [136] Haynes BS, Jander H, Wagner HG. The effect of metal additives on the formation of soot in premixed flames. *Proc Combust Inst* 1978;17:1365–74.
- [137] Homann KH. Formation of large molecules, particulates and ions in premixed hydrocarbon flames; progress and unresolved questions. *Proc Combust Inst* 1984;20:857–70.
- [138] Hospital A, Roth P. In-situ mass growth measurements of charged soot particles from low pressure flames. *Proc Combust Inst* 1990;22:1573–9.
- [139] Maricq M. A comparison of soot size and charge distributions from ethane, ethylene, acetylene, and benzene/ethylene premixed flames. *Combust Flame* 2006;144:730–43.
- [140] Onischuk AA, di Stasio S, Karasev VV, Baklanov AM, Makhov GA, Vlasenko AL, et al. Evolution of structure and charge of soot aggregates during and after formation in a propane/air diffusion flame. *J Aerosol Sci* 2003;34:383–404.
- [141] Kovacevic E, Stefanovic I, Berndt J. Infrared fingerprints and periodic formation of nanoparticles in Ar/C_2H_2 plasmas. *J Appl Phys* 2003;93:2924–30.
- [142] Netleton MA. Thermal ionization of soot particles in gases heated by reflected shocks to 2500 to 4000 K. *J Phys D* 1972;5:L4–6.
- [143] Calcote HF. Mechanisms of soot nucleation in flames - a critical review. *Combust Flame* 1981;42:215–42.
- [144] Gerhardt PH, Homann KH. Ions and charged soot particles in hydrocarbon flames. 2. Positive aliphatic and aromatic ions in ethyne/oxygen flames. *J Phys Chem* 1990;94:5381–91.
- [145] Balthasar M, Mauss F, Wang H. A computational study of particle thermal ionization and its effect on soot mass growth in laminar premixed flames. *Combust Flame* 2002;29:204–16.
- [146] Savel'ev AM, Starik AM. Interaction of ions and electrons with nanoparticles in hydrocarbon combustion plasmas. *Tech Phys* 2006;51:444–52.
- [147] Moyerman RM, Shuler KE. The concentration of contaminant alkali salts in ground level air. *Science* 1953;118:612–4.
- [148] John W, Kaifer R, Rahn K, Wesolowski J. Trace element concentrations in aerosols from the San Francisco Bay area. *J Atmos Environ* 1973;7:107–11.
- [149] Aravin GS, Karasevich Yu K, Shumeiko AN. Ionization of hydrazoic acid in shock waves. *Combust Explosion Shock Waves* 1977;13:611–8.
- [150] Eremin A, Naboko I, Palopezhtentsev S. Radiation of sodium impurity in a vibrationally nonequilibrium nitrogen jet. *Opt Spektrosk* 1986;60:920–7.
- [151] Emelianov A, Eremin A, Jander H. Experimental study of carbon particle charging at shock wave pyrolysis of C_3O_2 . *Proc Combust Inst* 2009;32:721–8.
- [152] Böhm H, Hesse D, Jander H, Lüers B, Pietscher J, Wagner HGg, et al. The influence of pressure and temperature on soot formation in premixed flames. *Proc Combust Inst* 1989;22:403–11.
- [153] Warnatz J, Maas U, Dibble RW. *Combustion*. Springer Verlag, ISBN 3-540-60730-7; 1996.
- [154] Savvatimskiy AI. Measurements of the melting point of graphite and the properties of liquid carbon (a review for 1963–2003). *Carbon* 2005;45:1115–42.
- [155] Winter NW, Ree FH. Carbon particle phase stability as a function of size. *J Comput-Aided Mater Des* 1998;5:279–94.
- [156] Jiang Q, Chen ZP. Thermodynamic phase stabilities of nanocarbon. *Carbon* 2006;44:79–83.
- [157] D'Anna A, Rolando A, Allouis C, Minatolo P, D'Alessio A. Nano-organic carbon and soot particle measurements in a laminar ethylene diffusion flames. *Proc Combust Inst* 2005;30:1449–56.
- [158] Ciajolo A. Condensed phases in soot formation process. In: Bockhorn H, D'Anna A, Sarofim AF, Wang H, editors. *Combustion generated fine carbonaceous particles*. KIT Scientific Publishing, ISBN 978-3-86644-441-6; 2009. p. 333–44.
- [159] Frenklach M, Wang H. Detailed modeling of soot particle nucleation and growth. *Proc Combust Inst* 1991;23:1559–66.
- [160] Kazakov A, Frenklach M. Dynamic modeling of soot particle coagulation and aggregation: implementation with the method of moments and application to high-pressure laminar premixed flames. *Combust Flame* 1999;114(3–4):484–501.

- [161] Patterson RIA, Kraft M. Models for the aggregate structure of soot particles. *Combust Flame* 2007 Oct;151(1–2):160–72.
- [162] Frenklach M. Method of moments with interpolative closure. *Chem Eng Sci* 2002 Jun;57(12):2229–39.
- [163] Mueller ME, Blanquart G, Pitsch H. Hybrid method of moments for modeling soot formation and growth. *Combust Flame* 2009;156(6):1143–55.
- [164] Deufhard P, Wulkow M. Computational treatment of polyreaction kinetics by orthogonal polynomials of a discrete variable. *Impact Comput Sci Eng* 1989;1:269–301.
- [165] Wulkow M. The simulation of molecular weight distribution in polyreaction kinetics by discrete Galerkin methods. *Macromol Theory Simul* 1996;5: 393–416.
- [166] Sirignano M, Kent J, D'Anna A. Detailed modeling of size distribution functions and hydrogen content in combustion-formed particles. *Combust Flame* 2010;157:1211–9.
- [167] D'Anna A, Sirignano M, Kent J. A model of particle nucleation in premixed ethylene flames. *Combust Flame* 2010;157:2106–15.
- [168] Park SH, Rogak SN. A novel fixed-sectional model for the formation and growth of aerosol agglomerates. *J Aerosol Sci* 2004;35:1385–404.
- [169] Wen JZ, Thomson MJ, Lightstone MF, Park SH, Rogak SN. An improved moving sectional model of soot formation in a plug flow reactor. *Combust Sci Technol* 2006;178(5):921–51.
- [170] Wen JZ, Thomson MJ, Park SH, Rogak SN, Lightstone MF. Study of soot growth in a plug flow reactor using a moving sectional model. *Proc Combust Inst* 2005;30(1):1477–84.
- [171] Park SH, Rogak SN, Bushe WK, Wen JZ, Thomson MJ. An aerosol model to predict size and structure of soot particles. *Combust Theory Model* 2005; 9(3):499–513.
- [172] Zhang O, Guo H, Liu F, Smallwood GJ, Thomson MJ. Implementation of an advanced fixed sectional aerosol dynamics model with soot aggregate formation in a laminar methane/air coflow diffusion flame. *Combust Theory Model* 2008;12(4):621–41.
- [173] Morgan N, Kraft M, Balthasar M, Wong D, Frenklach M, Mitchell P. Numerical simulations of soot aggregation in premixed laminar flames. *Proc Combust Inst* 2007;31(1):693–700.
- [174] Balthasar M, Kraft M. Stochastic approach to calculate the particle size distribution function of soot particles in laminar premixed flames. *Combust Flame* 2003;133(3):289–98.
- [175] Raj A, Celnik M, Shirley R, Sander RM, Patterson R, West R, et al. A statistical approach to develop a detailed soot growth model using PAH characteristics. *Combust Flame* 2009;156(4):896–913.
- [176] Violi A. Modeling of soot particle inception in aromatic and aliphatic premixed flames. *Combust Flame* 2004;139(4):279–87.
- [177] Frenklach M, Schuetz CA, Ping J. Migration mechanism of aromatic-edge growth. *Proc Combust Inst* 2005;30(1):1389–96.
- [178] Chung SH, Violi A. Insights on the formation and growth of carbonaceous nanoparticles in high temperature environments. In: Bockhorn H, D'Anna A, Sarofim AF, Wang H, editors. *Combustion generated fine carbonaceous particles*. KIT Scientific Publishing, ISBN 978-3-86644-441-6; 2009. p. 321–32.
- [179] Richter H, Howard JB. Formation of polycyclic aromatic hydrocarbons and their growth to soot—a review of chemical reaction pathways. *Prog Energy Combust Sci* 2000;26:565–608.
- [180] Miller JA, Pilling MJ, Troe J. Unravelling combustion mechanisms through a quantitative understanding of elementary reactions. *Proc Combust Inst* 2005;30(1):43–88.
- [181] Celnik M, Raj A, West R, Patterson R, Kraft M. Aromatic site description of soot particles. *Combust Flame* 2008;155(1–2):161–80.
- [182] Totton TS, Chakrabarti D, Misquitta AJ, Sander M, Wales DJ, Kraft M. Modelling the internal structure of nascent soot particles. *Combust Flame* 2010;157(5):909–14.
- [183] Sander MR, Patterson IA, Braumann A, Raj A, Kraft M. Developing the PAH-PP soot particle model using process informatics and uncertainty propagation. *Proc Combust Inst* 2011;33:675–83.
- [184] Frenklach M. On surface growth mechanism of soot particles. *Proc Combust Inst* 1996;26:2285–93.
- [185] Frenklach M. Reaction mechanism of soot formation in flames. *Phys Chem Chem Phys* 2002;4(2):2028–37.
- [186] Bonne U, Homann KH, Wagner HG. Carbon formation in premixed flames. *Proc Combust Inst* 1965;10:503–12.
- [187] Homann KH, Wagner HG. Some new aspects of the mechanism of carbon formation in premixed flames. *Proc Combust Inst* 1967;11:371–9.
- [188] Krestinin AV. Polyne model of soot formation process. *Proc Combust Inst* 1998;27:1557–63.
- [189] Krestinin AV. Detailed modeling of soot formation in hydrocarbon pyrolysis. *Combust Flame* 2000;121(3):513–24.
- [190] Dale I. In: Viehe HG, editor. *Chemistry of Acetylenes*. New York: Marcel Dekker; 1969.
- [191] Frenklach M, Clary DW, Gardiner Jr WC, Stein SE. Detailed kinetic modeling of soot formation in shock tube pyrolysis of acetylene. *Proc Combust Inst* 1984;20:887–901.
- [192] Kiefer JH, Von Drasek WA. The mechanism of the homogeneous pyrolysis of acetylene. *Int J Chem Kinet* 1990;22:747–86.
- [193] Raman A, Sivaramakrishnan R, Brezinsky K. Role of diacetylene in soot formation. In: Bockhorn H, D'Anna A, Sarofim AF, Wang H, editors. *Combustion generated fine carbonaceous particles*. KIT Scientific Publishing, ISBN 978-3-86644-441-6; 2009. p. 75–8.
- [194] D'Anna A. Particle inception and growth: experimental evidences and a modelling attempt. In: Bockhorn H, D'Anna A, Sarofim AF, Wang H, editors. *Combustion generated fine carbonaceous particles*. KIT Scientific Publishing, ISBN 978-3-86644-441-6; 2009. p. 289–320.
- [195] Deppe J, Emelianov A, Eremin A, Jander H, Wagner HG, Zaslonko IS. High-temperature carbon particle formation and decay in carbon suboxide pyrolysis behind shock waves. *Zeit Phys Chem* 2000;214(1): 129–35.
- [196] Agafonov GL, Nullmeier M, Vlasov PA, Warnatz J, Zaslonko IS. Kinetic modeling of solid carbon particle formation and thermal decomposition during carbon suboxide pyrolysis behind shock waves. *Combust Sci Technol* 2002;174:185–213.
- [197] Krestinin AV, Moravsky AP, Tesner PA. Kinetic model of fullerenes C60 and C70 formation at condensation of carbon vapor. *Khimicheskaya Fizika* 1998; 17(9):70–84 [in Russian].
- [198] Wagner HG, Vlasov PA, Dorge KJ, Eremin AV, Zaslonko IS, Tanke D. Kinetics of carbon cluster formation in the course of C₃O₂ pyrolysis. *Kinet Catal* 2001; 42:583–93.
- [199] Vlasov PA, Warnatz J. Detailed kinetic modeling of soot formation in hydrocarbon pyrolysis behind shock waves. *Proc Combust Inst* 2002;29: 2335–41.
- [200] Agafonov GL, Naydenova I, Vlasov PA, Warnatz J. Detailed kinetic modeling of soot formation in shock tube pyrolysis and oxidation of toluene and n-heptane. *Proc Combust Inst* 2007;31:575–83.
- [201] Kiefer JH, Sidhu SS, Kern RD, Xie K, Chen H, Harding LB. The homogeneous pyrolysis of acetylene II: the high temperature radical chain mechanism. *Combust Sci Technol* 1992;82(1):101–30.
- [202] Kruse T, Roth P. Kinetics of C₂ reactions during high-temperature pyrolysis of acetylene. *J Phys Chem A* 1997;101:2138–46.
- [203] Naydenova I, Marquetand J, Warnatz J. Soot formation simulation of shock tube experiments with the use of an empirical model. In: Bockhorn H, D'Anna A, Sarofim AF, Wang H, editors. *Combustion generated fine carbonaceous particles*. KIT Scientific Publishing, ISBN 978-3-86644-441-6; 2009. p. 405–12.